UNIVERSITÀ DEGLI STUDI DI PADOVA

Dipartimento di Fisica e Astronomia "Galileo Galilei"

Master Degree in Physics

Final Dissertation

Towards a precision measurement of Δm_s at LHCb

Thesis supervisor	Candidate
Dr. Alessandro Bertolin	Altea Lorenzon

Academic Year 2018/2019

Abstract

Indirect searches for new physics (NP) can be performed comparing measurements of the CKM angle γ from tree-processes with the results of global CKM fits. Assuming no NP in tree-level decays, any disagreement between tree-level determinations and the value inferred from global fits would indicate the presence of NP, due to new particles being exchanged in loops. $B_s^0 \to D_s^{\mp} K^{\pm}$ is a very sensitive tree-level decay for γ measurements accessible with high statistic at LHCb. For a precise determination of γ the mass difference Δm_s and the reconstruction efficiency as a function of the B_s^0 decay time have to be determined from a suitable control channel, namely $B_s^0 \to D_s^{-} \pi^{+}$. Tools and methods used in LHCb will be presented as well as the preliminary results obtained for both Δm_s and the decay time efficiency. The full LHCb Run 2 data sample will be used for these studies. Given the size of the $D_s \pi$ data sample a very accurate determination of Δm_s is achievable.

Contents

List of Figures

List of Tables

1   Introduction

Understanding the origin of the baryon asymmetry of the Universe is one of the key issues of modern physics. Sakharov showed that such an asymmetry can arise if three conditions are fulfilled [1], one of which is the requirement that both charge (C) and charge-parity (CP) symmetries are broken. The latter phenomenon arises in the Standard Model (SM) of particle physics through the complex phase of the Cabibbo-Kobayashi-Maskawa (CKM) quark mixing matrix [2, 3], although the effect in the SM is not large enough to account for the observed baryon asymmetry in the Universe [4]. Violation of CP symmetry can be studied by measuring the angles of the CKM unitarity triangle [5, 6, 7]. One of these angles, γ, can be measured using only tree-level processes [8, 9, 10, 11]. Disagreement between such direct measurements of γ and the value inferred from global CKM fits, assuming the validity of the SM and no new physics (NP) phenomenon in tree-level processes, would indicate new physics beyond the SM.

The study of neutral mesons with beauty, from a phenomenological point of view, allows to highlight some interesting phenomena, such as the neutral meson mixing. Furthermore, exploiting particular decay channels of the B_s^0, the CP violation phenomenon becomes accessible. This is the case of the non-flavour-specific $B_s^0 \to D_s^{\mp} K^{\pm}$ decay mode: in fact, B_s^0 and $\bar{B}_s^0$ can both decay at tree-level to the same final state, giving rise to CP violation in the interference between mixing and decay. The CP violating phase depends on the CKM angle γ [12, 13, 14]. The high statistics collected by LHCb allows for γ to be measured via a time-dependent analysis of the $B_s^0 \to D_s^{\mp} K^{\pm}$ decay channel. This measurement needs two fundamental inputs determined from the $B_s^0 \to D_s^- \pi^+$ control channel: the $B_s^0 - \bar{B}_s^0$ oscillation frequency, Δm_s, and the decay time efficiency. The measurement of these quantities is the subject of this work.

This thesis is organized as follows. In Chapter 2 a theoretical overview of the oscillation phenomenon in the $B_s^0 - \bar{B}_s^0$ system, of the properties of the CKM matrix and of the angle γ will be given in the context of the SM. Moreover, predictions for γ inferred from global fits will be presented, together with the LHCb 2018 γ combination. Finally the analysis strategy for the measurement Δm_s in the $B_s^0 \to D_s^- \pi^+$ channel at LHCb will be described and the 2011 LHCb result will be reported.

In Chapter 3 the main characteristics of the Large Hadron Collider and the data taking conditions during the two data taking campaigns, Run 1 and 2, are summarized. A description of the LHCb detector, in terms of its subdetectors and performances, follows. This Chapter gives also some characteristics of the b production processes at hadron colliders, such as LHC, and describes the *flavour tagging* techniques employed in LHCb to identify the flavour of b-mesons.

The following Chapters are dedicated to the analysis procedure and results. In Chapter 4 the $B_d^0 \to D^- \pi^+$ decays are considered. In fact, this particular channel can be reconstructed with a practically negligible background and can therefore be used as control channel to assess the correctness of the Montecarlo simulations and the goodness of the response of the detector. Then, a reweighing of the simulations will be performed to improve the agreement with data.

In Chapter 5 the channel of interest, $B_s^0 \to D_s^- \pi^+$, will be analysed: the invariant mass fit of the candidates provides a description of the signal and background contributions, while the fit to the decay time distribution allows to extract the value of Δm_s. At this stage, the decay time fit has been performed "blinded", meaning that only the statistical error of Δm_s is available to the analysts.

Finally, in Chapter 6 the mixing phenomenon between B_s^0 and $\bar{B}_s^0$ is highlighted through the *folded time asymmetry* distributions. Before building up these distributions on data, toy Montecarlo simulations will be used to study how different contributions, such as the finite decay time resolution of the detector or the probability for the flavour tagging algorithms to take the wrong decision, can affect these distributions.

The analysis is using the full Run 2 data sample, corresponding to $5.9\,\text{fb}^{-1}$ collected by LHCb from 2015 until 2018.

2 Standard Model and B Physics

The Standard Model (SM) of particle physics by now has been successful in describing experimental data; however it is considered an effective theory valid only at low energies, below the few TeV scale. New physics (NP) phenomena are predicted to emerge at higher energies. Two conceptually different approaches are used in analyses looking for beyond Standard Model (BSM) physics: direct and indirect searches. Direct searches are performed at the highest available energies and aim at producing and detecting new heavy particles. Indirect searches focus on precision measurements of quantum-loop-induced processes. In fact, accurate theoretical predictions are available for the heavy quark sector in the SM. Therefore heavy quark physics is an excellent playground to search for new phenomena, since any deviation from these predictions can be attributed to contributions from BSM.

This Chapter introduces the phenomenon of neutral meson mixing in the SM, in particular for the $B_{d,s}^0$ - $\bar{B}_{d,s}^0$ system (Section 2.1). In Section 2.2 and 2.3 the measurements already performed by the LHCb experiment on the key quantities γ, one of the three angles of the CKM matrix, and Δm_s, the $B_s^0 - \bar{B}_s^0$ oscillation frequency, are described.

2.1 $B_{d,s}^0$ - $\bar{B}_{d,s}^0$ mixing

2.1.1 Oscillation probability and decay amplitudes

Meson mixing is a phenomenon that only occurs for the weakly-decaying, open-flavor (*i.e.* not $q\bar{q}$ pairs) neutral K, D, and $B_{d,s}^0$ mesons [15, 16, 17]. The time evolution of the $B_{d,s}^0$ - $\bar{B}_{d,s}^0$ system can be described as

$$i\frac{\partial}{\partial t}\begin{pmatrix} B_{d,s}^0 \\ \bar{B}_{d,s}^0 \end{pmatrix} = \mathbf{H}_{\text{eff}}\begin{pmatrix} B_{d,s}^0 \\ \bar{B}_{d,s}^0 \end{pmatrix} \tag{2.1.1}$$

The effective Hamiltonian that describes the time evolution is a sum of the strong, electromagnetic (EM) and weak Hamiltonians:

$$\mathbf{H}_{\text{eff}} = \mathbf{H}_{\text{strong}} + \mathbf{H}_{\text{EM}} + \mathbf{H}_{\text{weak}} \tag{2.1.2}$$

and can be written in the $(B_{d,s}^0, \bar{B}_{d,s}^0)$ basis as

$$\mathbf{H}_{\text{eff}} = \mathbf{M} - i\frac{\mathbf{\Gamma}}{2} = \begin{pmatrix} M_{11} & M_{12} \\ M_{21} & M_{22} \end{pmatrix} - \frac{i}{2}\begin{pmatrix} \Gamma_{11} & \Gamma_{12} \\ \Gamma_{21} & \Gamma_{22} \end{pmatrix} \tag{2.1.3}$$

3
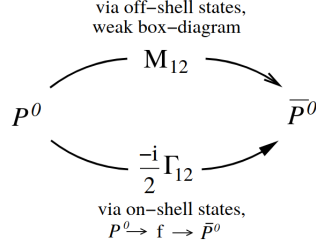
Figure 2.1: The neutral meson oscillation consists of two contributions, namely through off-shell states and on-shell states. Figure from [18].

where $\mathbf{M}$ and $\boldsymbol{\Gamma}$ are 2×2 Hermitian matrices describing the mass and decay rate components of $\mathbf{H}_{\text{eff}}$, respectively. The CPT symmetry imposes that the matrix elements in Equation 2.1.3 satisfy $M_{11} = M_{22}$, $\Gamma_{11} = \Gamma_{22}$, $M_{12} = M_{21}^*$ and $\Gamma_{12} = \Gamma_{21}^*$. In particular, M_{12} quantifies the short-distance contribution to the oscillation from off-shell states, as further discussed in Section 2.1.2, while Γ_{12} is related to the contribution from intermediate decays to a state f, as illustrated in Figure 2.1. Solving the time evolution represented by the effective Hamiltonian of Equation 2.1.3 is equivalent to the determination of its eigenstates; however, the eigenvalue problem is non-Hermitian, hence the eigenvalues will be complex and the eigenstates will be non-orthogonal. This non-Hermiticity, in particular the presence of the imaginary parts of the eigenvalues, leads to a non-unitary time evolution in the two-dimensional subspace spanned by the $B_{d,s}^0$ and the $\bar{B}_{d,s}^0$. As a consequence, probability is not conserved in this subspace, meaning that both mesons will eventually decay and hence disappear from this two-dimensional space.

The eigenstates of the effective Hamiltonian, or mass eigenstates, can be written as a superposition of flavour eigenstates via

$$|B_{1,2}^0\rangle = p\,|B_{d,s}^0\rangle \pm q\,|\bar{B}_{d,s}^0\rangle \tag{2.1.4}$$

with $|p|^2 + |q|^2 = 1$ to normalize the eigenstates and

$$\frac{q}{p} = \sqrt{\frac{M_{12}^* - \frac{i}{2}\Gamma_{12}^*}{M_{12} - \frac{i}{2}\Gamma_{12}}}$$

The corresponding eigenvalues are

$$m_1 - \frac{i}{2}\Gamma_1 = M_{11} - \frac{i}{2}\Gamma_{11} + \frac{p}{q}\left(M_{12} - \frac{i}{2}\Gamma_{12}\right) \tag{2.1.5}$$

$$m_2 - \frac{i}{2}\Gamma_2 = M_{11} - \frac{i}{2}\Gamma_{11} - \frac{p}{q}\left(M_{12} - \frac{i}{2}\Gamma_{12}\right) \tag{2.1.6}$$

where $m_{1,2}$ are the masses and $\Gamma_{1,2}$ the decay widths of the effective Hamiltonian eigenstates. These parameters determine the time evolution of a neutral meson that

oscillates between the particle and the anti-particle state.

The time evolution of the mass eigenstates is obtained from the Schrödinger equation (2.1.1) with diagonal effective Hamiltonian:

$$|B_1^0(t)\rangle = e^{-im_1 t - \frac{1}{2}\Gamma_1 t} |B_1^0(0)\rangle \tag{2.1.7}$$

$$|B_1^0(t)\rangle = e^{-im_2 t - \frac{1}{2}\Gamma_2 t} |B_2^0(0)\rangle \tag{2.1.8}$$

Assuming $m_2 > m_1$ we define $\Delta m = m_2 - m_1 > 0$ and $\Delta\Gamma = \Gamma_2 - \Gamma_1$. By combining Equations (2.1.4)(2.1.7) and (2.1.8) and defining the following quantities:

$$g_+(t) = \frac{1}{2}\left(e^{-im_1 t - \frac{1}{2}\Gamma_1 t} + e^{-im_2 t - \frac{1}{2}\Gamma_2 t}\right) \tag{2.1.9}$$

$$g_-(t) = \frac{1}{2}\left(e^{-im_1 t - \frac{1}{2}\Gamma_1 t} - e^{-im_2 t - \frac{1}{2}\Gamma_2 t}\right) \tag{2.1.10}$$

the time evolution of a pure $|B_{d,s}^0\rangle$ or $|\bar{B}_{d,s}^0\rangle$ state at $t = 0$ can be written as

$$|B_{d,s}^0(t)\rangle = g_+(t) |B_{d,s}^0(0)\rangle + \frac{q}{p} g_-(t) |\bar{B}_{d,s}^0(0)\rangle \tag{2.1.11}$$

$$|\bar{B}_{d,s}^0(t)\rangle = g_+(t) |\bar{B}_{d,s}^0(0)\rangle + \frac{p}{q} g_-(t) |B_{d,s}^0(0)\rangle \tag{2.1.12}$$

which means that the flavour states remain unchanged (+) or oscillate into each other (-) with time-dependent probabilities proportional to

$$|g_\pm(t)|^2 = \frac{e^{-\Gamma t}}{2}\left[\cosh\left(\frac{\Delta\Gamma t}{2}\right) \pm \cos(\Delta m t)\right] \tag{2.1.13}$$

with $\Gamma = (\Gamma_1 + \Gamma_2)/2$. Here we see that Γ fulfills the natural role of decay constant, $\Gamma = 1/\tau$, justifying the choice of the factor $1/2$ in Equation (2.1.3). From these relations we can compute the time-dependent decay rates for both $B_{d,s}^0$ and $\bar{B}_{d,s}^0$. If $|f\rangle$ is a common final state for both $B_{d,s}^0$ and $\bar{B}_{d,s}^0$, and $\bar{f}$ the CP conjugate, we denote the corresponding decay amplitudes as

$$A_f = \langle f| H_{|\Delta F|=1} |B_{d,s}^0(t)\rangle \qquad\qquad A_{\bar{f}} = \langle \bar{f}| H_{|\Delta F|=1} |B_{d,s}^0(t)\rangle$$
$$\bar{A}_f = \langle f| H_{|\Delta F|=1} |\bar{B}_{d,s}^0(t)\rangle \qquad\qquad \bar{A}_{\bar{f}} = \langle \bar{f}| H_{|\Delta F|=1} |\bar{B}_{d,s}^0(t)\rangle$$

where $H_{|\Delta F|=1}$ is the transition Hamiltonian involving a flavour change of one unit. Defining:

$$\lambda_f = \frac{q}{p}\frac{\bar{A}_f}{A_f} \qquad \bar{\lambda}_f = \frac{1}{\lambda_f} \qquad \lambda_{\bar{f}} = \frac{q}{p}\frac{\bar{A}_{\bar{f}}}{A_{\bar{f}}} \qquad \bar{\lambda}_{\bar{f}} = \frac{1}{\lambda_{\bar{f}}}$$

and considering the general expression for the time dependent decay rates $\Gamma_{B^0 \to f}(t) = |\langle f| H_{|\Delta F|=1} |B^0(t)\rangle|^2$, we obtain:

$$\Gamma_{B^0_{d,s} \to f}(t) = |A_f|^2 \quad \left\{ |g_+(t)|^2 + |\lambda_f|^2 |g_-(t)|^2 + 2\,\mathrm{Re}\left[\lambda_f g_+^*(t) g_-(t)\right] \right\} \quad (2.1.14)$$

$$\Gamma_{B^0_{d,s} \to \bar{f}}(t) = |\bar{A}_{\bar{f}}|^2 \left|\frac{q}{p}\right|^2 \left\{ |g_-(t)|^2 + |\bar{\lambda}_{\bar{f}}|^2 |g_+(t)|^2 + 2\,\mathrm{Re}\left[\bar{\lambda}_{\bar{f}} g_+(t) g_-^*(t)\right] \right\} \quad (2.1.15)$$

$$\Gamma_{\bar{B}^0_{d,s} \to f}(t) = |A_f|^2 \left|\frac{p}{q}\right|^2 \left\{ |g_-(t)|^2 + |\lambda_f|^2 |g_+(t)|^2 + 2\,\mathrm{Re}\left[\lambda_f g_+(t) g_-^*(t)\right] \right\} \quad (2.1.16)$$

$$\Gamma_{\bar{B}^0_{d,s} \to \bar{f}}(t) = |\bar{A}_{\bar{f}}|^2 \quad \left\{ |g_+(t)|^2 + |\bar{\lambda}_{\bar{f}}|^2 |g_-(t)|^2 + 2\,\mathrm{Re}\left[\bar{\lambda}_{\bar{f}} g_+^*(t) g_-(t)\right] \right\} \quad (2.1.17)$$

The terms proportional to $|A|^2$ are associated to decays that occurred without oscillation, whereas the terms proportional to $|A|^2 |q/p|^2$ or $|A|^2 |p/q|^2$ are associated to decays following a net oscillation. Terms proportional to $\mathrm{Re}(g^*g)$ are associated to the interference between the two cases. Using the results in Equation (2.1.13) and explicitly calculating the products:

$$g_+^*(t) g_-(t) = \frac{e^{-\Gamma t}}{2} \left[\sinh\left(\frac{\Delta\Gamma t}{2}\right) + i\sin\left(\Delta m t\right) \right] \quad (2.1.18)$$

$$g_+(t) g_-^*(t) = \frac{e^{-\Gamma t}}{2} \left[\sinh\left(\frac{\Delta\Gamma t}{2}\right) - i\sin\left(\Delta m t\right) \right] \quad (2.1.19)$$

we obtain the following decay amplitudes for the neutral B mesons:

$$\Gamma_{B^0_{d,s} \to f}(t) = |A_f|^2 \frac{e^{-\Gamma t}}{2} \left[(1 + |\lambda_f|^2) \cosh\left(\frac{\Delta\Gamma t}{2}\right) + 2\,\mathrm{Re}(\lambda_f) \sinh\left(\frac{\Delta\Gamma t}{2}\right) \right.$$
$$\left. + (1 - |\lambda_f|^2) \cos(\Delta m t) - 2\,\mathrm{Im}(\lambda_f) \sin(\Delta m t) \right] \quad (2.1.20)$$

$$\Gamma_{\bar{B}^0_{d,s} \to f}(t) = |A_f|^2 \left|\frac{p}{q}\right|^2 \frac{e^{-\Gamma t}}{2} \left[(1 + |\lambda_f|^2) \cosh\left(\frac{\Delta\Gamma t}{2}\right) + 2\,\mathrm{Re}(\lambda_f) \sinh\left(\frac{\Delta\Gamma t}{2}\right) \right.$$
$$\left. - (1 - |\lambda_f|^2) \cos(\Delta m t) + 2\,\mathrm{Im}(\lambda_f) \sin(\Delta m t) \right] \quad (2.1.21)$$

Here the sinh- and sin- terms are associated to the interference between the decays with and without oscillation. Commonly, the latter equations are expressed as

$$\Gamma_{B^0_{d,s} \to f}(t) = |A_f|^2 (1 + |\lambda_f|^2) \frac{e^{-\Gamma t}}{2} \left[\cosh\left(\frac{\Delta\Gamma t}{2}\right) \right.$$
$$\left. + D_f \sinh\left(\frac{\Delta\Gamma t}{2}\right) + C_f \cos(\Delta m t) - S_f \sin(\Delta m t) \right] \quad (2.1.22)$$

$$\Gamma_{\bar{B}^0_{d,s} \to f}(t) = |A_f|^2 \left|\frac{p}{q}\right|^2 (1 + |\lambda_f|^2)\frac{e^{-\Gamma t}}{2}\left[\cosh\left(\frac{\Delta\Gamma t}{2}\right)\right.$$
$$\left. + D_f \sinh\left(\frac{\Delta\Gamma t}{2}\right) - C_f \cos(\Delta m t) + S_f \sin(\Delta m t)\right] \qquad (2.1.23)$$

with
$$D_f = \frac{2\,\mathrm{Re}(\lambda_f)}{1 + |\lambda_f|^2} \qquad C_f = \frac{1 - |\lambda_f|^2}{1 + |\lambda_f|^2} \qquad S_f = \frac{2\,\mathrm{Im}(\lambda_f)}{1 + |\lambda_f|^2} \qquad (2.1.24)$$

2.1.2 Standard Model prediction and phenomenology

In the SM, the transitions $B^0_{d,s} \to \bar{B}^0_{d,s}$ are due to charged-current (CC) weak interactions. The lagrangian in terms of mass eigenstates is

$$\mathcal{L}^{\mathrm{SM}}_{\mathrm{CC}} = \frac{g}{\sqrt{2}}\left\{W^\dagger_\mu\left[\sum_{ij}\bar{u}^i_L\gamma^\mu V_{ij}d^j_L\right] + h.c.\right\} \qquad (2.1.25)$$

where g is the $SU(2)_L$ coupling constant, W_μ the boson field, $\mathbf{u}_L$ and $\mathbf{d}_L$ the triplet of left-handed up-type quarks and down-type quarks, respectively, and $\mathbf{V}$ the quark mixing matrix, labelled also $\mathbf{V}_{\mathrm{CKM}}$ [2, 3], that arises in the quark CC sector when switching from flavour to mass eigenstates. The CKM matrix $\mathbf{V}$ is a 3×3 complex unitary matrix commonly expressed as

$$\mathbf{V} = \begin{pmatrix} V_{ud} & V_{us} & V_{ub} \\ V_{cd} & V_{cs} & V_{cb} \\ V_{td} & V_{ts} & V_{tb} \end{pmatrix} \qquad (2.1.26)$$

More details about the standard electroweak theory can be found in [19, 20, 21, 22]. Since the $B^0_{d,s} \to \bar{B}^0_{d,s}$ oscillations involve a change of flavour $|\Delta F| = 2$ but no charge difference between the initial and the final state, this phenomenon is part of the flavour changing neutral current (FCNC) processes and is highly suppressed in the SM. In fact the $B^0_{d,s} \to \bar{B}^0_{d,s}$ mixing is described, at lowest order, by box diagrams involving two W bosons and two up-type quarks (see Figure 2.2), with the associated effective Hamiltonian

$$H_{\Delta F=2} = \frac{G_F^2 m_W^2 \eta_B}{4\pi^2}S_0\left(\frac{m_t^2}{m_W^2}\right)\left(V^*_{td,ts}V_{tb}\right)^2\bar{s}_L(\gamma_\mu)b_L \cdot \bar{s}_L\gamma^\mu b_L \qquad (2.1.27)$$

where G_F is the Fermi constant and m_W the W mass. The Inami-Lim function $S_0\left(m_t^2/m_W^2\right)$ [23], describing the result of the 1-loop box diagrams in the SM, can be very accurately approximated by $0.784\left(m_t^2/m_W^2\right)^{0.76}$ [24]; the QCD correction factor
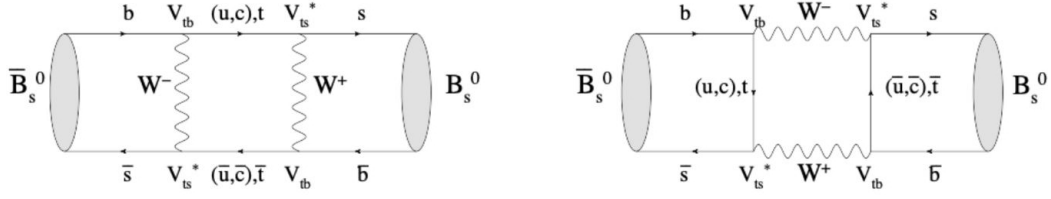
Figure 2.2: Box diagrams for the $B_s^0 \to \bar{B}_s^0$ transitions. The dominant contribution comes from diagrams the t quarks.

η_B is of order unity [25]. The calculation of the dispersive and absorptive parts of the box diagrams yields the following predictions for the off-diagonal element of the mass and decay matrices [23]

$$M_{12} = -\frac{G_F^2 m_W^2 \eta_B m_{B^0} B_{B^0} f_{B^0}^2}{12\pi^2} S_0\left(\frac{m_t^2}{m_W^2}\right)\left(V_{td,ts}^* V_{tb}\right)^2 \tag{2.1.28}$$

$$\begin{aligned}
\Gamma_{12} = &\frac{G_F^2 m_b^2 \eta_B' m_{B^0} B_{B^0} f_{B^0}^2}{8\pi}\Bigg[\left(V_{td,ts}^* V_{tb}\right)^2 \\
&+ V_{td,ts}^* V_{tb} V_{cd,cs}^* V_{cb} \mathcal{O}\left(\frac{m_c^2}{m_b^2}\right) + \left(V_{cd,cs}^* V_{cb}\right)^2 \mathcal{O}\left(\frac{m_c^4}{m_b^4}\right)\Bigg]
\end{aligned} \tag{2.1.29}$$

where m_i is the mass of quark i; m_{B^0}, f_{B^0} and B_{B^0} are the $B_{d,s}^0$ mass, weak decay constant and bag parameter respectively. The QCD correction factor η_B' is of order unity [25]. The only non negligible contributions to M_{12} are from box diagrams involving two top quarks.

The phases of M_{12} and Γ_{12} satisfy

$$\phi_M - \phi_\Gamma = \pi + \mathcal{O}\left(\frac{m_c^2}{m_b^2}\right) \tag{2.1.30}$$

implying that the mass eigenstates have mass and width differences of opposite signs *i.e.* the heavy state is expected to have a smaller decay width than the light state: $\Gamma_2 < \Gamma_1$. Furthermore the quantity

$$\left|\frac{\Gamma_{12}}{M_{12}}\right| \simeq \frac{3\pi}{2}\frac{m_b^2}{m_W^2}\frac{1}{S_0\left(m_t^2/m_W^2\right)} \sim \mathcal{O}\left(\frac{m_b^2}{m_t^2}\right) \tag{2.1.31}$$

is small and a power expansion of $|q/p|^2$ yields [26]

$$\left|\frac{q}{p}\right|^2 = 1 + \left|\frac{\Gamma_{12}}{M_{12}}\right| \sin\left(\phi_M - \phi_\Gamma\right) + \mathcal{O}\left(\left|\frac{\Gamma_{12}}{M_{12}}\right|^2\right) \tag{2.1.32}$$

Therefore, considering both Equations (2.1.30) and (2.1.31), the *CP* violating parameter

$$1 - \left|\frac{q}{p}\right|^2 \simeq \text{Im}\left(\frac{\Gamma_{12}}{M_{12}}\right) \tag{2.1.33}$$

is expected to be very small: $\sim \mathcal{O}(10^{-3})$ for the $B_d^0 - \bar{B}_d^0$ and $\lesssim \mathcal{O}(10^{-4})$ for the $B_s^0 - \bar{B}_s^0$ system, *i.e.* *CP* violation in $B_{d,s}^0$ mixing is a negligible effect at the present level of experimental precision [27]. However *CP* violation effects in interference between mixing and decay are studied when both $B_{d,s}^0$ and $\bar{B}_{d,s}^0$ decay to the same final state, f [28, 29, 30]. Assuming $|q/p| = 1$ the time-dependent *CP* asymmetry for B_d^0 can be written as [30, 31]

$$\mathcal{A}_f(t) = \frac{\Gamma(\bar{B}_d^0 \to f) - \Gamma(B_d^0 \to f)}{\Gamma(\bar{B}_d^0 \to f) + \Gamma(B_d^0 \to f)} = S_f \sin(\Delta m_d t) - C_f \cos(\Delta m_d t) \tag{2.1.34}$$

while for B_s^0

$$\mathcal{A}_f(t) = \frac{\Gamma(\bar{B}_s^0 \to f) - \Gamma(B_s^0 \to f)}{\Gamma(\bar{B}_s^0 \to f) + \Gamma(B_s^0 \to f)} = \frac{S_f \sin(\Delta m_s t) - C_f \cos(\Delta m_s t)}{\cosh(\Delta\Gamma t/2) - A_f^{\Delta\Gamma} \sinh(\Delta\Gamma t/2)} \tag{2.1.35}$$

where

$$A_f^{\Delta\Gamma} = \frac{-2\,\text{Re}(\lambda_f)}{1 + |\lambda_f|^2} \tag{2.1.36}$$

A complete set of SM predictions for all mixing parameters in both the $B_{d,s}^0 - \bar{B}_{d,s}^0$ systems can be found in [32, 33].

We relate Δm and $\Delta\Gamma$ with M_{12} and Γ_{12} by using expressions (2.1.5) and (2.1.6):

$$(\Delta m)^2 - \left(\frac{\Delta\Gamma}{2}\right)^2 = 4\left[|M_{12}|^2 - \left|\frac{\Gamma_{12}}{2}\right|^2\right] \tag{2.1.37}$$

$$\Delta m \Delta\Gamma = 4\,\text{Re}\left[M_{12}\Gamma_{12}^*\right] \tag{2.1.38}$$

As already pointed out, for B mesons the matrix element Γ_{12} is strongly CKM suppressed (see also [34]), thus $\Delta\Gamma$ is small compared to Δm, and can be set to zero. Neglecting $|\Gamma_{12}|$ in the previous expressions we get

$$\Delta m \simeq 2|M_{12}| \tag{2.1.39}$$

At this point we can see how the neutral mesons B_d^0 and B_s^0 oscillate. Keeping in mind that the oscillation probability is given by Equation (2.1.13), we see from Figure 2.3 that the B_s^0-mixing is more pronounced with respect to the B_d^0 system: in fact, the short-distance, off-shell contribution from M_{12} depends on the size of the CKM-elements at the corners of the box-diagram, and on the mass of the particles in the box. So the B_s^0 mixing proceeds proportional to $\sim |V_{tb}V_{ts}|^2 m_t^2$, while for B_d^0 to $\sim |V_{tb}V_{td}|^2 m_t^2$, but, as we will see in Section 2.2.1, the magnitude of V_{ts} exceeds the magnitude of V_{td}.
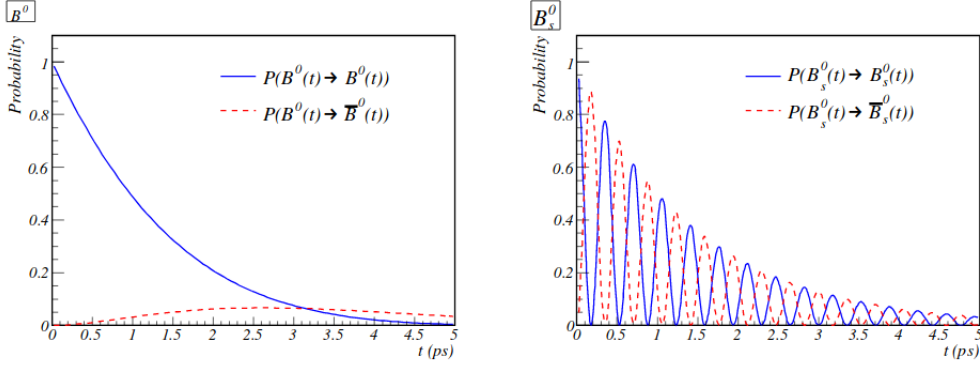
Figure 2.3: Probability to observe a $B_{d,s}^0$ or a $\bar{B}_{d,s}^0$-meson at time t, starting with a pure $B_{d,s}^0$-meson beam. The probability is expressed by Equation (2.1.13). Picture from [18].

2.2 The CKM angle γ

2.2.1 The Unitarity Triangle

We have encountered the CKM matrix **V** in Equation (2.1.25). It is a unitary 3×3 matrix, so it can be parameterized by three Euler angles and six complex phases [3]. Since quarks phases can be rotated freely

$$u_L^i \rightarrow e^{i\phi_u^i} u_L^i \qquad\qquad d_L^i \rightarrow e^{i\phi_d^i} d_L^i$$

with an appropriate redefinition of ϕ_u^i, ϕ_d^i, we can eliminate five phases of **V**, leaving only one physical phase. Due to this complex phase, the CKM matrix is a source (the only one) of CP violation in the SM. The fact that one can parametrize $\mathbf{V}_{\text{CKM}}$ by three real and only one imaginary physical parameters can be made manifest by choosing an explicit parametrization. The Wolfenstein parametrization [6, 7] is particularly useful

$$\mathbf{V} = \begin{pmatrix} 1 - \frac{1}{2}\lambda^2 & \lambda & A\lambda^3(\rho - i\eta) \\ -\lambda & 1 - \frac{1}{2}\lambda^2 & A\lambda^2 \\ A\lambda^3(1 - \rho - i\eta) & -A\lambda^2 & 1 \end{pmatrix} + \mathcal{O}(\lambda^4) \qquad (2.2.1)$$

with

$$\lambda = \frac{|V_{us}|}{\sqrt{|V_{ud}|^2 + |V_{us}|^2}} \qquad A\lambda^2 = \frac{|V_{cb}|}{\sqrt{|V_{ud}|^2 + |V_{us}|^2}} \qquad \bar{\rho} + i\bar{\eta} = -\frac{V_{ud}V_{ub}^*}{V_{cd}V_{cb}^*} \quad (2.2.2)$$

This parameterization nicely reveals the hierarchical structure of the CKM matrix, with diagonal elements of order 1 and smallest elements in the upper right and lower
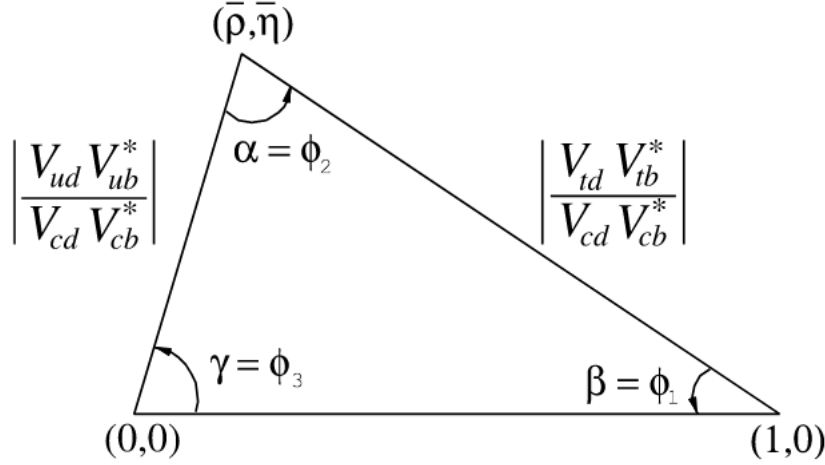
Figure 2.4: Representation of the unitarity triangle. Figure from [27].

left corners. In fact, the global fit results for these parameters are [27]

$$\lambda = 0.22453 \pm 0.00044 \qquad A = 0.836 \pm 0.015$$
$$\bar{\rho} = 0.122^{+0.018}_{-0.017} \qquad \bar{\eta} = 0.355^{+0.012}_{-0.011}$$

and for the magnitude of the nine elements of the CKM matrix [27]

$$\begin{pmatrix} 0.97446 \pm 0.00010 & 0.22452 \pm 0.00044 & 0.00365 \pm 0.00012 \\ 0.22438 \pm 0.00044 & 0.97359^{+0.00010}_{-0.00011} & 0.04214 \pm 0.00076 \\ 0.00896^{+0.00024}_{-0.00023} & 0.04133 \pm 0.00074 & 0.999105 \pm 0.000032 \end{pmatrix} \qquad (2.2.3)$$

The unitarity of the CKM matrix imposes:

$$\sum_i V_{ij} V_{ik}^* = \delta_{jk} \qquad \qquad \sum_j V_{ij} V_{kj}^* = \delta_{ik} \qquad (2.2.4)$$

The six vanishing combinations can be represented as triangles in a complex plane: the most commonly used unitarity triangle (UT), represented also in Figure 2.4, arises from

$$V_{ud} V_{ub}^* + V_{cd} V_{cb}^* + V_{td} V_{tb}^* = 0 \qquad (2.2.5)$$

by dividing each side by the best-known one, $V_{cd} V_{cb}^*$, its vertices are exactly $(0,0)$, $(1,0)$, and, due to the definition in Equation (2.2.2), $(\bar{\rho}, \bar{\eta})$. The angles of this

triangle are given by

$$\alpha \equiv \phi_2 \equiv \arg\left(-\frac{V_{td}V_{tb}^*}{V_{ud}V_{ub}^*}\right) \simeq \arg\left(-\frac{1-\rho-i\eta}{\rho+i\eta}\right) \tag{2.2.6}$$

$$\beta \equiv \phi_1 \equiv \arg\left(-\frac{V_{cd}V_{cb}^*}{V_{td}V_{tb}^*}\right) \simeq \arg\left(-\frac{1}{1-\rho-i\eta}\right) \tag{2.2.7}$$

$$\gamma \equiv \phi_3 \equiv \arg\left(-\frac{V_{ud}V_{ub}^*}{V_{cd}V_{cb}^*}\right) \simeq \arg\left(\rho+i\eta\right) \tag{2.2.8}$$

Another relation can be represented as a triangle

$$V_{us}V_{ub}^* + V_{cs}V_{cb}^* + V_{ts}V_{tb}^* = 0 \tag{2.2.9}$$

and its smaller angle, of $\mathcal{O}(\lambda^2)$

$$\beta_s \equiv \arg\left(-\frac{V_{ts}V_{tb}^*}{V_{cs}V_{cb}^*}\right) \tag{2.2.10}$$

is also convenient for analyzing CP violation in the B_s^0 sector.
The Wolfenstein phase convention in the CKM-matrix elements can be shown as:

$$\mathbf{V} = \begin{pmatrix} |V_{ud}| & |V_{us}| & |V_{ub}|e^{-i\gamma} \\ -|V_{cd}| & |V_{cs}| & |V_{cb}| \\ |V_{td}|e^{-i\beta} & -|V_{ts}|e^{i\beta_s} & |V_{tb}| \end{pmatrix} + \mathcal{O}(\lambda^5) \tag{2.2.11}$$

Since CP violation involves the phases of CKM elements [12, 13, 14], many measurements of CP-violating observables can be used to constrain the UT angles and the $\bar{\rho}, \bar{\eta}$ parameters. This is what happens in the case of γ. But an important difference from α and β occurs: in fact γ does not depend on CKM elements involving the top quark, so it can (also) be estimated in tree-level B decays [8, 9, 10, 11]. The latest CKMFitter [35] result for γ from tree-level quantities are shown in Figure 2.5, together with the corresponding global fit result. The numerical values reported in [36] are

$$\gamma_{tree} = 71.5°\,^{+3.6°}_{-4.5°} \qquad\qquad \gamma_{global} = 65.64°\,^{+0.97°}_{-3.42°} \qquad\qquad [68.3\%\ \text{CL}] \tag{2.2.12}$$

Detailed information on the methodology and treatment of the experimental and theoretical uncertainties for these estimations is provided in [37].
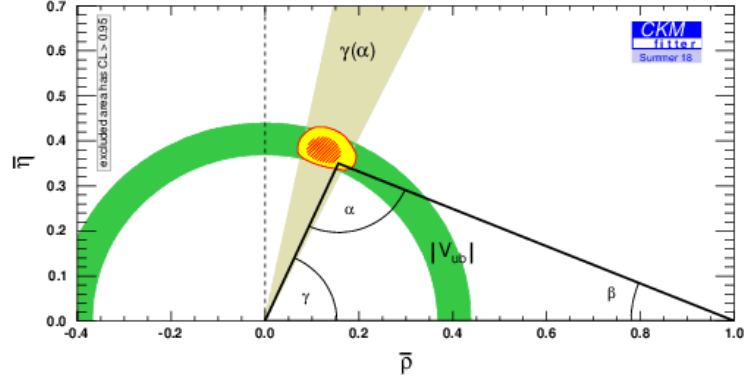
(a)
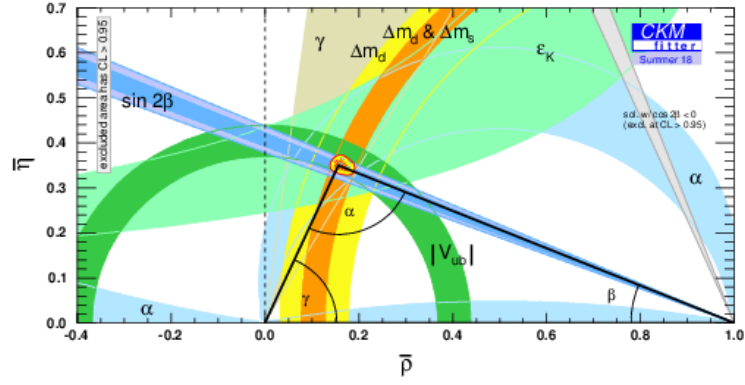
(b)
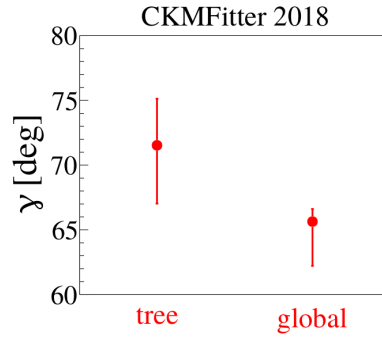
(c)

Figure 2.5: CKMFitter 2018 results. **(a)** Constraint on γ from tree-only fit; picture from [35]. **(b)** Global fit results; picture from [35]. **(c)** Numerical results for γ, Equation (2.2.12).

2.2.2   LHCb γ combination

The least precisely known angle of the CKM matrix is γ: as understood from the previous Section, it can be measured using only tree-level processes; a method that, assuming NP is not present in tree-level decays [38], has negligible theoretical uncertainty [39]. Any disagreement between such direct measurements of γ and the value inferred from global CKM fit, like the ones in Equation (2.2.12), would indicate the presence of new physics BSM.

The value of γ can be determined by exploiting the interference between favoured $b \to cW$ (V_{cb}) and suppressed $b \to uW$ (V_{ub}) transition amplitudes using a wide range of decay channels. The best precision is then obtained by combining measurements from many decay modes. The most recent LHCb γ combination [40] is obtained from time-integrated measurements of $B^+ \to DK^+$, $B^+ \to D^*K^+$, $B^+ \to DK^{*+}$, $B^0 \to DK^{*0}$, $B^0 \to DK^+\pi^-$ and $B^+ \to DK^+\pi^+\pi^-$ decays and time-dependent analyses of $B_s^0 \to D_s^\mp K^\pm$ and $B^0 \to D^\mp \pi^\pm$. All measurements used as inputs to the combination are summarized in Table 2.1. The combination procedure is described in [41]; it follows a frequentist treatment described in [42]. The combination gives the best fit value $\gamma = 74.0°$ and the confidence intervals:

$$\gamma \in [68.2, 79.0]° \quad \text{at } 68.3\% \text{ CL},$$
$$\gamma \in [61.6, 83.7]° \quad \text{at } 95.5\% \text{ CL}.$$

Taking the best fit value and the 68.3% CL interval, γ is found to be

$$\gamma = 74.0°\,^{+5.0°}_{-5.8°}$$

where the uncertainty includes statistical and systematic contributions. This result is in agreement with the world average reported in Equation (2.2.12) and with the previous LHCb average [43] and represents the most precise determination of γ from a single experiment to date.

Further improvements can be achieved increasing statistics. Data from Run 2 are currently being analysed. Both the statistical and the systematic uncertainties are expected to scale [44]. More precise results are foreseen also with the future LHCb upgrades, namely Upgrade I [45] (which is currently under construction and will start data taking in 2021 after LHC Long Shutdown 2) and Upgrade II [46] (with operations beginning in LHC Run 5, scheduled to start in 2031).

B decay	D decay	Method	Dataset	Ref.
$B^+ \to DK^+$	$D \to h^+h^-$	GLW	Run 1 & 2	[47]
$B^+ \to DK^+$	$D \to h^+h^-$	ADS	Run 1	[48]
$B^+ \to DK^+$	$D \to h^+\pi^-\pi^+\pi^-$	GLW/ADS	Run 1	[48]
$B^+ \to DK^+$	$D \to h^+h^-\pi^0$	GLW/ADS	Run 1	[49]
$B^+ \to DK^+$	$D \to K_s^0 h^+h^-$	GGSZ	Run 1	[50]
$B^+ \to DK^+$	$D \to K_s^0 h^+h^-$	GGSZ	Run 2	[51]
$B^+ \to DK^+$	$D \to K_s^0 K^+\pi^-$	GLS	Run 1	[52]
$B^+ \to D^*K^+$	$D \to h^+h^-$	GLW	Run 1 & 2	[47]
$B^+ \to DK^{*+}$	$D \to h^+h^-$	GLW/ADS	Run 1 & 2	[53]
$B^+ \to DK^{*+}$	$D \to h^+\pi^-\pi^+\pi^-$	GLW/ADS	Run 1 & 2	[53]
$B^+ \to DK^+\pi^+\pi^-$	$D \to h^+h^-$	GLW/ADS	Run 1	[54]
$B^0 \to DK^{*0}$	$D \to K^+\pi^-$	ADS	Run 1	[55]
$B^0 \to DK^+\pi^-$	$D \to h^+h^-$	GLW-Dalitz	Run 1	[56]
$B^0 \to DK^{*0}$	$D \to K_s^0\pi^+\pi^-$	GGSZ	Run 1	[57]
$B_s^0 \to D_s^{\mp}K^{\pm}$	$D_s^+ \to h^+h^-\pi^+$	TD	Run 1	[58]
$B^0 \to D^{\mp}\pi^{\pm}$	$D_s^+ \to K^+\pi^-\pi^+$	TD	Run 1	[59]

Table 2.1: List of the LHCb measurements used in the last combination [40], where TD stands for time-dependent and the method acronyms refer to the authors of Refs. [8, 9, 10, 11, 60, 61, 62]. Run 1 corresponds to an integrated luminosity of $3\,\text{fb}^{-1}$ taken at the center-of-mass energies of 7 and $8\,\text{TeV}$; Run 2 corresponds to an integrated luminosity of $2\,\text{fb}^{-1}$ taken at a center-of-mass energy of $13\,\text{TeV}$.

2.3 Δm_s measurements at LHCb

2.3.1 History and motivations

The experimental search for flavor oscillations in the B_s^0 system was pursued at multiple experiments for a long time: the first observation of particle-antiparticle transformations in neutral B mesons [63, 64] was made at DESY [65] by the AR-GUS collaboration [66] in 1987. In the following years the knowledge of B physics was further improved by experiments running at LEP (CERN, Geneva) [67], SLAC (Stanford, USA) [68] and Tevatron [69] (Fermilab, USA) where the CDF collaboration fist observed the $B_s^0 - \bar{B}_s^0$ mixing [70]. Since then, the determination of the $B_s^0 - \bar{B}_s^0$ oscillation frequency Δm_s from a time-dependent measurement of $B_s^0 - \bar{B}_s^0$ mixing has been a major objective of experimental particle physics [71]. The CDF collaboration performed a measurement of this quantity in 2006 [72]; the LHCb experiment published a first measurement of this frequency using a dataset taken at the LHC (CERN, Geneva) [73] in 2010, corresponding to an integrated luminosity of $37\,\mathrm{pb}^{-1}$ [74] and then using a data sample collected in 2011, corresponding to an integrated luminosity of $1.0\,\mathrm{fb}^{-1}$ [75], obtaining

$$\Delta m_s^{\mathrm{LHCb,\ 2011}} = 17.768 \pm 0.023\ (\mathrm{stat}) \pm 0.006\ (\mathrm{syst})\,\mathrm{ps}^{-1} \qquad (2.3.1)$$

More details about the latest LHCb measurement are given in the following Section. Studies continue nowadays not only at the LHC but also, for instance at the SuperKEKB (KEK, Tsukuba) [76]. In fact, the mixing phenomenon not only provides information on the parameters and validity of the SM, but it is also a sensitive probe for NP.

The mass differences Δm_s of the B_s^0 mass eigenstates could be used to determine the magnitude of one of the nine elements of the CKM matrix, $|V_{ts}|$; furthermore, a combined measurement of Δm_s and Δm_d could be used to derive the ratio $|V_{td}/V_{ts}|$ [77] with a small theoretical uncertainty, contributing to a stringent test of the unitarity of the CKM matrix [70]. More generally, it is used as an input parameter to CKM fits [36].

The LHCb experiment is currently interested in the measurement of Δm_s as a fundamental input to many time-dependent B_s measurements and as a key ingredient to searches for physics BSM in mixing phenomena. In the SM, transitions between quark flavours are possible at tree level via the CC weak interaction; FCNC processes are instead forbidden at lowest order, but allowed in higher order processes. Since new particles can contribute to these loop diagrams, such processes are highly sensitive to contributions from BSM [78]. Furthermore, many NP models that explain anomalies in the b-quark flavour sector, for example in the $b \to s\ell^+\ell^-$ transitions [79, 80] or in the lepton flavour universality ratios R_K and R_{K^*} [81, 82], are severely constrained by B_s^0-mixing (see for instance [83, 84, 85, 86, 87, 88, 89, 90]), for which the

SM prediction and experiments agreed well until recently [91, 92]. Taking however the most recent lattice average from the Flavour Lattice Averaging Group (FLAG) [93], which is more or less equivalent to the result obtained by Fermilab Lattice and MILC Collaborations [94], one gets a SM prediction for the mass difference [95] of

$$\Delta m_s^{\text{SM, 2017}} = (20.01 \pm 1.25)\,\text{ps}^{-1} \tag{2.3.2}$$

which is larger than the available measurements, like the one by LHCb reported in Equation (2.3.1). This has dramatic consequences for some NP models [95], but gives also new inputs to the theory community, see for instance [96].

2.3.2 Δm_s measurement from $B_s^0 \to D_s^- \pi^+$ at LHCb

This thesis work fits in the context of the time-dependent measurements of $B_s^0 \to D_s^- \pi^+$ performed at LHCb; the analysis aims to extract a precision measurement of Δm_s with Run 2 data to be used as one of the input parameters for an updated time-dependent measurement of γ in $B_s^0 \to D_s^{\mp} K^{\pm}$. Another quantity that can be extracted from $B_s^0 \to D_s^- \pi^+$ is the $B_s^0 \to D_s^{\mp} K^{\pm}$ decay time efficiency obtained as

$$\frac{\epsilon_{\text{decay time}}^{\text{DATA}}(D_s K)}{\epsilon_{\text{decay time}}^{\text{DATA}}(D_s \pi)} = \frac{\epsilon_{\text{decay time}}^{\text{MC}}(D_s K)}{\epsilon_{\text{decay time}}^{\text{MC}}(D_s \pi)} \tag{2.3.3}$$

The analysis strategy for the measurement of Δm_s from $B_s^0 \to D_s^- \pi^+$ is similar to that applied by LHCb in the previous measurement [75] and it is developed in different steps:

1. The analysis of the control channel $B_d^0 \to D^- \pi^+$, to check the reconstruction of kinematic variables. For this analysis the D candidates are reconstructed in the decay channel $D \to K\pi\pi$. This step is described in details in Chapter 4.

2. The fit to the invariant mass distribution of $B_s^0 \to D_s^- \pi^+$ candidates, where D_s^- candidates are reconstructed in five decay modes, namely $D_s^- \to \phi(K^+ K^-)\pi^-$, $D_s^- \to K^{*0}(K^+ \pi^-)K^-$, $D_s^- \to K^+ K^- \pi^-$ nonresonant, $D_s^- \to K^- \pi^+ \pi^-$ and $D_s^- \to \pi^- \pi^+ \pi^-$; charge conjugate processes are included too. As this is a flavour-specific process the flavour of the B_s^0 candidate at the time of its decay is given by the charges of the decay products.

3. The fit to the decay time distribution of the $B_s^0 \to D_s^- \pi^+$ candidates, from which Δm_s and $\epsilon_{\text{decay time}}^{\text{DATA}}(D_s \pi)$ can be measured. More details can be found in Chapter 5.

Using a data sample corresponding to an integrated luminosity of $1.0\,\text{fb}^{-1}$, collected at LHC in pp collisions at $\sqrt{s} = 7\,\text{TeV}$ in 2011, the measurement reported by LHCb is $\Delta m_s = 17.768 \pm 0.023\,(\text{stat}) \pm 0.006\,(\text{syst})\,\text{ps}^{-1}$ in good agreement both with the previous LHCb measurement [97] and the current world average [27].

3 LHC and LHCb

The Large Hadron Collider (LHC) [73] is the world's largest and most powerful particle accelerator. It is located at the European Organization for Nuclear Research, or CERN [98], in Geneva and is in operation since December 2009. It is a 27 km ring housed in the same tunnel that once hosted the Large Electron-Positron collider (LEP) at a depth ranging between 45 m and 170 m. LHC is only the latest addition to CERN accelerator's complex: it was designed to collide proton beams at a centre-of-mass energy of $\sqrt{s} = 14$ TeV and at nominal instantaneous luminosity of $\mathcal{L} = 10^{34}\,\mathrm{cm}^{-2}\mathrm{s}^{-1}$, which represent an extraordinary enhancement with respect to previous hadron colliders. In addition, LHC can accelerate lead ions up to 2.76 TeV with a luminosity $\mathcal{L} = 10^{31}\mathrm{cm}^{-2}\mathrm{s}^{-1}$.

Four experiments are installed along the circumference of LHC: CMS (Compact Muon Solenoid) [99] and ATLAS (A Toroidal LHC ApparatuS) [100] are general-purpose experiments designed to test the SM and search for BSM physics; the ALICE (A Large Ion Collider Experiment) [101] experiment analyses data from relativistic heavy ion collisions to study the physics of strongly interacting matter at extreme energy densities, where a phase of matter called quark-gluon plasma forms; LHCb (Large Hadron Collider beauty) [102] studies the properties of charm and beauty hadrons produced with large cross sections in the forward region.

In Sections 3.1 and 3.2 the LHC machine and the LHCb detector are described in more details, while in Section 3.3 flavour tagging techniques at LHCb are presented. Finally in Section 3.4 the production processes of b-hadrons in pp collisions are discussed.

3.1 The LHC machine

3.1.1 The structure

The LHC is composed by 1232 super-conducting dipole magnets each 15 m long, providing a 8.3 T magnetic field that keeps the beams circulating in their trajectories along the 27 km circumference. The beams, divided in bunches, travel in opposite directions inside two different vacuum pipes. More than 8000 additional magnets are used for beam injection, collimation, trajectory correction and finally crossing. All magnets are cooled by superfluid helium at a temperature of 1.9 K.

Before their injection into the LHC ring, the proton bunches are passed through a series of lower energy accelerators. The full acceleration chain is shown in Figure 3.1. Protons are produced by ionization of the hydrogen gas situated at the beginning of the colliders' chain; then, protons are fed into the LINear ACcelerator 2 (LINAC2)
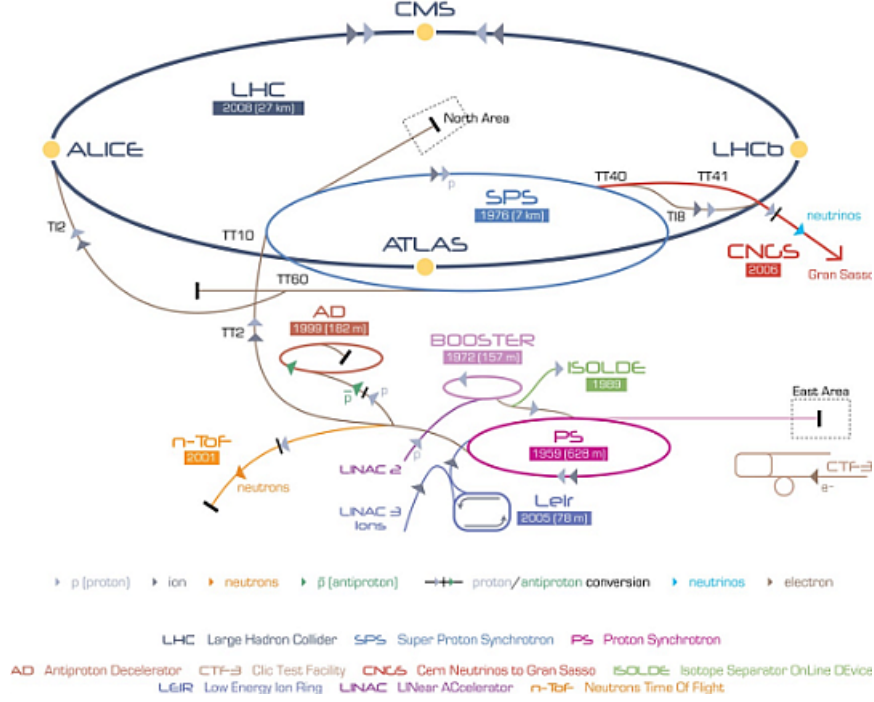
Figure 3.1: The accelerator complex at CERN. Image from [103].

where they reach an energy of 50 MeV before they are injected into the Proton Synchrotron Booster (PSB). Once the protons reach an energy of 1.4 GeV, they are transferred into the Proton Synchrotron (PS) followed by the Super Proton Synchrotron (SPS) where they are accelerated to energies of 25 GeV and 450 GeV respectively. They are then injected into the LHC in two counter rotating beams, where they are steered and accelerated up to a maximum energy of 7 TeV per beam with 16 superconducting Radio Frequency cavities (8 per beam) which raise the beam energy by 16 MeV each round with an electric field of 5 MV/m oscillating at 400 MHz frequency. The two separated beams cross in four interaction points, where the four LHC experiments are installed. At nominal LHC conditions, bunches are spaced by 25 ns equivalent to a bunch crossing frequency of 40 MHz, which corresponds to the rate of the collisions in the interaction points.

3.1.2 Performances

The two main features that characterize a particle collider are: the center-of-mass energy, which corresponds to the total amount of energy available to create new particles in a single collision, and the instantaneous luminosity, $\mathcal{L}$, which is the flux (the number of particles crossing the unit area per unit time) of the circulating

particles, defined as:

$$\mathcal{L} = \frac{f k N_1 N_2}{4\pi \sigma_x \sigma_y} \tag{3.1.1}$$

where f is the revolution frequency, k the number of bunches and $N_{1,2}$ the number of protons in each bunch; σ_x and σ_y the radius of particles' distribution in the transverse plane of the beam. At nominal LHC conditions, with $\sqrt{s} = 14\,\text{TeV}$ and $\mathcal{L} = 10^{34}\,\text{cm}^{-2}\text{s}^{-1}$, these parameters are equal to: $k = 2808$, $N_{1,2} = 1.5 \cdot 10^{11}$ and $\sigma_x \sigma_y = 16.6\,\mu\text{m}^2$ (while along the beam direction $\sigma_z = 7.6\,\text{cm}$). The rate of events, R, expected in the experiments is:

$$R = \sigma \mathcal{L} \tag{3.1.2}$$

where σ is the cross section of the process considered. Integrating the instantaneous luminosity over time it is possible to have an estimate of the number of events expected in the experiments, N:

$$N = \sigma \int_0^T \mathcal{L} dt = \sigma L \tag{3.1.3}$$

where L is called integrated luminosity.

LHC started its operations in December 2009 with a center-of-mass energy of $\sqrt{s} = 0.9\,\text{TeV}$; during the so-called Run 1, in 2010 and 2011 the center-of-mass energy was raised to $\sqrt{s} = 7\,\text{TeV}$, with a bunch crossing rate of 20 MHz, and obtained a maximum instantaneous luminosity at the start of fills, $\mathcal{L}_{peak}$, of about $3.7 \cdot 10^{33}\,\text{cm}^{-2}\text{s}^{-1}$. Then in 2012 $\sqrt{s}$ has been increased to 8 TeV, while $\mathcal{L}_{peak}$ reached $7.7 \cdot 10^{33}\,\text{cm}^{-2}\text{s}^{-1}$. Table 3.1 shows selected LHC parameters for Run 1 [104].

After a shut-down period to allow an upgrade of the LHC, during Run 2, from 2015 to 2018, the center-of-mass energy has been set to $\sqrt{s} = 13\,\text{TeV}$, with a bunch crossing rate of 40 MHz. The data-taking conditions evolved significantly during Run 2, with the LHC peak instantaneous luminosity increasing from 5 to $19 \cdot 10^{33}\,\text{cm}^{-2}\text{s}^{-1}$, as the number of colliding bunches. More details can be found in Table 3.2 [105].

After a two-year-long break known as Long Shutdown 2 (LS2), to allow the upgrades of the LHC machine and of the experiments, the collider will restart again in 2021 for the Run 3 operation period.

Parameter	2010	2011	2012
Maximum number of colliding bunch pairs	348	1331	1380
Bunch spacing [ns]	150	50	50
Typical bunch population [10^{11} protons]	0.9	1.2	1.7
Peak luminosity [$10^{33}\,\mathrm{cm}^{-2}\mathrm{s}^{-1}$]	0.2	3.6	7.7
Total delivered integrated luminosity	$47\,\mathrm{pb}^{-1}$	$5.5\,\mathrm{fb}^{-1}$	$23\,\mathrm{fb}^{-1}$

Table 3.1: Selected LHC parameters for *pp* collisions at $\sqrt{s} = 7\,\mathrm{TeV}$ in 2010 and 2011, and at $\sqrt{s} = 8\,\mathrm{TeV}$ in 2012. Values shown are representative of the best accelerator performance during normal physics operation.

Parameter	2015	2016	2017	2018
Maximum number of colliding bunch pairs	2232	2208	2544/1909	2544
Bunch spacing [ns]	25	25	25/8b4e	25
Typical bunch population [10^{11} protons]	1.1	1.1	1.1/1.2	1.1
Peak luminosity [$10^{33}\,\mathrm{cm}^{-2}\mathrm{s}^{-1}$]	5	13	16	19
Total delivered integrated luminosity [fb^{-1}]	4.0	38.5	50.2	63.4

Table 3.2: Selected LHC parameters for *pp* collisions at $\sqrt{s} = 13\,\mathrm{TeV}$ in 2015–2018. The values shown are representative of the best accelerator performance during normal physics operation. In 2017, the LHC was run in two modes: standard 25 ns bunch train operation, and '8b4e', denoting a pattern of eight bunches separated by 25 ns followed by a four bunch-slot gap. Values are given for both configurations.

3.2   The LHCb detector

The LHCb experiment is designed precisely to exploit the large production of highly boosted $b\bar{b}$ pairs at LHC (see also Sec. 3.4): it is in fact a single-arm spectrometer with a forward angular coverage from approximately 10 mrad to 300 mrad in the bending plane, that reduces to 250 mrad in the non-bending plane. This corresponds to a pseudorapidity coverage between 1.8 and 4.9, being the pseudorapidity defined as:

$$\eta = -\ln\left[\tan\left(\frac{\theta}{2}\right)\right] \tag{3.2.1}$$

where θ is the angle formed by the particle momentum and the beam axis.
The optimal luminosity for the LHCb experiment is $\sim 10^{32}\,\mathrm{cm}^{-2}\mathrm{s}^{-1}$, lower than that delivered by LHC. Running at this lower luminosity has some advantages: events are dominated by single pp interaction per bunch crossing (simpler to analyze than those with multiple primary pp interactions) and the occupancy in the detectors is reduced as well as the radiation damage to the apparatus. The luminosity provided by the LHC is reduced using a luminosity levelling technique, where the two beams do not collide head-on but they are tilted to obtain a larger interaction area [106]. During the fill, as the proton beams current and quality degrade, the tilt is reduced to obtain a constant instantaneous luminosity. Figure 3.2 shows the integrated luminosity of LHCb in pp collisions during all the years of data taking.
The LHCb detector is made of different subdetectors and its layout is shown in Figure 3.3. The subdetectors are:

- a VErtex LOcator (VELO) placed around the interaction point;

- a dipole magnet;

- a tracking system, with multiple stations located both upstream and downstream of the magnet;

- two Ring Imaging CHerenkov: RICH I is located after the VELO and RICH II after the tracking system stations;

- a calorimeter system composed of a Scintillator Pad Detector and a PreShower (SPD/PS), an Electromagnetic CALorimeter (ECAL) and a Hadronic CALorimeter (HCAL);

- a five-station muon tracking system (M1 - M5), mainly composed of multi-wire proportional chambers (MWPC), while in the highest rate region triple-GEM detectors are used.
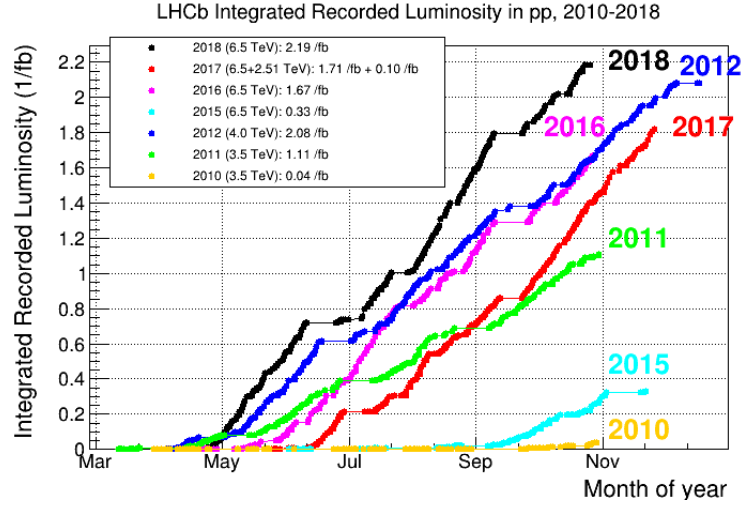
Figure 3.2: Integrated Recorded luminosity at LHCb in *pp* collisions in different years of data taking, from 2010 (begin of Run 1) to 2018 (end of Run 2). Image from [107].
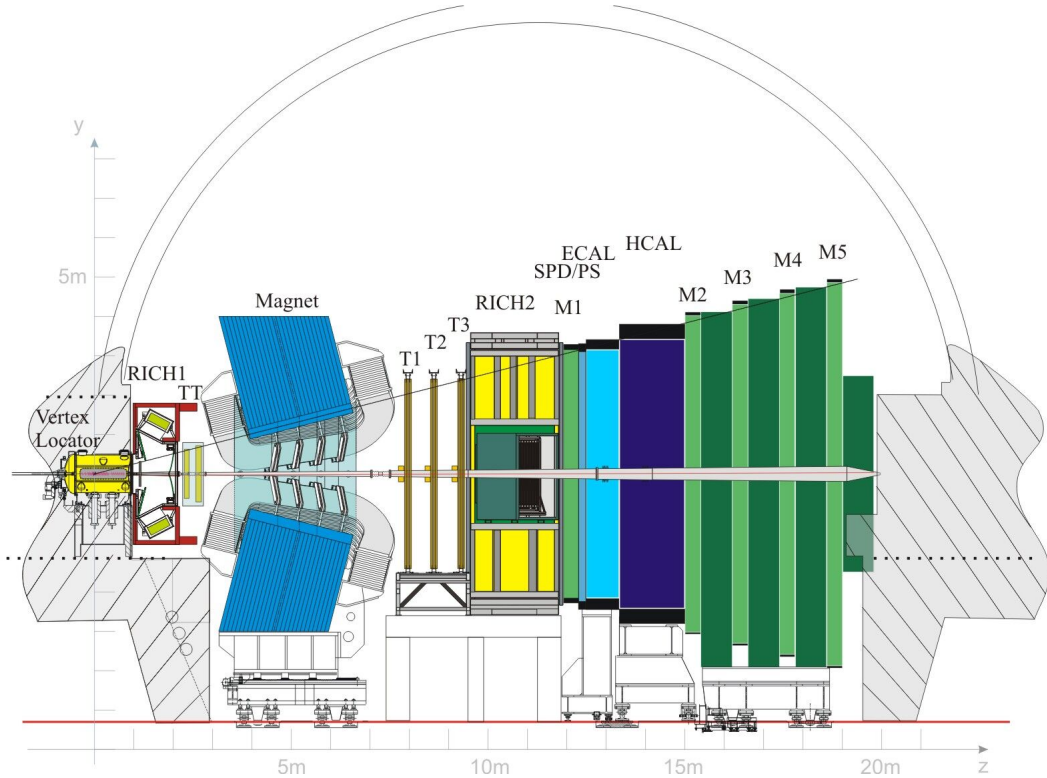
Figure 3.3: Schematic of the LHCb detector and its subdetectors. Image from [107].

In the standard right-handed LHCb coordinates system the z axis is parallel to the beam direction, the y axis has vertical direction and is pointing upwards and the x axis has horizontal direction pointing to the outside of the LHC-ring. Nominal proton-proton collisions happen in the z = 0 point of Figure 3.3.

In Table 3.3 a summary of the main LHCb performance numbers is presented.

Resolutions	Momentum resolution:	$\Delta p/p = 0.5\%$ at low momentum to 1% at 200 GeV/c
	Impact parameter resolution:	$(15 + 29/p_T[\text{GeV}])\,\mu\text{m}$
	Decay time resolution:	$\sim 45\,\text{fs}$ for $B_s^0 \to J/\psi\phi$ and for $B_s^0 \to D_s\pi$
	Invariant mass resolution:	$\sim 8\,\text{MeV/c}^2$ for $B \to J/\psi X$ decays with constraint on J/ψ mass
		$\sim 22\,\text{MeV/c}^2$ for two-body B decays
		$\sim 100\,\text{MeV/c}^2$ for $B_s^0 \to \phi\gamma$, dominated by photon contribution
Efficiencies	working detector channels:	$\sim 99\%$ for all subdetectors
	data taking efficiency:	90%; out of which 99% good for analyses
	trigger efficiencies:	$\sim 90\%$ for dimuon channels, $\sim 30\%$ for multi-body hadronic final states
	track reconstruction efficiency:	$\sim 96\%$ for long tracks
	PID efficiency	Electron ID $\sim 90\%$ for $\sim 5\%$ $e \to h$ mis-id probability
		Kaon ID $\sim 95\%$ for $\sim 5\%$ $\pi \to K$ mis-id probability
		Muon ID $\sim 97\%$ for $1-3\%$ $\pi \to \mu$ mis-id probability

Table 3.3: Summary of the main LHCb performance numbers, data from [108].

The following paragraphs review the main LHCb subdetectors.

3.2.1   VErtex LOcator

The basic tasks of the LHCb VELO [109] system are the reconstruction of the position of the primary vertex (PV), the detection of tracks which do not originate from the primary vertex and the reconstruction of the *b*-hadron decay vertices. The design of the VELO system is constrained by its integration into the LHCb detector and by its proximity to the LHC beams, which exposes the detector to an extreme radiation environment.

With a radial distance of $\sim 8\,\mathrm{mm}$, the VELO is the detector component closest to the beam in LHC. It is placed into a vessel where the vacuum is maintained, separated from the machine vacuum by aluminium sheets called RF-foils, studied to minimize multiple scattering effects. The VELO consists of a series of circular silicon strip modules arranged to cover $1\,\mathrm{m}$ distance along the beam direction: each module is divided into two separate halves, that are closed to form a circle (with a small overlap allowing relative alignment) only during the stable beams phases. The two halves host different kind of sensors:

- *r*-sensors, segmented in concentric semi-circles, thanks to which it is possible to measure the radial distance from the beam axis;

- *φ*-sensors, segmented radially, measuring the azimuthal angle.

The sensors are $300\,\mu\mathrm{m}$ thick but the strip length and pitch are sensor dependent. A schematic of the VELO structure is shown in Figure 3.4.

The performance of the VELO depends on the number of reconstructed tracks and their momenta. For a vertex with about 25 tracks a PV resolution of approximately $13\,\mu\mathrm{m}$ in the transverse plane ($70\,\mu\mathrm{m}$ along the z-axis) is achieved. The minimal distance of a charged track with respect to the PV, referred to as impact parameter (IP), can be reconstructed with a resolution of $35\,\mu\mathrm{m}$ for tracks with momentum larger than $1\,\mathrm{GeV}/c$. The angular acceptance is given by the solid angle in which at least three sensors are hit: $1.6 < \eta < 4.9$.

3.2.2   Dipole magnet

A dipole magnet [110] is used to bend the tracks of charged particles, in order to be able to measure their momentum. It is composed of two saddle-shaped coils placed symmetrically to each other inside a window-frame yoke, as shown also in Figure 3.5. The magnet provides an integrated magnetic field of about $4\,\mathrm{Tm}$ for tracks passing through the entire tracking system. The main component of the magnetic field is along the y-axis and thus bends charged tracks in the x-z plane. The very precise knowledge of this field allows the tracking detectors to perform momentum measurements on charged particles with a precision of about 0.4% for
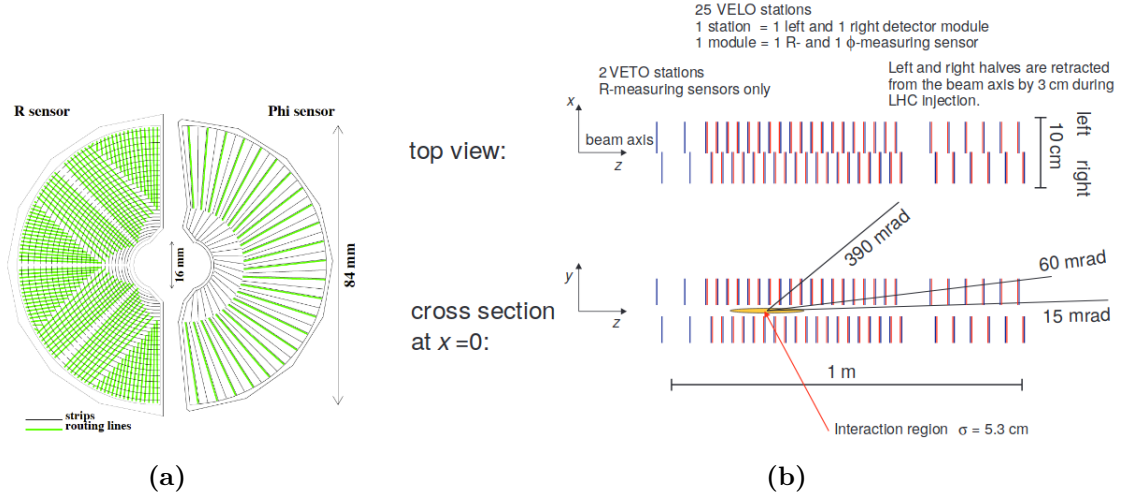
Figure 3.4: **(a)** Schematic representation of an r and a ϕ sensor. Image from [81]. **(b)** Arrangement of detectors along the beam axis. The top figure shows the VELO setup seen from above, indicating the overlap between the left and the right halves. The bottom figure is a cross section of the setup at x = 0, showing also the nominal position for the interaction area ($\pm 2\sigma$). The three black lines indicate the maximum and the minimum angular coverage and the average angle of tracks in minimum bias events. Image from [109].
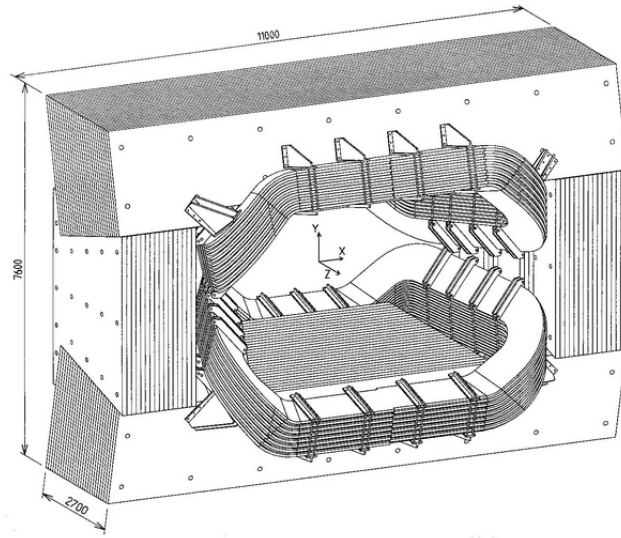
Figure 3.5: Representation of the LHCb dipolar magnet. Image from [110].

low momenta and 0.6% up to $200\,\mathrm{GeV}/c$. To cancel detector induced left-right asymmetries, the polarity of the magnet is periodically switched.

3.2.3   Tracking system

The tracking system is composed by four planar stations: the Tracker Turicensis (TT) [111], located between the RICH I and the dipole magnet, and the T1, T2, T3 stations, placed over $3\,\mathrm{m}$ between the magnet and the RICH II. The TT and the inner regions of the T1-T3 stations, called Inner Tracker (IT) [112], form the so called Silicon Tracker (ST) system; the outer regions of the T1-T3 stations are the Outer Tracker (OT) [113].

With a height of $130\,\mathrm{cm}$ and a width of $160\,\mathrm{cm}$, the TT covers the full angular acceptance of the VELO. The TT consists of four planes of silicon strip sensors grouped in two stations (TTa and TTb) and arranged in a (x-u-v-x) layout: the strips of the x layers are aligned with the y-axis, while the u and v layers are rotated by an angle of $+5°$ and $-5°$ respectively to infer also information on the y-dimension. A representation of the TT (x-u-v-x) layout is shown in Figure 3.6. The strip pitch of $183\,\mu\mathrm{m}$ leads to a spatial resolution of $\sim 50\,\mu\mathrm{m}$ in the x-dimension.

The IT covers an area of $120 \times 40\,\mathrm{cm}^2$ corresponding to less than 2% of the LHCb acceptance, but it is intercepted by about 20% of the tracks produced in pp collisions: a fine detector granularity is therefore required. Each station has four layers with the same (x-u-v-x) layout as the TT, and the same spatial resolution is achieved.

The OT is a drift time detector surrounding the IT and covering the remaining acceptance; it follows the same arrangement as the TT and IT, having four layers in (x-u-v-x) configuration per station. The tubes, having an internal diameter of $4.9\,\mathrm{mm}$, are filled with a mixture of Ar (70%), CO_2 (28.5%) and O_2 (1.5%). The proportions are chosen in order to achieve a drift distance resolution of $\sim 200\,\mu\mathrm{m}$. A schematic representation of the IT and OT layout is shown in Figure 3.7.

3.2.4   RICH I-II

Particle identification (PID) is a fundamental requirement of the LHCb experiment. The ability to distinguish between charged hadrons such as pions or kaons in a variety of final states is essential for the physics that the experiment is designed to study. In fact, meaningful CP-violation measurements are only possible in many important channels if hadron identification is available. The PID is achieved using two Ring Imaging CHerenkov (RICH) detectors [115]. They feature a similar setup, consisting of a suitable radiator material, a mirror system and a photo–sensitive detector component. When a charged particle exceeds the speed of light in the radiator, Cherenkov light is emitted in form of a cone, where the opening angle θ_C is
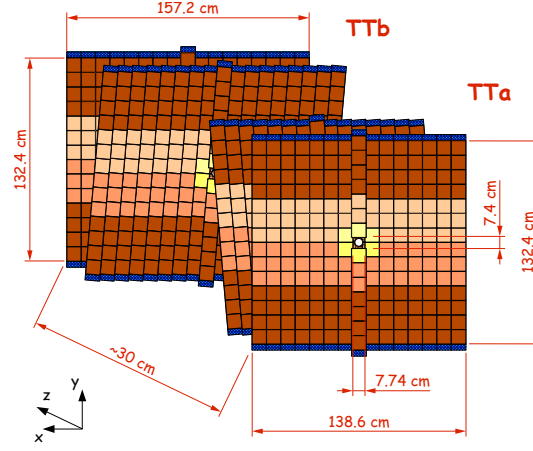
Figure 3.6: Layout of TT layers. Image from [114].

(a)   **(b)**
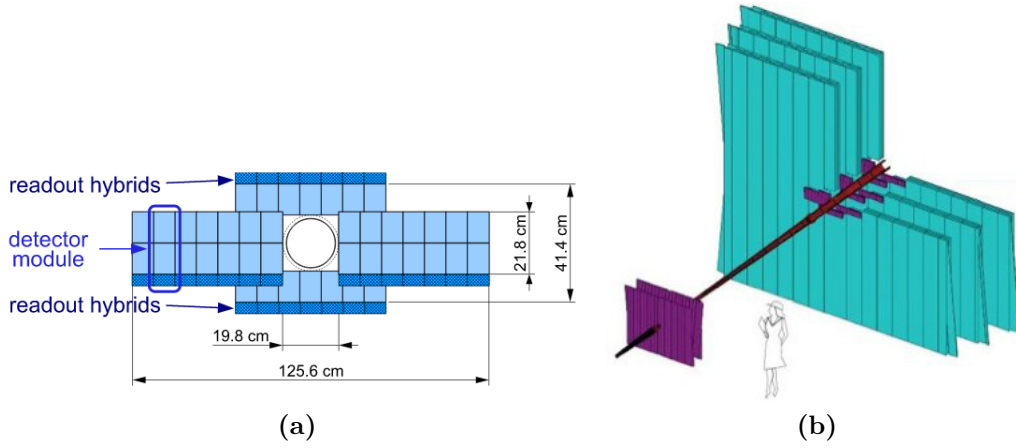
Figure 3.7: **(a)** Layout of an x detection layer in one of the IT stations. **(b)** Arrangement of OT straw-tube modules in layers and stations. Pictures from [102].

purely a function of the particle's velocity:

$$\cos(\theta_C) = \frac{1}{\beta n} \tag{3.2.2}$$

where n is the refraction index of the radiator and β the velocity in natural units. The emitted light cone is then guided by the mirror system to the photo–detectors. If the momentum of a particle is known from an independent measurement, the mass can be inferred from the measured angle θ_C.

The choice of using two different RICH detectors arises from the need to be sensitive

Figure 3.8: (a) Side view schematic layout of the RICH I detector. **(b)** Top view schematic of the RICH II detector. Images from [102].

over the wide momentum spectrum of particles in the LHCb acceptance. RICH I, having C_4F_{10} gas as radiator ($n = 1.0014$) performs best on the low-momentum ($1 - 60\,\text{GeV}/c$) particles, while RICH II, containing CF_4 ($n = 1.0005$), covers the high momentum range, from $50\,\text{GeV}/c$ up to $150\,\text{GeV}/c$.

3.2.5 Calorimeters

The main task of the calorimetry system [116] is to measure the particles' energy and location and to give information for the Level-0 trigger and, ultimately, PID. In LHCb the system is composed by four subdetectors, in order of position along z:

- a Scintillating Pad Detector (SPD);

- a PreShower (PS);

- an Electromagnetic CALorimeter (ECAL);

- a Hadronic CALorimeter (HCAL).

The layout of the calorimetry system is illustrated in Figure 3.9.
The SPD and the PS are almost two identical planes of scintillating pads separated by a 15 mm-thick lead layer, corresponding to 2.5 electromagnetic interaction lengths

and to ~ 0.06 hadronic interaction lengths. As only charged particles produce scintillating light, the SPD, together with the ECAL, provide a discrimination between $e^{\pm}$ and neutral particles (γ and π^0), which do not produce a SPD signal. The PS helps to discriminate charged $\pi^{\pm}$ and $e^{\pm}$, as the energy deposition in the layer of lead will be different for hadrons and leptons. The calorimeters are constructed as sampling calorimeters, meaning that alternating layers of absorber and scintillation material are positioned in a row. The absorber material is used to induce electromagnetic or hadronic showers; when the cascades of secondary particles hit the scintillators these cause the emission of photons proportional in number to the energy of the incident particle. Photons are then trasported through wavelength shifting fibers to photomultiplier tubes. The PS, SPD, ECAL and HCAL adopt a variable lateral segmentation, due to the fact that the hit density varies by two orders of magnitude over the calorimeter surface, depending on the radial distance from the beam. The ECAL comprises alternating layers of lead ($2\,\mathrm{mm}$) and scintillating tiles ($4\,\mathrm{mm}$). Its main purpose is to measure the energy of electrons and photons, which predominantly loose their energy in electromagnetic showers. Furthermore, it plays a crucial role in the reconstruction of neutral pions. The energy resolution of the ECAL is, in the inner modules

$$\frac{\sigma_E}{E} = \frac{(8.2 \pm 0.4)\%}{\sqrt{E}} \oplus (0.87 \pm 0.07)\%$$

The HCAL is used to measure the energy of hadrons, which induce hadronic showers while passing through the absorber plates, that in this case are made of iron. The HCAL resolution is

$$\frac{\sigma_E}{E} = \frac{(69 \pm 5)\%}{\sqrt{E}} \oplus (9 \pm 2)\%$$

3.2.6 Muon tracking system

A muon system [118], Figure 3.10, consisting of five stations (M1-M5) is used for track reconstruction and PID of muons. In the LHCb momentum range, muons act as minimum ionizing particles and are the only charged particles that travel through the whole detector. Therefore the muon stations are mainly placed furthest away from the interaction point (z > 15 m), where the majority of particles have already been stopped by interactions with the detector material. The first station (M1) is placed upstream of the PS, while the remaining four stations (M2, M3, M4 and M5) are located downstream of the calorimeter system, interleaved with iron absorbers to select penetrating muons.

All muon stations use Multi-Wire Proportional Chambers (MWPC), operating with a gas mixture of Ar (40%), CO_2 (55%) and CF_4 (5%), providing a time resolution of
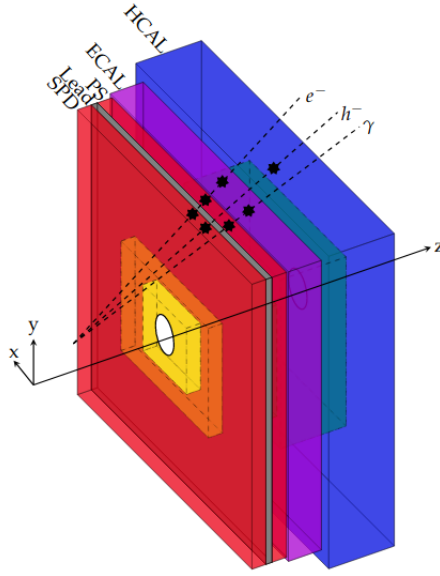
Figure 3.9: Layout of the SPD, PS, ECAL and HCAL showing the different segmentation areas and the interactions of different particle species. The relative dimensions of the ECAL and HCAL are correct, but the z-scale of the SPD/PS is exaggerated. Image from [117].
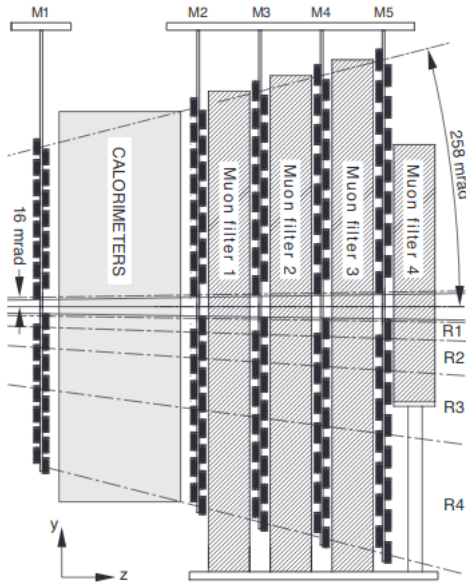
Figure 3.10: Side view of the muon system. Image from [102]

about 5 ns. Only in inner region of M1, where the particle flux is higher, triple-GEM (Gas Electron Multiplier) detectors are installed because of their higher radiation tolerance: the fast gas mixture (with proportion 45:15:40) allows a time resolution better than 3 ns.

Given the fast readout and high efficiency (the average muon identification efficiency is in fact 98%) the muon chambers play a crucial role in the LHCb trigger system.

3.2.7   Trigger

The LHCb trigger [119] is organized in two different levels, executed in cascade:

- the Level 0 trigger (L0) is a hardware trigger, operating synchronously with the bunch-crossing frequency (40 MHz during Run 2). It lowers the event rate to a maximum of ~ 1 MHz;

- the High Level Trigger (HLT) is a software trigger which is run asynchronously on the Event Filter Farm (EFF), a large computing cluster of about 29000 CPU cores. It is divided into two steps, HLT1 and HLT2, and reduces the event rate from 1 MHz to 5 kHz.

The L0 trigger uses the information provided by three different sub-systems: the VELO pile-up system (composed by the two r-sensors placed upstream the interaction region), the calorimeters and the muon tracker. It identifies the hadron, electron and photon clusters with the highest transverse energy in the calorimeters and the two tracks with the highest transverse momentum in the muon chambers. In addition, the pile-up system in the VELO estimates the number of primary pp interactions in each bunch crossing.

The HLT1 provides a fast confirmation of the L0 decision using more refined data: exploiting the information from the VELO and the T1-T3 stations a partial event reconstruction is performed, at this stage on high-p_T and high-p tracks. Their impact parameter with respect to the primary vertex is computed and used as a discriminating variable as well as the presence in the event of secondary vertices produced by the decay of flying particles. The computing power available in the Run 2 EFF allows for automated alignment and calibration tasks: dedicated samples selected by the HLT1 are used to align and calibrate the detector in real time.

The HLT2 consists of several selection lines run in parallel, corresponding each to a specific physics decay topology, matching events of interest for the LHCb physics program. It searches for secondary vertices and applies mass and kinematic cuts to reduce the rate of events. Using inclusive and exclusive algorithms, it performs the pattern recognition to find all tracks in the event and thus to provide a full event reconstruction. The output of the HLT2 is then written to disk to be further analysed.

A schematic of the overall trigger flow is shown in Figure 3.11

LHCb 2015 Trigger Diagram

40 MHz bunch crossing rate

L0 Hardware Trigger : 1 MHz readout, high E_T/P_T signatures

| 450 kHz $h^\pm$ | 400 kHz $\mu/\mu\mu$ | 150 kHz e/γ |

Software High Level Trigger

Partial event reconstruction, select displaced tracks/vertices and dimuons

Buffer events to disk, perform online detector calibration and alignment

Full offline-like event selection, mixture of inclusive and exclusive triggers

12.5 kHz (0.6 GB/s) to storage

Figure 3.11: The LHCb Run 2 trigger scheme. Picture from [120].

3.3 Flavour Tagging

The identification of the initial flavour of reconstructed B mesons is necessary for most of the measurements of time-dependent CP asymmetries and flavour oscillations. This procedure is known as flavour tagging (FT) and is performed at LHCb by means of several algorithms. Different sources of information can be used to asses the initial flavour of a B-meson candidate, as illustrated in Figure 3.12. In the following Sections, two types of tagger algorithms are described: opposite-side taggers, based on muons, electrons, kaons, charmed hadrons and inclusive secondary vertex data, and same-side taggers, based on kaons, pions and protons.

The performance of a flavour tagging algorithm is defined by its tagging efficiency, ϵ_{tag}, mistag fraction, ω, and dilution, $\mathcal{D} = 1 - 2\omega$. For a simple tagging algorithm with discrete decisions (for example B^0, $\bar{B}^0$, or untagged) these parameters are directly related to the number of rightly tagged (R), wrongly tagged (W), and untagged events (U) in a signal sample:

$$\epsilon_{tag} = \frac{R + W}{R + W + U} \tag{3.3.1}$$

$$\omega = \frac{W}{R + W} \tag{3.3.2}$$

$$\mathcal{D} = \frac{R - W}{R + W} \tag{3.3.3}$$

For each tagger, a multivariate classifier is trained using simulated data to distinguish between correct and incorrect decisions. The inputs to the classifier are a selection of quantities describing the event in general with the exception of any information concerning the B candidate to tag. The classifier then calculates a predicted mistag probability, η. The predicted mistag probability is then calibrated with data using an appropriate flavour self-tagged mode, such as $B^+ \to J/\psi K^+$, or a mode involving neutral B oscillation which self-tags its flavour at the decay-time, such as $B^0 \to J/\psi K^{*0}$ or $B_s^0 \to D_s^- \pi^+$ [121, 122]. This calibration procedure provides a function $\omega(\eta)$, which relates the actual mistag probability ω to the predicted mistag probability η:

$$\omega(\eta) = p_0 + p_1(\eta - \bar{\eta}) \tag{3.3.4}$$

$$\omega(B) - \omega(\bar{B}) = \Delta\omega = \Delta p_0 + \Delta p_1(\eta - \bar{\eta}) \tag{3.3.5}$$

where $\bar{\eta}$ is the average estimated mistag probability and $\Delta\omega$ represents the excess mistag probability for B^+ (B^0) with respect to B^- ($\bar{B}^0$). In the ideal case the parameter p_0 should be equal to $\bar{\eta}$, while p_1 should be equal to 1. $\bar{\eta}$ is introduced to "decorrelate" the parameters p_0, p_1, Δp_0, Δp_1.

The tagging efficiency and the mistag probabilities are used to calculate the effective tagging efficiency ϵ_{eff}, also known as tagging power:

$$\epsilon_{eff} = \epsilon_{tag} \frac{1}{R + W} \sum_{i=1}^{R+W} (1 - 2\omega(\eta_i))^2 \tag{3.3.6}$$

which represents the figure of merit in the optimisation of a flavour-tagging algorithm.

3.3.1   Opposite Side Taggers

Opposite-side (OS) tagging algorithms [123] rely on the pair production of b and $\bar{b}$ quarks and infer the flavour of a given B meson (signal B) from the identification of the flavour of the other b hadron (tagging B). The algorithms use the charge of the lepton (μ,e) from semileptonic b decays, the charge of the kaon from the $b \to c \to s$ decay chain or the charge of the inclusive secondary vertex reconstructed from b-hadron decay products. These taggers are called electron, muon, kaon (which we refer to as single particle taggers) and vertex charge taggers, respectively. Recently a new OS flavour tagging algorithm has been implemented, that relies on the correlation between the reconstructed decays of charm hadrons produced in the OS b hadron decay [124].

In the case of single particle taggers, the tagging particles are selected exploiting the
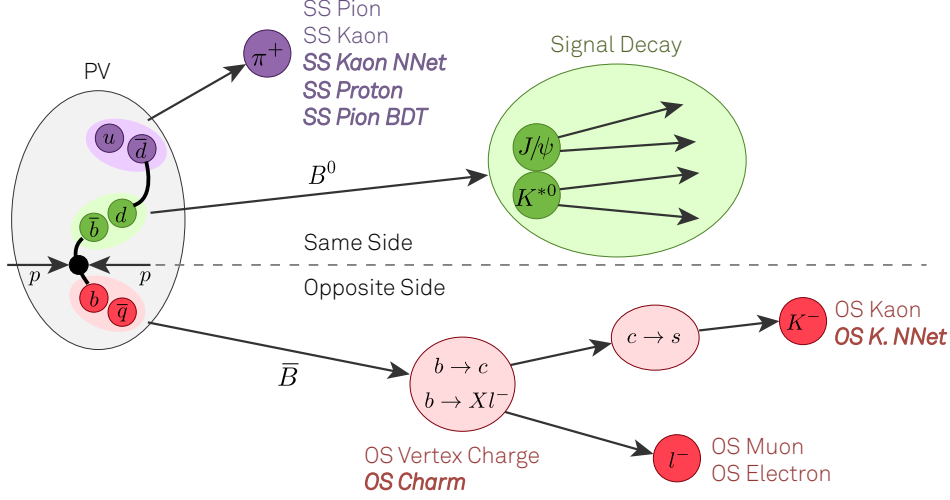
Figure 3.12: Schematic representation of the different sources of information available to tag the initial flavour of a signal B candidate at LHCb.

properties of the *b*-hadron decay: a large impact parameter significance with respect to the primary vertex (IP/σ_{IP}) and a large transverse momentum (p_T) are required, in combination with the particle identification given by the RICH, the calorimeter and the muon systems. Only charged particles reconstructed with a good quality of the track fit are used. In addition, to reject tracks coming from other primary interactions in the same bunch crossing, the impact parameter significance with respect to these pile-up (PU) vertices, defined as $IP_{PU}/\sigma_{IP_{PU}}$, is required to be large.

The vertex charge tagger is based on the inclusive reconstruction of the secondary vertex corresponding to the decay of the tagging *B* meson. A vertex candidate is built from two seed tracks above a p_T and IP/σ_{IP} threshold; the pion mass is attributed to each. Tracks that are compatible with coming from the two track vertex but do not originate from the primary vertex are added. A good quality of the vertex reconstruction is required. The probability that it originates from a *b*-hadron decay is estimated out the the fit quality, geometry and kinematics of the decay. The charge of the tagging *B* is calculated as the sum of the charges Q_i of all the tracks associated to the vertex weighted with their transverse momentum to the power of κ:

$$Q_{vtx} = \frac{\sum_i Q_i p_{Ti}^\kappa}{\sum_i p_{Ti}^\kappa} \qquad (3.3.7)$$

where $\kappa = 0.4$ is chosen to optimize the tagging power.

For each single particle tagger i, the probability η_i of the tag decision to be wrong is estimated by using properties of the tagger and of the event itself. This mistag probability is evaluated by means of a neural network trained on simulated events to identify the correct flavour of the signal *B*, and subsequently calibrated on data.

The inputs to the neural network are the transverse momentum of the signal B, the number of PU vertices, the number of tracks initially selected for the tagging candidate, other geometrical and kinematic properties of these tagging particles (such as p, p_T, IP/σ_{IP}). In Table 3.4 the performances of single particle taggers and the OS combination measured after the calibration of the mistag probability are reported.

The OS charm tagger is based on the reconstruction of the charm hadrons D^+, D^0 and Λ_c^+ produced through the quark level transition $b \to c$. The charge of the D^+ or Λ_c^+ determines the flavour of the parent b hadron, while for the D^0 decays trough the dominant process $D^0 \to K^- X$ (which is Cabibbo favoured), the kaon charge determines the flavour of the charm hadron and consequently of the parent b hadron (the D^0 mixing effect is negligible). This algorithm uses charm hadron candidates reconstructed in a set of decay modes with relatively large branching fractions. For each mode a boosted decision tree (BDT) [125][126] is used both to suppress background candidates and to extract mistag probabilities. The inputs to each BDT are variables that describe the decay kinematics, the decay vertex and the PID information of the decay products. These BDTs are trained on $b\bar{b}$ simulated events.

The tagging efficiency, mistag fraction and tagging power of the OS charm tagger are reported in Table 3.5 for $B \to J/\psi X$ decays and for the B_0^s decay of interest in this analysis.

Taggers	$\epsilon_{tag}[\%]$	$\omega[\%]$	$\epsilon_{eff}[\%]$
μ	4.8 ± 0.1	34.3 ± 1.9	0.48 ± 0.12
e	2.2 ± 0.1	32.4 ± 2.8	0.27 ± 0.10
K	11.4 ± 0.2	39.6 ± 1.2	0.49 ± 0.13
Q_{vtx}	14.9 ± 0.2	41.7 ± 1.1	0.41 ± 0.11
OS average ($\eta_c < 0.42$)	17.9 ± 0.2	36.8 ± 1.0	1.24 ± 0.2
OS sum of η_c bins	27.1 ± 0.3	38.0 ± 0.9	1.57 ± 0.22

Table 3.4: Tagging performance in the $B^0 \to D^{*-}\pi^+(\mu^+\nu_\mu)$ channel for single particle taggers and charge vertex taggers [123]. The performance of the OS combination is calculated rejecting the events with a poor calibrated mistag probability η_c (larger than 0.42). Additionally the tagging performance is determined in independent samples obtained by dividing the data in bins of η_c. Uncertainties are statistical only.

Sample	$\epsilon_{tag}[\%]$	$\omega[\%]$	$\epsilon_{eff}[\%]$
Simulation	4.88	37.0	0.33
$B^0 \to D^- \pi^+$	4.11 ± 0.03	$34.4 \pm 0.4 \pm 0.3$	$0.40 \pm 0.03 \pm 0.01$
$B_s^0 \to D_s^- \pi^+$	3.99 ± 0.07	$34.4 \pm 0.6 \pm 0.3$	$0.39 \pm 0.03 \pm 0.01$

Table 3.5: Tagging performance of the OS charm tagger algorithm [124]. The first uncertainties are statistical and the second are systematic. The sample labeled Simulation is the training sample of $B^+ \to J/\psi K^+$, $B^0 \to J/\psi K^{*0}$ and $B_s^0 \to J/\psi \phi$ decays, which has negligible statistical uncertainty.

3.3.2   Same Side Taggers

Same-side (SS) tagger algorithms [127][128] exploit the correlation between the flavour of the b-hadron and the charge of the particle (pion, proton, kaon) produced next to the signal b-hadron in the hadronisation process. In fact, through the production of a B^0 meson ($\bar{b}d$), an additional $\bar{d}$ is created, which can further hadronize into a pion or proton. Instead, the production of a B_s^0 meson ($\bar{b}s$) is accompanied by a $\bar{s}$, which can form a kaon. The SS pion, SS proton and SS kaon taggers exploit the formation of these particles to infer the flavour of the b hadron produced simultaneously. Both the SS pion and SS proton use a BDT to select suitable candidates [129], in contrast with the SS kaon, which employs a cut based selection.
A new SS kaon algorithm, SS kaon NNet [130], exploits two neural networks to identify the flavour at production of a reconstructed B_s^0 meson. The first neural network is used to assign to each track reconstructed in the pp collision the probability of being a particle related to the B_s^0 hadronisation process. Tracks that have a probability larger than a suitably chosen threshold are "combined" in the second network to determine the tagging decision and to estimate the probability of an incorrect flavour assignment. The tagging power of this new algorithm, as measured in $B_s^0 \to D_s^- \pi^+$ decays, is $(1.80 \pm 0.19(\text{stat}) \pm 0.18(\text{syst}))\%$ a significant improvement over the tagging power of 1.2% of the previous cut based implementation [130]. This new algorithm represents an important progress for many analyses aiming to make high-precision measurements of $B_s^0 - \bar{B}_s^0$ mixing and of CP asymmetries in B_s^0 decays.

3.3.3   Combination of taggers

The decisions provided by all the available taggers are combined into a final decision on the initial flavour of the signal B meson. The combined probability $P(b)$

that the signal meson contains a b quark is calculated as [123]

$$P(b) = \frac{p(b)}{p(b) + p(\bar{b})} \qquad P(\bar{b}) = 1 - P(b) \qquad (3.3.8)$$

where

$$p(b) = \prod_i \left(\frac{1 + d_i}{2} - d_i \left(1 - \eta_i\right) \right) \qquad p(\bar{b}) = \prod_i \left(\frac{1 - d_i}{2} + d_i \left(1 - \eta_i\right) \right) \quad (3.3.9)$$

Here, d_i is the decision taken by the i-th tagger based on the charge of the particle with the convention $d_i = 1(-1)$ for the signal B containing a $\bar{b}(b)$ quark and η_i the corresponding predicted mistag probability.

3.4 $B_{d,s}^0$ production at LHC

Heavy flavour production in hadronic collisions can be described in the parton model approach, where light partons in the incoming hadrons collide and produce a heavy $q\bar{q}$ pair via elementary strong interactions vertices [131], like, for example, in the diagrams of Figure 3.13.
Montecarlo (MC) simulations of $b\bar{b}$ production at $\sqrt{s} = 14\,\mathrm{TeV}$ at LHC were implemented using PYTHIA8 [132] and CTEQ6 NLO [133], including the following processes weighted according to their cross-sections:

$$q\bar{q} \to b\bar{b} \qquad gg \to b\bar{b} \qquad q\bar{q} \to b\bar{b}g \qquad gg \to b\bar{b}g$$

The total $b\bar{b}$ cross-section using the default PYTHIA8 parameters is $527.3\,\mu\mathrm{b}$ at $14\,\mathrm{TeV}$. As it is possible to observe from the results in Figure 3.14, the $b\bar{b}$ pairs are highly boosted. The LHCb pseudorapidity coverage, $1.8 < \eta < 4.9$, allows to intercept 24% of $b\bar{b}$ pairs and 27% of the b or $\bar{b}$ quarks [134].
Due to the quark confinement, b and $\bar{b}$ quarks can not exist as free particles: their long lifetime implies that bottom hadrons are formed and observed. The process where a b or a $\bar{b}$ quark forms a bound state with another quark is called hadronization. The primary products are B^+, B^0, B_s^0 and their charge-conjugate states, formed by one $\bar{b}$ quark bound to one of the three light quarks (u, d and s) [136]. The production cross-section for b-flavoured hadrons can be calculated in QCD [137, 138, 139] complemented with the knowledge of the hadronization fractions, defined as the probability for a b quark to hadronise as a particular bottom hadron [140]. Measurements of the cross-section for producing b quarks in the reaction $pp \to b\bar{b}X$ at 13 TeV center-of-mass energies are performed by LHCb, giving as result $\approx 560\,\mu\mathrm{b}$ in the full η and p_T range covered by the experiment [141]. Complete measurements of b hadron production fractions at the LHC do not exist yet for $\sqrt{s} = 13\,\mathrm{TeV}$
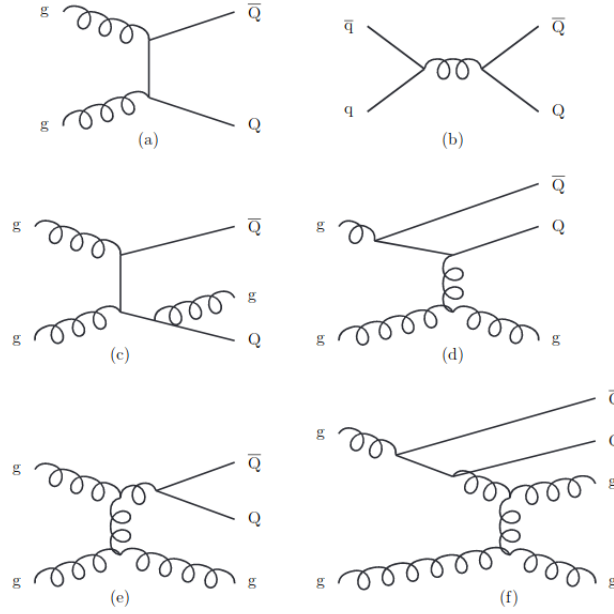
Figure 3.13: Examples of heavy flavour production diagrams. **(a,b)** Leading order. **(c)** Pair creation with gluon emission. **(d)** Flavour excitation. **(e)** Gluon splitting. **(f)** Events classified as gluon splitting but with flavour excitation character. Picture from [135].
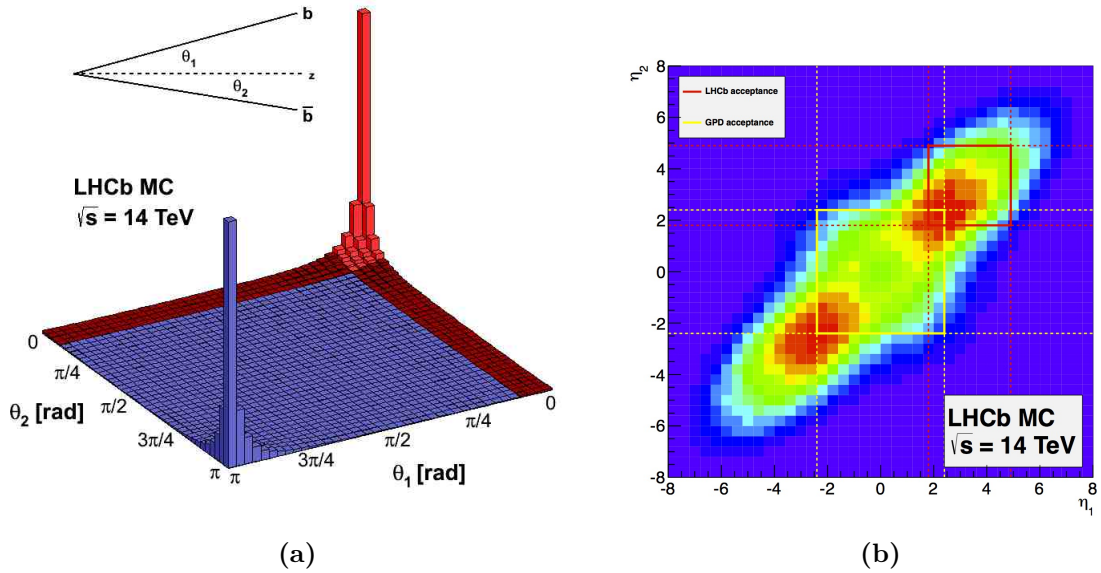

Figure 3.14: $b\bar{b}$ production angle and pseudorapidity at 14 TeV at LHC. The acceptance of LHCb is compared to that of a general purpose detector (GPD) with $|\eta| < 2$. Pictures from [134].

pp collisions. LHCb measured the hadronization fraction f_s of $\bar{B}_s^0$ normalized to the sum of the B^- fraction f_u and $\bar{B}^0$ fraction f_d, leading to $f_s/(f_u + f_d) = 0.122 \pm 0.006$ (stat and syst) at $\sqrt{s} = 13\,\text{TeV}$ [142]: the ratio shows a mild dependence on the p_T and no dependence on η.

In the Figures from 3.15 to 3.17 the most relevant kinematic properties of B_s^0 with daughters in the LHCb geometrical acceptance range, at $\sqrt{s} = 7\,\text{TeV}$, as obtained from a PYTHIA MC sample, are presented: they are the momentum and transverse momentum, the pseudorapidy, the azimuthal angle and the decay time. From Figure 3.15 it is possible to observe that the momentum of the B_s^0 is peaked around $50\,\text{GeV}$, while the transverse momentum reaches its maximum at $5\,\text{GeV}$. Due to the daughters in LHCb preselection B_s^0 particles have pseudorapidity between 2 and 5, while, as expected, the azimuthal angle is uniform in the $[0, 2\pi]$ range, see Figure 3.16. Finally, the decay time distribution, Figure 3.17, has an average of $1.5\,\text{ps}$. Clearly no flavour tagging information is used in the decay time reconstruction hence $B_s^0 - \bar{B}_s^0$ mixing is not evident. More details on this topic are given in Chapter 6.

In the following Figure 3.18, the number of tracks and the number of long tracks, *i.e.* those which have hits in the VELO and in all the T-stations, are presented: while the number of tracks is ≈ 150, the number of long tracks is ≈ 50 on average. Finally in Figure 3.19 the number of primary vertices is shown: 2.5 primary vertices can be found per event with the running conditions chosen by LHCb.

(a)

(b)
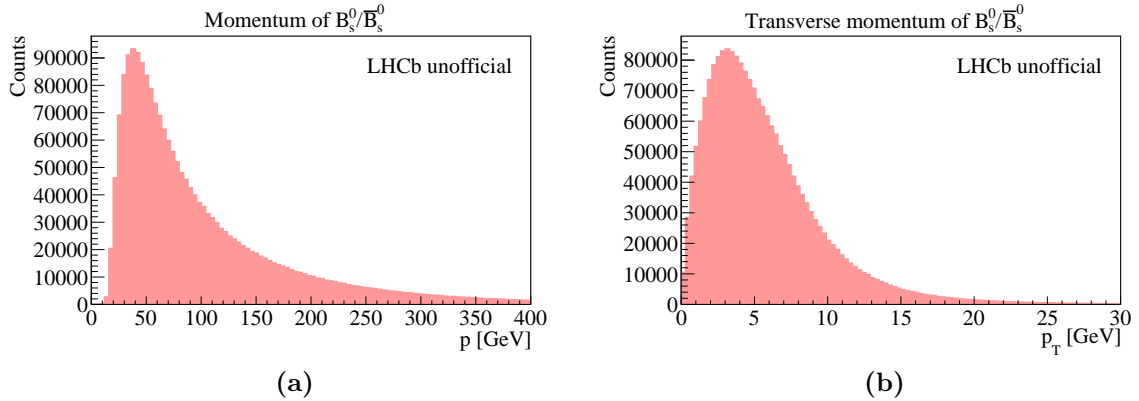
Figure 3.15: Momentum and transverse momentum of $B_s^0/\bar{B}_s^0$ in MC simulations at $\sqrt{s} = 7\,\text{TeV}$ at LHCb.
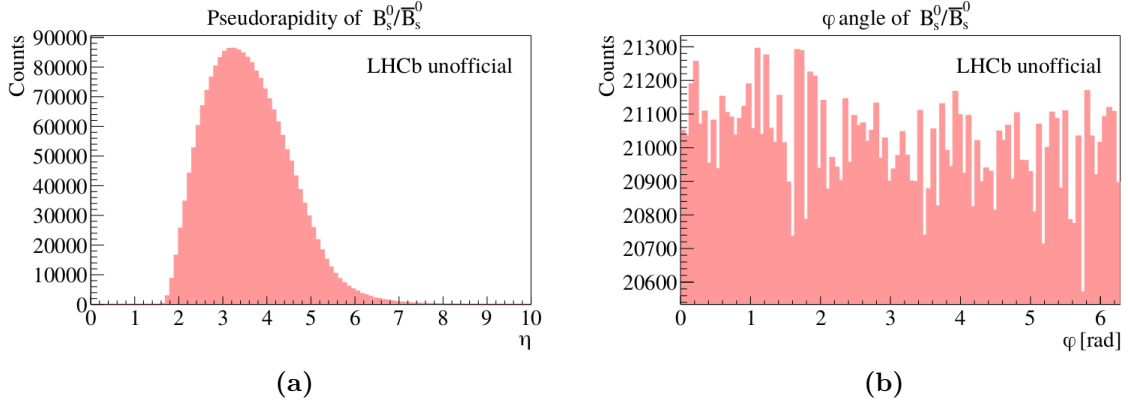
Figure 3.16: Pseudorapidity and azimuthal angle of $B_s^0/\bar{B}_s^0$ in MC simulations at $\sqrt{s} = 7\,\text{TeV}$ at LHCb.
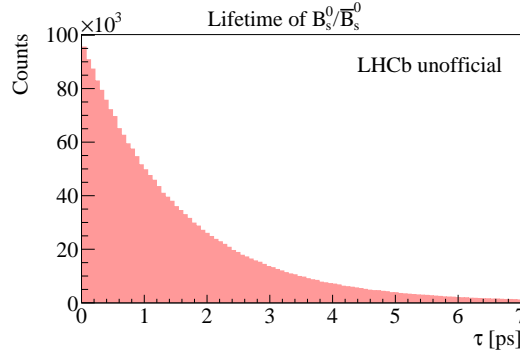
Figure 3.17: Decay time of $B_s^0/\bar{B}_s^0$ in MC simulations at $\sqrt{s} = 7\,\text{TeV}$ at LHCb.
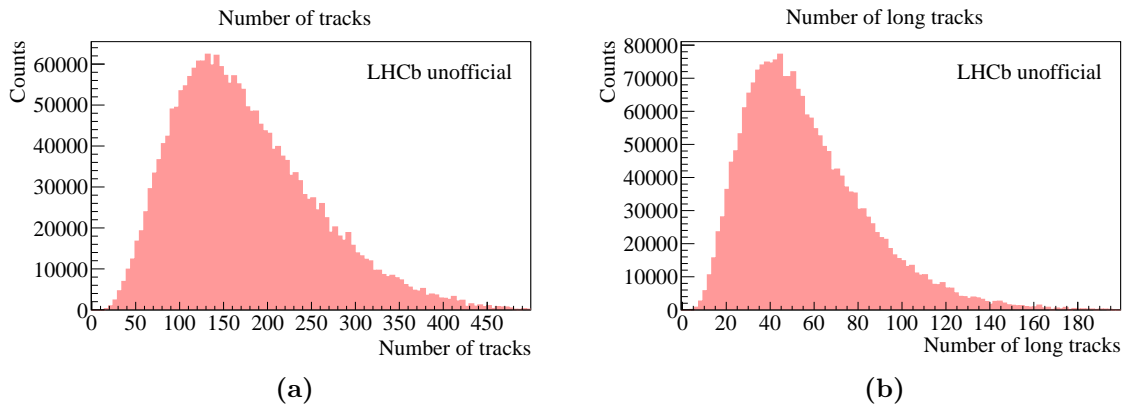
Figure 3.18: Number of tracks and long tracks in $B_s^0/\bar{B}_s^0$ events at $\sqrt{s} = 7\,\text{TeV}$.
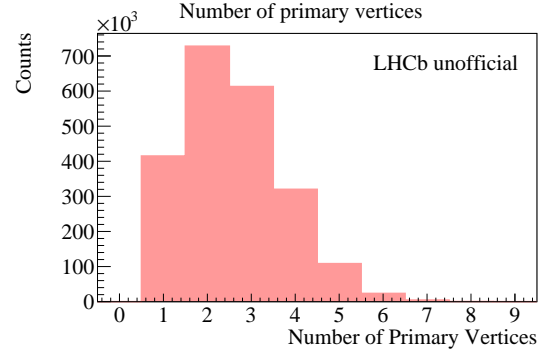
Figure 3.19: Number of primary vertices in $B_s^0/\bar{B}_s^0$ events at $\sqrt{s} = 7\,\text{TeV}$.

4 Analysis of the control channel $B_d^0 \rightarrow D^- \pi^+$

A measurement of Δm_s, as anticipated in Chapter 2, can be obtained from a time-dependent analysis of the $B_s^0 \rightarrow D_s^- \pi^+$ decay channel. In order to check the correct reconstruction of kinematic variables and validate the analysis procedure, a control sample is studied. In this case, the control sample is given by the $B_d^0 \rightarrow D^- \pi^+$ decay mode, where $D^- \rightarrow K^- \pi^+ \pi^-$. The charge conjugate mode is considered too. The analysis of the control sample foresees:

1. the modelling, by means of MC simulations, of the signal and background probability density functions (PDFs) for the invariant mass distribution to be subsequently used in fits to data;

2. a fit of the reconstructed $B_d^0 \rightarrow D^- \pi^+$ invariant mass distribution, to extract the signal and background yields and other important quantities, like the width of the signal peak;

3. the comparison between data and MC.

In Section 4.1, the functions used to model the signal and the various background contributions are described. In Section 4.2 the results of the invariant mass fits to the control channel $B_d^0 \rightarrow D^- \pi^+$ are reported for different subsets of Run 2 data. Finally in Section 4.3 some relevant kinematic quantities of this control sample, as measured in data, are compared to those obtained from the MC simulation.
The analysis uses a data sample corresponding to an integrated luminosity of $5.9\,\mathrm{fb}^{-1}$ collected by LHCb detector during Run 2.

4.1 Signal and background modelling

4.1.1 Signal fit in MC

Determining the invariant mass shape of the $D^- \pi^+$ system, *i.e.* the probability density function (PDF) that parameterizes the invariant mass, is crucial to describe this process accurately. Generally the best PDF function and its parameters are determined by means of MC simulations; the shape parameters extracted in MC are then fixed in the fits to data.
The shape of the B_d^0 invariant mass distribution for signal candidates is modelled using the Ipatia+JohnsonSU function. This choice provides a good description of

the peak region as well as of radiative tail and other reconstruction effects. More information about this choice can be found in [143].

The Ipatia function $H(m, \mu, \sigma_I, \lambda, \zeta, \beta, a_1, n_1, a_2, n_2)$ is a PDF with exponential tails and a core that follows a hyperbolic distribution [144]; it is defined as

$$
H \propto \begin{cases}
h(m, \mu, \sigma_I, \lambda, \zeta, \beta), & \text{if } \dfrac{m-\mu}{\sigma_I} > -a_1 \text{ or } \dfrac{m-\mu}{\sigma_I} < a_2 \\[2ex]
\dfrac{h(m - a_1\sigma_I, \mu, \sigma_I, \lambda, \zeta, \beta)}{\left[1 - m/\left(n \frac{h(m-a_1\sigma_I, \mu, \sigma_I, \lambda, \zeta, \beta)}{h'(m-a_1\sigma_I, \mu, \sigma_I, \lambda, \zeta, \beta)} - a_1\sigma_I\right)\right]^{n_1}}, & \text{if } \dfrac{m-\mu}{\sigma_I} \le -a_1 \\[4ex]
\dfrac{h(m - a_2\sigma_I, \mu, \sigma_I, \lambda, \zeta, \beta)}{\left[1 - m/\left(n \frac{h(m-a_2\sigma_I, \mu, \sigma_I, \lambda, \zeta, \beta)}{h'(m-a_2\sigma_I, \mu, \sigma_I, \lambda, \zeta, \beta)} - a_2\sigma_I\right)\right]^{n_2}}, & \text{if } \dfrac{m-\mu}{\sigma_I} \ge a_2
\end{cases}
$$

$$(4.1.1)$$

where

$$
h(m, \mu, \sigma_I, \lambda, \zeta, \beta) \propto \left[(m-\mu)^2 + A_\lambda^2(\zeta)\sigma_I^2\right]^{\frac{1}{2}\lambda - \frac{1}{4}} e^{\beta(m-\mu)} K_{\lambda - \frac{1}{2}}\left[\zeta\sqrt{1 + \left(\frac{m-\mu}{A_\lambda(\zeta)}\right)^2}\right]
$$

$$
A_\lambda(\zeta) = \frac{\zeta K_{\lambda(\zeta)}}{K_{\lambda+1}(\zeta)}
$$

where K_λ are cylindrical harmonics *i.e.* special Bessel functions of third kind. The JohnsonSU $J(m, \mu, \sigma_J, \nu\tau)$ is a function with highly asymmetric tails [145]; it is defined as

$$
J \propto \frac{1}{2\pi c(\nu\tau)\sigma_J} e^{\frac{1}{2} r(m,\mu,\sigma_J,\nu.\tau)^2} \frac{1}{\tau\sqrt{z(m,\mu,\sigma_J,\nu,\tau)^2 + 1}}
$$

$$(4.1.2)$$

where

$$
r = -\nu + \frac{\sinh(z^{-1})}{\tau}
$$

$$
z = \frac{m - [\mu + c + \sigma_J\sqrt{w}\sinh(\omega)]}{c\sigma_J}
$$

$$
c = \frac{1}{\sqrt{\frac{1}{2}(w-1)[w\cosh(2\omega) + 1]}}
$$

$$
\omega = -\nu\tau
$$

$$
w = e^{\tau^2}
$$

The mean μ of the two functions is shared when fitting the signal.

MC samples are generated using PYTHIA8 with a specific LHCb configuration [146]. Decays of hadronic particles are described by EVTGEN [147], in which final-state radiation is generated using PHOTOS [148]. The interaction of the generated particles with the detector and its response, are implemented using the GEANT4 toolkit
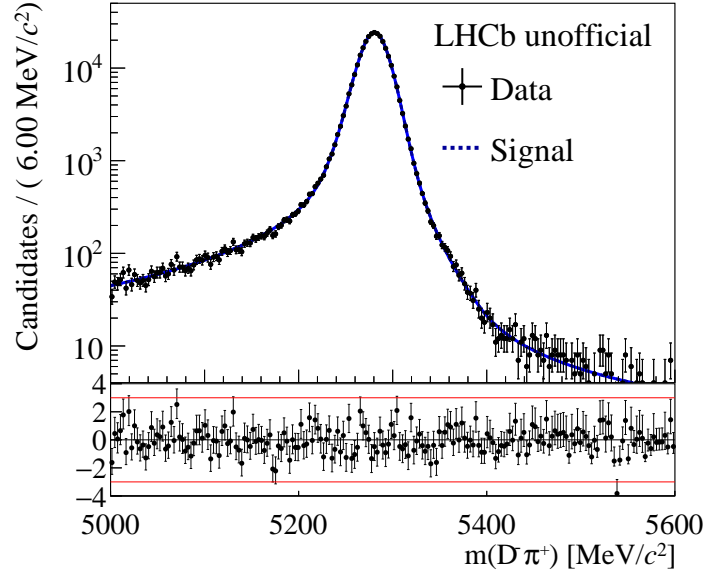
Figure 4.1: Signal shape fit of $B_d^0 \to D^- \pi^+$ in 2016 MC simulation.

[149, 150]. In Figure 4.1 the fit to the $B_d^0 \to D^- \pi^+$ 2016 MC signal is presented in a mass range from 5000 to 5600 MeV/c^2. In order to have an indication of how well the fit is performing "locally", a pull diagram is displayed underneath the fit. All the parameters are left free to vary, except β and ζ of the Ipatia function which are set to zero. Fitting this function gives a PDF that agrees with the simulation results very well, based on both the pull diagram, where we can see that in the vast majority of cases the deviations are under 3σ, and the reduced χ^2, equal to 0.76. The same fit has been performed also with the 2015 MC sample, with very similar results.

4.1.2   Background templates

In the invariant mass fits of the $D^- \pi^+$ candidates three different kind of background contributions can be distinguished:

- **Partially reconstructed backgrounds**: these background sources arise in decays where one or more particles in the final state are not reconstructed. These unreconstructed particles cause the partially reconstructed background events to have a lower invariant mass than the $B_d^0 \to D^- \pi^+$ signal.

- **Misidentified backgrounds**: if one of the final-state particles gets misidentified, the event ends up being reconstructed under an incorrect mass hypothesis as a $D^- \pi^+$ candidate.
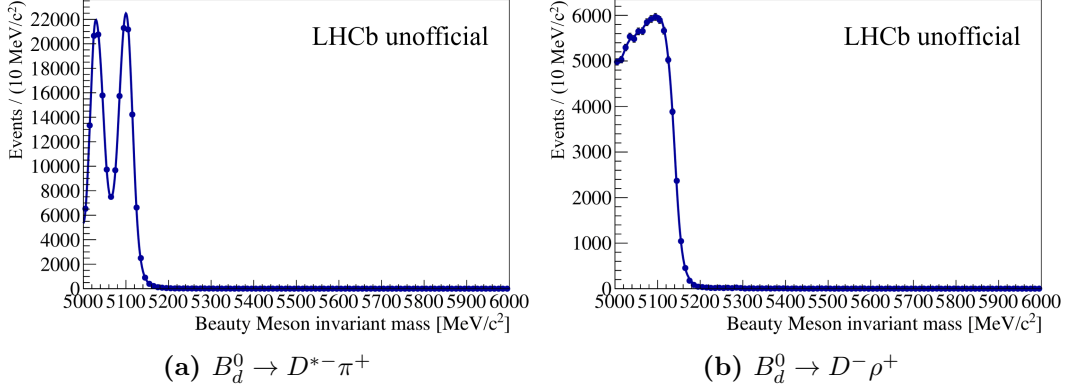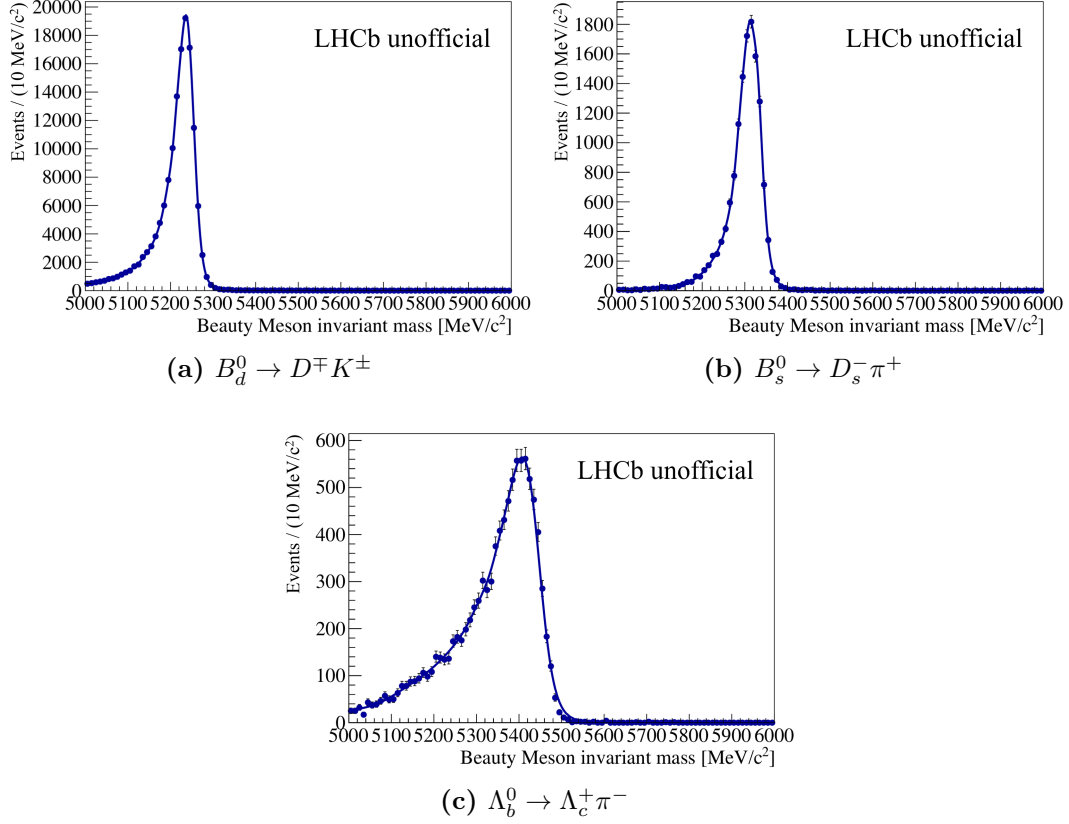
Figure 4.2: Partially reconstructed background templates for **(a)** $B_d^0 \to D^{*-}\pi^+$ and **(b)** $B_d^0 \to D^-\rho^+$ decay channels reconstructed as $B_d^0 \to D^-\pi^+$ candidates, which are used for $D^-\pi^+$ invariant mass fit.

- **Combinatorial background**: this background consists of random combinations of the final-state particles, resulting in $D^-\pi^+$ candidates. Two cases can occur: the first when a "genuine" D^- is randomly combined with a pion, the second when the D^- is reconstructed from a random combination of $K\pi\pi$ and is randomly combined with a pion.

The main contributions to the partially reconstructed background for the $B_d^0 \to D^-\pi^+$ are represented by $B_d^0 \to D^-\rho^+$, where $\rho^+ \to \pi^+\pi^0$, and $B_d^0 \to D^{*-}\pi^+$, where $D^{*-} \to D^-\pi^0$ or $D^{*-} \to D^-\gamma$. The main sources of misidentified background are the decay $B_d^0 \to D^\mp K^\pm$, where the kaon is reconstructed with the pion mass, the $\Lambda_b^0 \to \Lambda_c^+\pi^-$, where the $\Lambda_c^+ \to pK\pi$ is reconstructed as a combination of $K\pi\pi$ and thus it is identified as a D, and the $B_s^0 \to D_s^-\pi^+$, where similarly the D_s decay products are misidentified as a $K\pi\pi$ combination.

The partially reconstructed background and misidentified background contributions are described by functions called RooKeysPDF [151, 152], whose shapes are obtained fitting the corresponding simulation samples. The only exception is the $B_d^0 \to D^{*-}\pi^+$ PDF, which is described by a double Gaussian function with separated means. Finally the combinatorial background can be modelled with a double exponential function.

In Figures 4.2 and 4.3, an example of partially reconstructed background and misidentified background templates are reported. The blue points are obtained from the MC simulation of the corresponding process, while the solid blue line represents the PDF template.

(a) $B_d^0 \to D^{\mp} K^{\pm}$

(b) $B_s^0 \to D_s^- \pi^+$

(c) $\Lambda_b^0 \to \Lambda_c^+ \pi^-$

Figure 4.3: Misidentified background templates for **(a)** $B_d^0 \to D^{\mp} K^{\pm}$, **(b)** $B_s^0 \to D_s^- \pi^+$ and **(c)** $\Lambda_b^0 \to \Lambda_c^+ \pi^-$ decay channels reconstructed as $B_d^0 \to D^- \pi^+$ candidates, which are used for $D^- \pi^+$ invariant mass fit.

4.2 $B_d^0 \to D^- \pi^+$ invariant mass fits

4.2.1 Candidate selection

First of all, D^- candidates are reconstructed from a combination of charged particles in the final state, namely $K\pi\pi$. These D^- candidates are then associated with a fourth particle, which we refer to as "bachelor". Further selection criteria are applied to the reconstructed $B_d^0 \to D^- \pi^+$ candidates, the most important being listed below:

- The candidates undergo the decision of a gradient boosted decision tree (BDTG) algorithm [153], used to increase the signal purity by suppressing background from random combinations of particles. The algorithm is trained on $D_s\pi$ *sWeighted* data for the signal part and $D_s\pi$ candidates with invariant mass

above the nominal B_s^0 one for the background part.

- The B_d^0 and D^- candidates are required to have a measured mass within $[5000, 6000]\,\mathrm{MeV/c^2}$ and $[1830, 1920]\,\mathrm{MeV/c^2}$, respectively.

- The reconstructed B_d^0 decay time must be $\tau > 0.4\,\mathrm{ps}$, in order to avoid overlaps between the primary and the secondary vertex;

- The D candidates are required to be detached from the primary vertex, by imposing conditions on the flight distance.

Very similar cuts are applied also to the $D_s\pi$ channel.

4.2.2   Fit results

The Run 2 data sample after the selection is split into eight subsets, according to the different years of data-taking (2015, 2016, 2017, 2018) and the different orientation of the magnetic field, namely "polarity up" and "polarity down". This procedure allows to check the consistency and the stability of the invariant mass fits.

The invariant mass distributions of all the samples are fitted through a maximum Likelihood fit: the shape of the B_d^0 signal is modelled using the Ipatia+JohnsonSU PDF, as reported in Section 4.1. The parameters of the PDF are fixed to the values extracted from the MC signal fit, see Figure 4.1, with some exceptions: the mean μ and the parameters a_1, σ_I and σ_J are left free, in order to be able to cope with differences between data and MC, as well as to compare the left tail of the signal shape. Clearly also the yields of the signal component is a floating parameter.

The misidentified backgrounds, $B_d^0 \rightarrow D^\mp K^\pm$, $B_s^0 \rightarrow D_s^- \pi^+$ and $\Lambda_b^0 \rightarrow \Lambda_c^+ \pi^-$, and the partially reconstructed backgrounds, $B_d^0 \rightarrow D^{*-}\pi^+$ and $B_d^0 \rightarrow D^- \rho^+$, are modelled using MC templates, as explained in Section 4.1. Almost all background yields are left free to vary in the fit, except those that have an expected contribution below 2% of the signal yield, namely $B_s^0 \rightarrow D_s^- \pi^+$ and $\Lambda_b^0 \rightarrow \Lambda_c^+ \pi^-$. Such background yields are fixed from known branching fractions and relative efficiencies, as measured using simulation, and assuming an "initial" value for the signal yield. However being so small a perfectly legitimate fit is obtained also setting them at 0. The combinatorial background is modelled with a double exponential, with parameters free to vary.

In Figures from 4.4 to 4.7 the results of the invariant mass fits are reported: the mass distribution features a peak in correspondence to the known value of the B_d^0 mass, $\approx 5280\,\mathrm{MeV/c^2}$, with a width of about $20\,\mathrm{MeV/c^2}$. At values lower than $5200\,\mathrm{MeV/c^2}$, broad structures corresponding to partially reconstructed decays are present.

The fits allow to estimate the signal and background yields, both in the entire range

and in the signal range: in particular the yields in the signal range $[5229.63, 5329.63]\,\mathrm{MeV/c^2}$ are listed in Table 4.1 for samples with magnet polarity down and Table 4.2 for samples with magnet polarity up.

From these fits it is also possible to extract *sWeights*, obtained from the *sPlot* prescription [154], which allow to statistically subtract the background contributions. The values obtained for the Ipatia+JohnsonSU mean parameter from the eight subsets are shown in Figure 4.8. In the same plot also the values obtained from the 2015 and 2016 MC signal fit (such as the one presented in Figure 4.1) are displayed. This plot represents a useful cross check of the LHCb momentum scale calibration. The offset between the B_d^0 invariant mass reconstructed in MC and data amounts to only $\approx 2\,\mathrm{MeV/c^2}$. In addition a difference is visible between the 2018 down and up samples that could be recover improving the momentum scale calibration.

(a) Polarity down
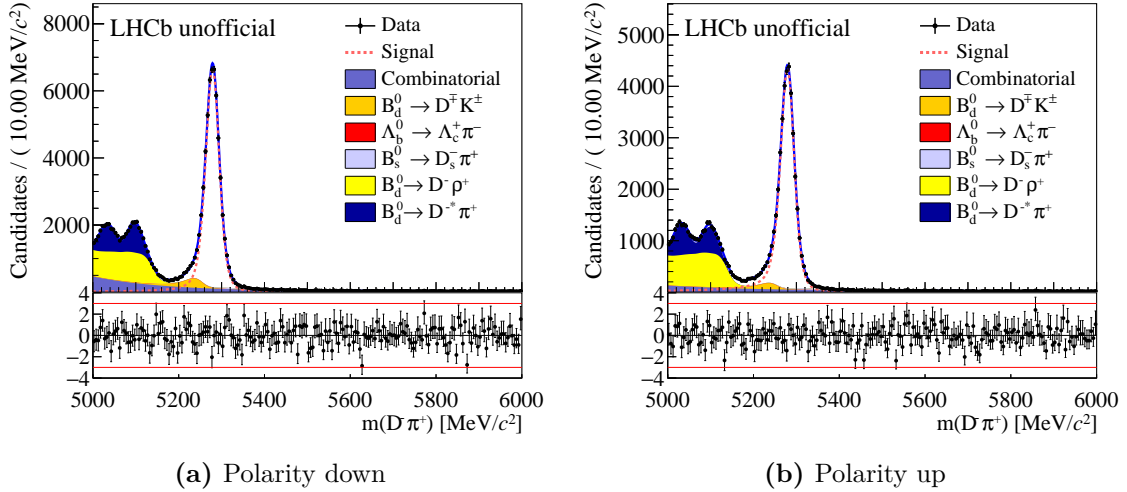
(b) Polarity up

Figure 4.4: Distributions of the B_d^0 invariant mass for $B_d^0 \to D^-\pi^+$ final states in the 2015 data sample, with magnet polarity down **(a)** and up **(b)**. The solid blue curve is the total result of the fit. The dotted red curve shows the $B_d^0 \to D^-\pi^+$ signal and the fully coloured stacked histograms show the different background contributions. Normalized residuals are shown underneath all the distributions.
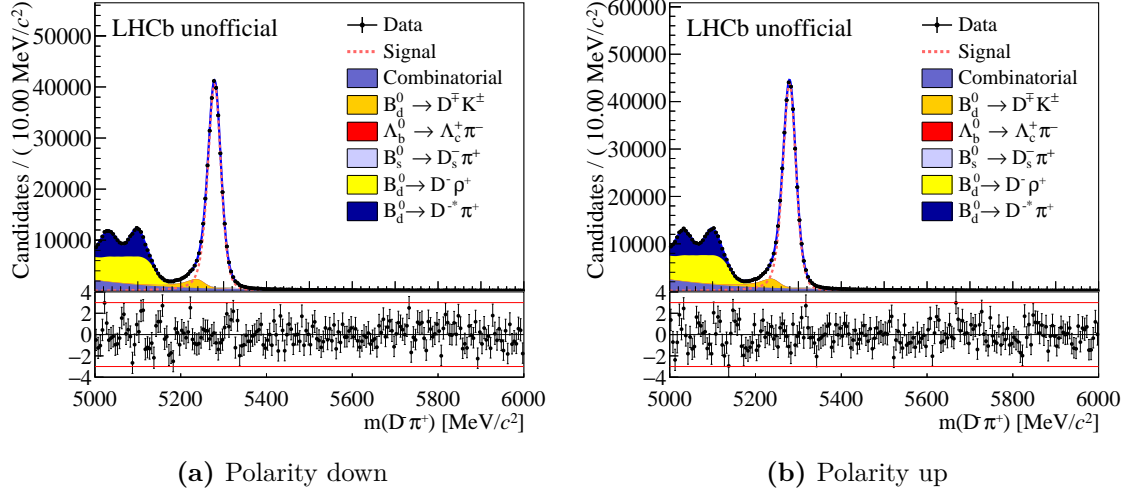
(a) Polarity down
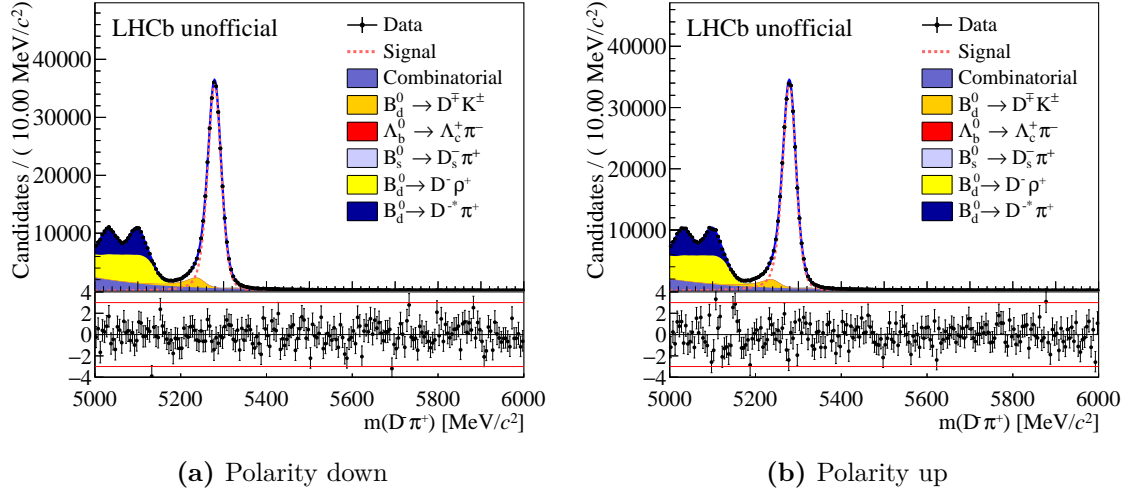
(b) Polarity up

Figure 4.5: Distributions of the B^0 invariant mass for $B_d^0 \to D^- \pi^+$ final states in the 2016 data sample, with magnet polarity down **(a)** and up **(b)**. The solid blue curve is the total result of the simultaneous fit. The dotted red curve shows the $B_d^0 \to D^- \pi^+$ signal and the fully coloured stacked histograms show the different background contributions. Normalized residuals are shown underneath all the distributions.


(a) Polarity down
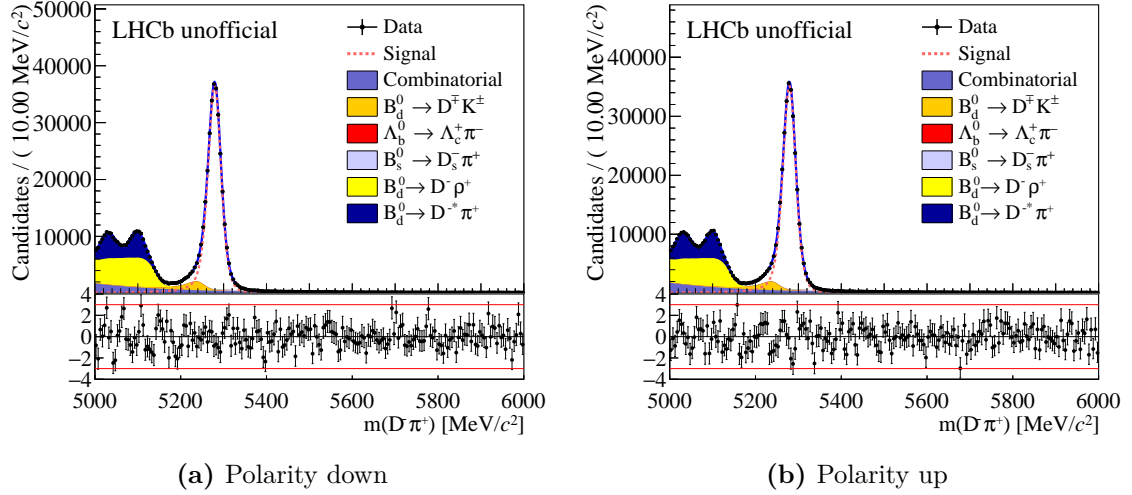
(b) Polarity up

Figure 4.6: Distributions of the B^0 invariant mass for $B_d^0 \to D^- \pi^+$ final states in the 2017 data sample, with magnet polarity down **(a)** and up **(b)**. The solid blue curve is the total result of the simultaneous fit. The dotted red curve shows the $B_d^0 \to D_s^- \pi^+$ signal and the fully coloured stacked histograms show the different background contributions. Normalized residuals are shown underneath all the distributions.

(a) Polarity down

(b) Polarity up

Figure 4.7: Distributions of the B_d^0 invariant mass for $B_d^0 \to D^-\pi^+$ final states in the 2018 data sample, with magnet polarity down **(a)** and up **(b)**. The solid blue curve is the total result of the simultaneous fit. The dotted red curve shows the $B_d^0 \to D_s^-\pi^+$ signal and the fully coloured stacked histograms show the different background contributions. Normalized residuals are shown underneath all the distributions.
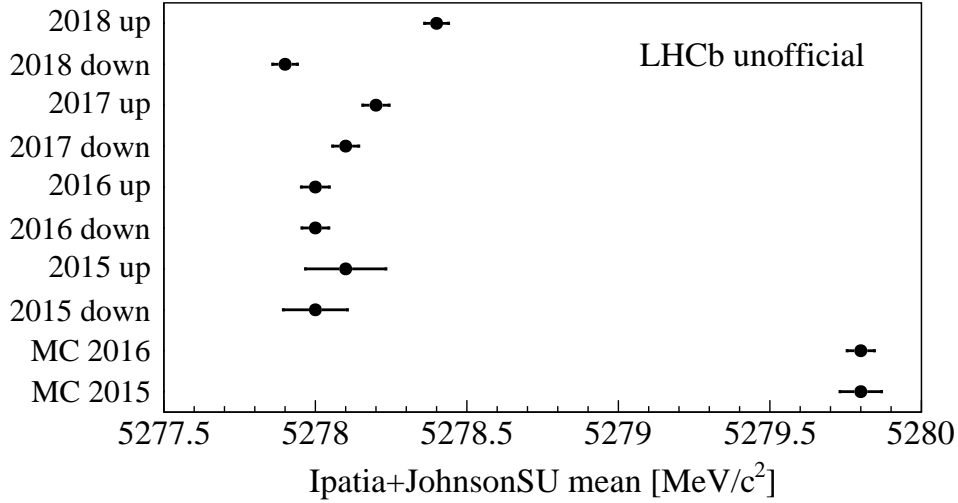
Figure 4.8: Results for the Ipatia+JohnsonSU mean obtained from the fits to $B_d^0 \to D^-\pi^+$ Run 2 data samples and MC simulations.

		Years			
		2015	2016	2017	2018
Yields	Signal (S)	55614.78	295551.47	295112.06	327778.20
	Background (B)	4255.03	23442.00	21143.75	24000.67
Performance	S/B	13.07	12.61	13.96	13.66
	S/$\sqrt{\text{S+B}}$	227.29	523.29	524.77	552.64

Table 4.1: Signal and background yields in range $[5229.63, 5329.63]\,\text{MeV/c}^2$ obtained from $B_d^0 \to D^- \pi^+$ invariant mass fits with dipole magnet polarity down.

|		Years			
		2015	2016	2017	2018
Yields	Signal (S)	37189.50	281055.92	284344.73	355179.23
	Background (B)	2112.41	20345.50	20464.36	26538.38
Performance	S/B	17.61	13.81	13.89	13.38
	S/$\sqrt{\text{S+B}}$	187.59	511.94	515.03	574.88

Table 4.2: Signal and background yields in range $[5229.63, 5329.63]\,\text{MeV/c}^2$ obtained from $B_d^0 \to D^- \pi^+$ invariant mass fits with dipole magnet polarity up.

4.3   Data to MC comparison

The goodness of the reconstruction of $B_d^0 \to D^- \pi^+$ candidates in Run 2 data can be checked by comparing the relevant kinematic quantities as measured in data with the MC simulation. The quantities chosen are: the momentum and transverse momentum of the B_d^0 and of the bachelor track, the pseudorapidity and the lifetime of the B_d^0, and finally the number of reconstructed tracks. These comparisons are made before and after applying a reweighting procedure. The reweighting method foresees that:

- data are background-subtracted using the *sWeights* extracted from the $B_d^0 \to D^- \pi^+$ invariant mass fits (see Section 4.2);

- MC simulation data are reweighted according to the ratio between data and MC histograms (normalized to unity) in the $\log(p_\pi)$-$\log$(number of tracks) plane. The .root files containing these ratios are "centrally" produced and shared by many analyses involving charmed mesons from B mesons decay.

The samples with magnet polarity up and down are kept separated in the analysis; furthermore, due to the low statistics recorded in 2015, the 2015 and 2016 data samples are merged. Figures 4.9 to 4.15 show the results of the comparisons for the down polarity samples; similar plots are obtained also for the up polarity. In general after the reweighting procedure the behaviour of the MC simulation gets more similar to the data. This improvement can be observed in particular in Figure 4.15, displaying the logarithm of the number of tracks; but also in Figure 4.12, that shows the B_d^0 lifetime, and in Figures 4.13 and 4.14, that show the logarithm of bachelor momentum and transverse momentum, around the peak of these distributions.
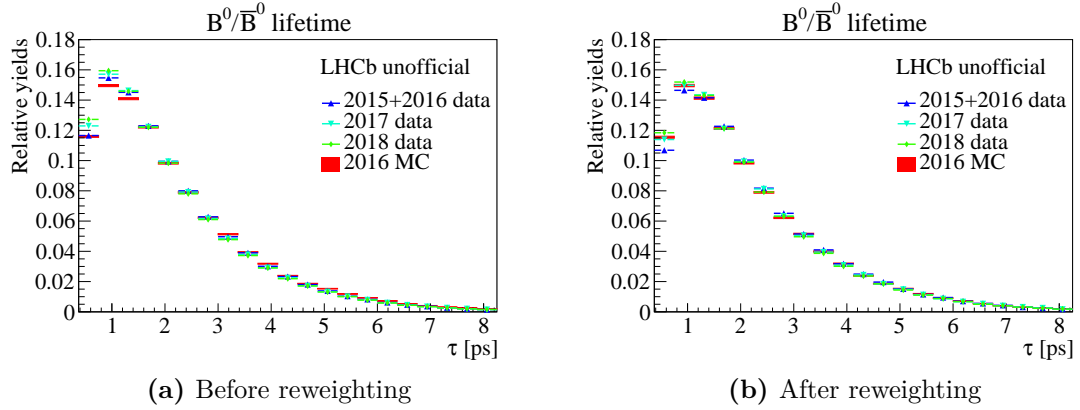

(a) Before reweighting   **(b)** After reweighting
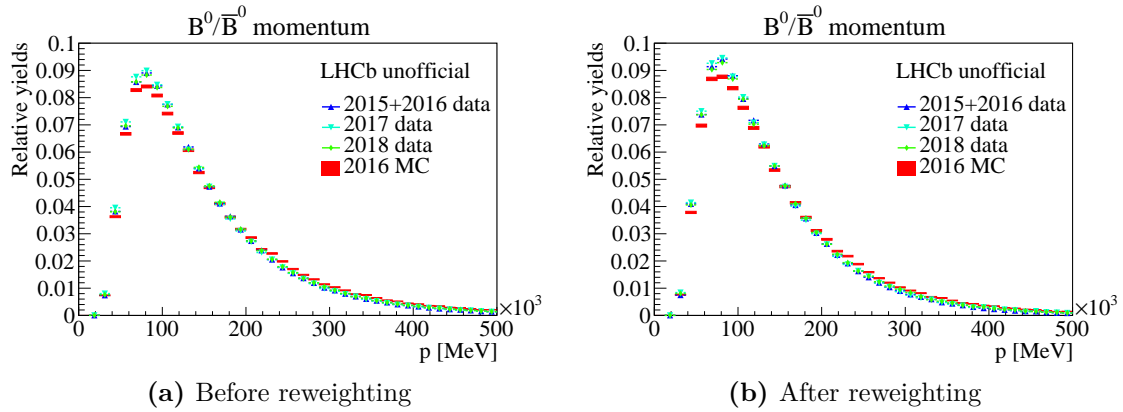
Figure 4.9: Reconstructed momentum of $B_d^0(\bar{B}_d^0) \to D^{\mp}\pi^{\pm}$ in Run 2 data and 2016 MC simulation with magnet polarity down, before reweighting **(a)** and after reweighting **(b)**.

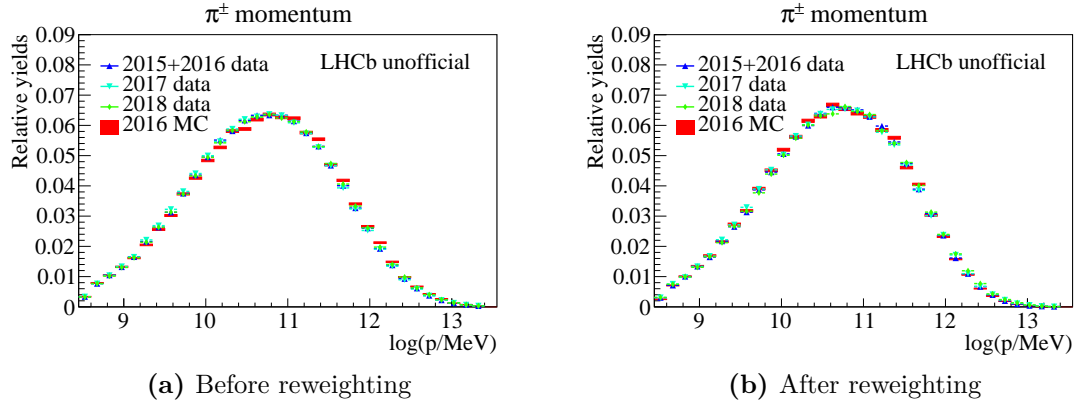**(a)** Before reweighting   **(b)** After reweighting
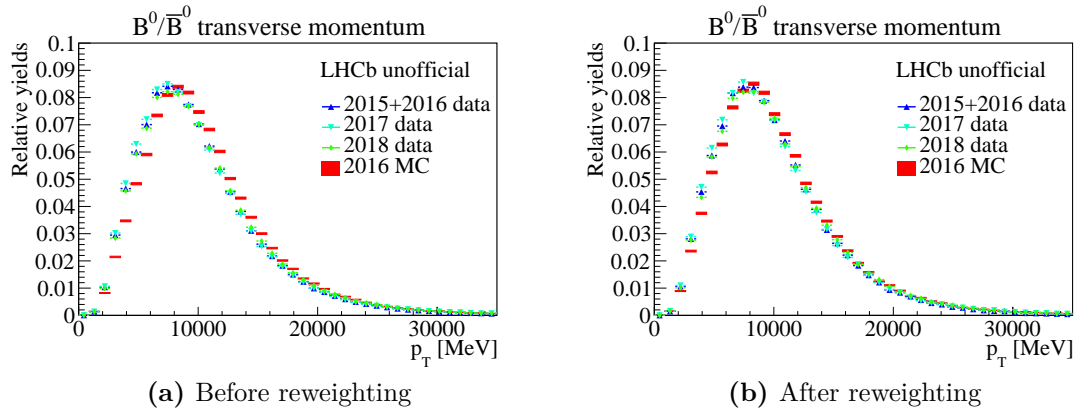
Figure 4.10: Reconstructed transverse momentum of $B_d^0(\bar{B}_d^0) \to D^{\mp}\pi^{\pm}$ in Run 2 data and 2016 MC simulation with magnet polarity down, before reweighting **(a)** and after reweighting **(b)**.

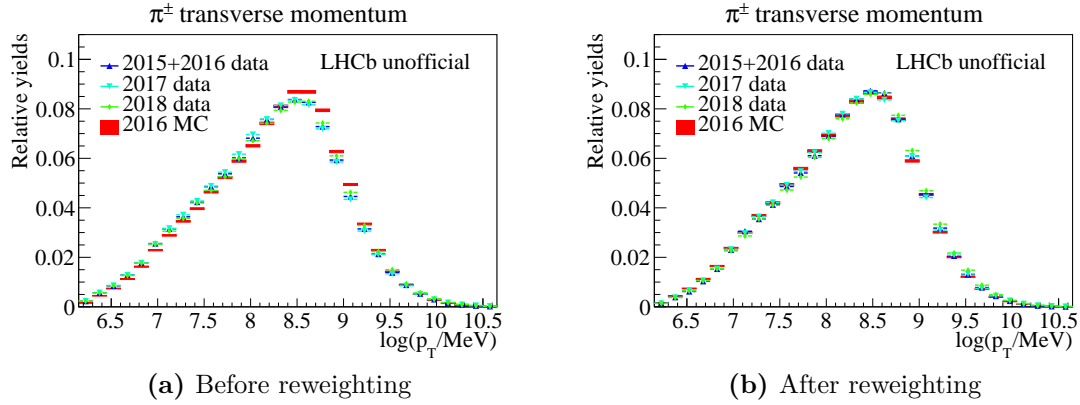**(a)** Before reweighting   **(b)** After reweighting
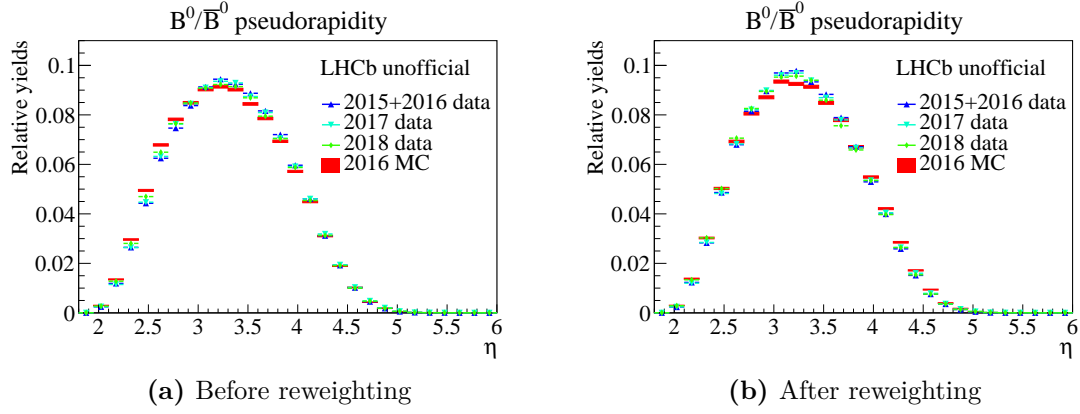
Figure 4.11: Reconstructed pseudorapidity of $B_d^0(\bar{B}_d^0) \to D^{\mp}\pi^{\pm}$ in Run 2 data and 2016 MC simulation with magnet polarity down, before reweighting **(a)** and after reweighting **(b)**.

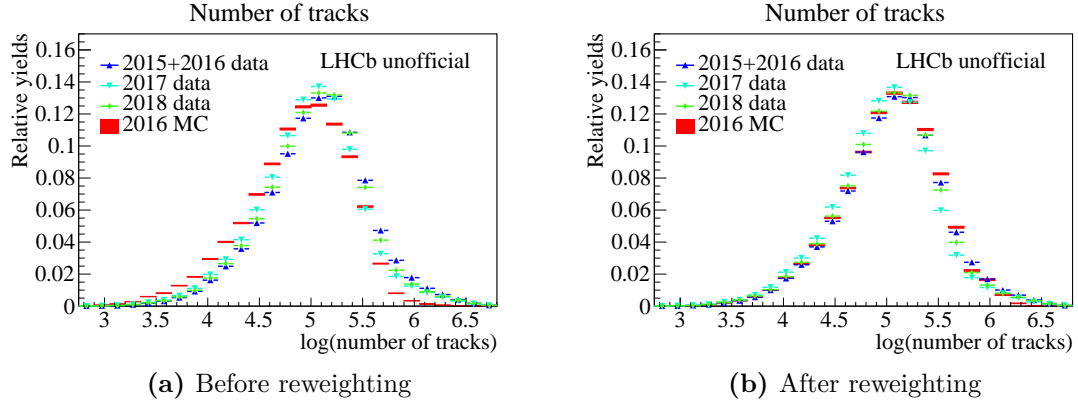**(a)** Before reweighting   **(b)** After reweighting

Figure 4.12: Reconstructed decay time of $B_d^0(\bar{B}_d^0) \to D^{\mp}\pi^{\pm}$ in Run 2 data and 2016 MC simulation with magnet polarity down, before reweighting **(a)** and after reweighting **(b)**.

(a) Before reweighting

(b) After reweighting

Figure 4.13: Reconstructed momentum of the bachelor particle of $B_d^0(\bar{B}_d^0) \rightarrow D^{\mp}\pi^{\pm}$ in Run 2 data and 2016 MC simulation with magnet polarity down, before reweighting **(a)** and after reweighting **(b)**.

(a) Before reweighting

(b) After reweighting

Figure 4.14: Reconstructed transverse momentum of the bachelor particle of $B_d^0(\bar{B}_d^0) \rightarrow D^{\mp}\pi^{\pm}$ in Run 2 data and 2016 MC simulation with magnet polarity down, before reweighting **(a)** and after reweighting **(b)**.

(a) Before reweighting

(b) After reweighting

Figure 4.15: Number of tracks reconstructed in $B_d^0(\bar{B}_d^0) \rightarrow D^{\mp}\pi^{\pm}$ in Run 2 data and 2016 MC simulation with magnet polarity down, before reweighting **(a)** and after reweighting **(b)**.

The reweighting procedure has been performed also according to the $\log(p_{T\pi})$-$\log$(number of tracks) plane, with similar results.

5 Analysis of $B_s^0 \to D_s^- \pi^+$

The measurement of Δm_s is performed at LHCb in the $B_s^0 \to D_s^- \pi^+$ decay channel. This Cabibbo-favoured decay mode has a large branching fraction, $\mathcal{B} = (3.00 \pm 0.23) \times 10^{-3}$ [27], and can be reconstructed with a large signal to background ratio. It is also a flavour-specific decay. Thus this high-statistics channel is well suited for Δm_s measurements [155]. Moreover, it can be used as control channel in time-dependent analyses of non flavour-specific B_s^0 decays, such as for the measurement of γ in the $B_s^0 \to D_s^\mp K^\pm$ decay mode, as mentioned in Chapter 2.
The analysis strategy foresees firstly the fit to the invariant mass of the $B_s^0 \to D_s^- \pi^+$ candidates, presented in Section 5.2, after a selection procedure described in Section 5.1. From the mass fits *sWeights* are extracted and applied to data in order to statistically subtract backgrounds. Then, in order to perform a measurement of Δm_s, a decay time fit is performed, as illustrated in Section 5.3.

5.1 Candidate selection

The B_s^0 candidates are reconstructed in the flavour-specific decay mode $B_s^0 \to D_s^- \pi^+$, where the D_s^- are reconstructed in five decay modes, namely $D_s^- \to \phi(K^+ K^-)\pi^-$, $D_s^- \to K^{*0}(K^+\pi^-)K^-$, $D_s^- \to K^+ K^- \pi^-$ nonresonant, $D_s^- \to K^- \pi^+ \pi^-$ and $D_s^- \to \pi^- \pi^+ \pi^-$. Unless explicitly stated, the inclusion of charge-conjugated modes is always implied.
Different criteria are taken into account for the candidate selection, such as:

- a boosted decision tree algorithm, BDTG, particularly effective in separating signal from background contributions. This is the algorithm already introduced in Section 4.2;

- the reconstructed invariant mass of the B_s^0 candidates must be in the mass range $[5300, 5800]\,\mathrm{MeV/c^2}$; at the same time, the D_s candidates are required to have a measured mass within $[1930, 2015]\,\mathrm{MeV/c^2}$;

- the reconstructed B_s^0 decay time must be $\tau > 0.4\,\mathrm{ps}$, in order to avoid overlaps between the primary and the secondary vertex;

- the D_s candidate must be detached from the primary vertex, as obtained by imposing conditions on the flight distance.

A combination of tagging algorithms is applied to identify the flavour of the B_s^0 at production. These algorithms provide a tagging decision for each candidate, together

with an estimate of the probability of a wrong assignment (mistag probability). Flavour tagging algorithms have been described in Section 3.3.

Additional requirements are applied on the sum of the p_T of the B_s^0 candidate's decay products, on particle identification variables and on track and vertices quality.

5.2 $B_s^0 \to D_s^- \pi^+$ invariant mass fits

The fit to the invariant mass of the $B_s^0 \to D_s^- \pi^+$ candidates proceeds in a very similar way to what described in Chapter 4 for the $B_d^0 \to D^- \pi^+$ invariant mass fit. Here the shape of the B_s^0 invariant mass distribution for signal candidates is modelled using a double Crystal Ball function [156] *i.e.* the sum of two Crystal Ball functions which are constrained to have the same mean value. The Crystal Ball PDF $C(m, \alpha, n, \mu, \sigma)$ is defined as

$$C \propto \begin{cases} \exp\left[-\dfrac{(m-\mu)^2}{2\sigma^2}\right], & \text{if } \dfrac{m-\mu}{\sigma} > -\alpha \\[2ex] A \cdot \left(B - \dfrac{m-\mu}{\sigma}\right)^{-n}, & \text{if } \dfrac{m-\mu}{\sigma} \leq -\alpha \end{cases} \tag{5.2.1}$$

where

$$A = \left(\frac{n}{|\alpha|}\right)^n \cdot \exp\left(-\frac{|\alpha|^2}{2}\right)$$

$$B = \frac{n}{|\alpha|} - |\alpha|$$

The parameters of the double Crystal Ball function describing the tails are fixed in the fit to the values obtained from the MC simulation, whereas the mean and the two widths are allowed to vary.

The fit to the beauty, B_s^0, and charm, D_s, masses are performed simultaneously. The shape of the D_s invariant mass distribution is similarly described by a double Crystal Ball. The main sources of background in this channel are:

- Misidentified backgrounds: the $B_s^0 \to D_s^\mp K^\pm$, where the kaon is reconstructed with the mass of the pion; the $\Lambda_b^0 \to \Lambda_c^+ \pi^-$, where the $\Lambda_c^+ \to pK\pi$ is reconstructed as a combination of K and π and thus identified as a D_s; the $B_d^0 \to D^- \pi^+$, where one of the D decay tracks is misidentified and hence the D meson reconstructed as a D_s;

- Partially reconstructed backgrounds: the $B_{d,s}^0 \to D_s^{*-} \pi^+$, where the D_s^* decays ejecting a π^0 or a γ, which are not reconstructed in the final state;

- Combinatorial backgrounds.
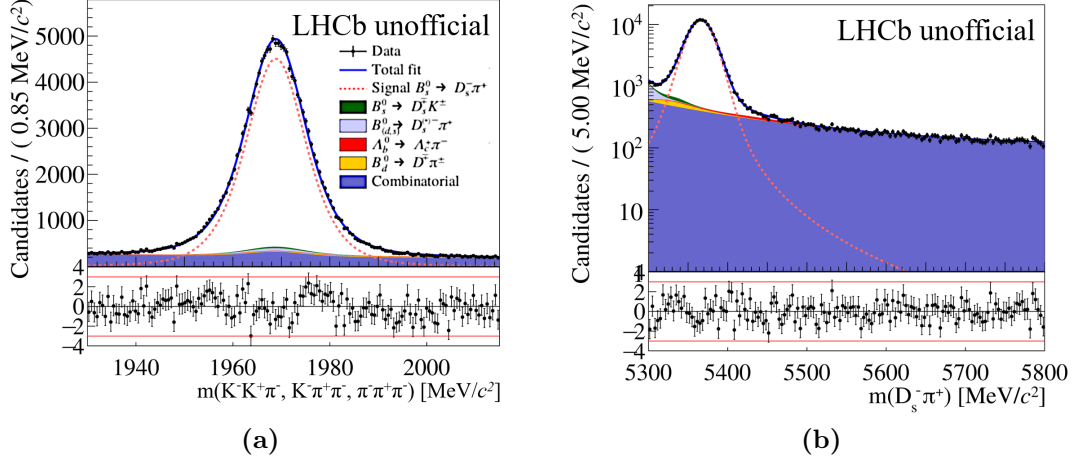
Figure 5.1: Distribution of the B_s^0 **(a)** and the D_s^- **(b)** invariant masses for $B_s^0 \to D_s^- \pi^+$ final states for the full Run 2 dataset. The contributions for all from all D_s^- final states are combined. The solid blue curve is the total result of the simultaneous fit. The dotted red curve shows the $B_s^0 \to D_s^- \pi^+$ signal and the fully coloured stacked histograms show the different background contributions. Normalized residuals are shown underneath all the distributions.

The background shapes are fixed from MC simulation. Almost all background yields are left free to vary, except those that have an expected contribution below 2% of the signal yield.

The *sPlot* technique allows to extract *sWeights*, which are used in the following Section to statistically subtract all background sources.

The results of the simultaneous fit are shown in Figure 5.1.

5.3 $B_s^0 \to D_s^- \pi^+$ decay time fits

5.3.1 Decay time description

The decay time distributions of B_s^0 and $\bar{B}_s^0$ to the same final state f are described by Equations (2.1.22) and (2.1.23), respectively. These expressions depend on the CP violating parameters D_f, C_f, S_f defined in Equation (2.1.24). The CP-conjugate final states $f = D_s^- \pi^+$ and $\bar{f} = D_s^+ \pi^-$ are flavour specific for B_s^0 and $\bar{B}_s^0$, *i.e.* the B_s flavour at decay is known from the charge of its decay products. No CP violation occurs in the interference between mixing and decay. The CP violating parameters can be set to the value

$$C_f = 1 \qquad S_f = 0 \qquad D_f = 0$$

Thus the theoretical distribution of the decay time gets modified with respect to Equations (2.1.22) and (2.1.23) and the PDF can be written as

$$\mathcal{P}_{t(B_s^0)} \propto \frac{e^{-\Gamma_s t}}{2} \left[\cosh\left(\frac{\Delta\Gamma_s t}{2}\right) + \cos(\Delta m_s t) \right] \theta(t) \tag{5.3.1}$$

$$\mathcal{P}_{t(\bar{B}_s^0)} \propto \frac{e^{-\Gamma_s t}}{2} \left[\cosh\left(\frac{\Delta\Gamma_s t}{2}\right) - \cos(\Delta m_s t) \right] \theta(t) \tag{5.3.2}$$

where the Heaviside step function $\theta(t)$ is introduced to restrict the PDF to positive decay times only.

To determine the flavour of the B_s^0 meson at production, both OS and SS tagging algorithms, as described in Chapter 3, are used. The decisions given by both tagging algorithms have a certain probability of being incorrect; each tagging algorithm provides an estimate for the mistag probability, η. The true mistag probability, ω, can be parameterized as a linear function of the predicted mistag probability as shown in Equation (3.3.4). The calibration is performed separately for the OS and SS taggers. The calibration parameters $(p_0, p_1)_{OS}$ and $(p_0, p_1)_{SS}$ are allowed to vary in the fit. The average mistag fraction, $\bar{\eta}$, is fixed, for both OS and SS taggers, to the value corresponding to the mean of the η distribution. Taking into account the tagging decisions and the mistag estimate, the decay time PDF can be written as

$$\mathcal{P}_t \propto \frac{e^{-\Gamma_s t}}{2} \left[\cosh\left(\frac{\Delta\Gamma_s t}{2}\right) + d\,(1 - 2\omega)\cos(\Delta m_s t) \right] \theta(t)\epsilon_{tag} \tag{5.3.3}$$

where ϵ_{tag} gives the fraction of candidates with a tagging decision d.

In order to account for detector resolution effects, the decay time PDF is convolved with a Gaussian distribution $G\left(t, 0, S_{\sigma_t}\sigma_t\right)$. The uncertainty σ_t is taken from an event-by-event estimate returned by the fitting algorithm that reconstructs the B_s^0 decay vertex. This approach requires the estimated per-candidate decay time uncertainty to be calibrated. The calibration is performed using prompt D_s^- mesons, each combined with a random π^+ track, to form "fake B_s^0" candidates. The decay time distribution of these "fake B_s^0" candidates has, "by construction", a true lifetime of zero. This distribution is then fitted with a Gaussian function providing a scale factor S_{σ_t} such that G models the correct resolution.

Some of the selection criteria influence the shape of the decay time distribution, *e.g.* the requirement of a large impact parameter for the B_s^0 daughter tracks. Thus, a time-dependent efficiency, called "acceptance" in the following, has to be taken into account. The decay time acceptance function $\varepsilon_t(t)$ is described by *splines* [157]. The splines boundaries, or *knots*, are chosen in order to model reliably the features of the acceptance shape, and are placed at 0.5, 1.0, 1.5, 2.0, 3.0 and 12.0 ps. The parameterization is first determined from simulation; the parameters describing the

shape are then allowed to vary in the fit to the data.

Taking into account resolution and decay time acceptance, the PDF given in Equation (5.3.3) is modified to

$$\mathcal{P}(t|\sigma_t) \propto \frac{e^{-\Gamma_s t}}{2} \left[\cosh\left(\frac{\Delta\Gamma_s t}{2}\right) + d\left(1 - 2\omega\right)\cos(\Delta m_s t) \right] \theta(t)\epsilon_{tag} \otimes G\left(t, 0, S_{\sigma_t}\sigma_t\right) \varepsilon_t\left(t\right)$$

5.3.2 Fit Results

The $B_s^0 \to D_s^- \pi^+$ candidates are divided in three datasets, corresponding to the years of data taking "2015+2016", "2017", "2018". The integrated luminosity of each sample is $2.00\,\mathrm{fb}^{-1}$, $1.81\,\mathrm{fb}^{-1}$ and $2.19\,\mathrm{fb}^{-1}$ respectively. The background is statistically subtracted by weighting the candidates according to the *sWeights* computed with the mass fit, see Section 5.2. The *sFit* procedure [158], which is an extension of the *sPlot* technique, is applied to perform the decay time fit.

In addition to the parameters discussed in the previous Section, other quantities are fixed in the fit: Γ_s is set to be constant at $0.664\,\mathrm{ps}^{-1}$ while $\Delta\Gamma_s$ is fixed to $-0.083\,\mathrm{ps}^{-1}$. Both are HFLAV average values [159]. The favour tagging calibration parameters, p_0 and p_1, the *splines* coefficients and Δm_s are allowed to vary in the fit.

At this stage, the measurement of Δm_s is "blinded", meaning that the fitted value of Δm_s is hidden to the analysts. However the associated statistical error is available. The results obtained for the statistical error of Δm_s from the three different data samples are reported in Table 5.1. The average statistical error, calculated as the standard error of the weighted mean of the three measurements, is equal to $0.0051\,\mathrm{ps}^{-1}$. This value is one order of magnitude lower than the statistical error of the previous LHCb measurement, see Equation (2.3.1). It is instead comparable to the systematical error of that measurement, whose major contributions are:

- **z-scale**: it is related to the imperfect knowledge of the longitudinal (z) scale of the detector. It is estimated by evaluating the track distribution in the vertex detector.

- **Momentum scale**: it is evaluated by an independent study using mass measurements of well-known resonances.

- **Decay time bias**: this uncertainty is given by the track reconstruction and the selection procedure. It is estimated by fitting the decay time distribution of "fake B_s^0" candidates, with a similar procedure to that described in the previous Section.

In Table 5.2 the calibration parameters of the OS and SS taggers obtained from the fits are listed: as expected the differences $p_0 - \bar{\eta}$ and $p_1 - 1$ are both close to zero,

see Section 3.3.

Finally, in Figures 5.2 to 5.4 the results of the *sFit* are shown. In the same plots, the decay time acceptance function is displayed.

|	$\Delta m_s \pm \sigma_{\Delta m_s}\,[\mathrm{ps}^{-1}]$
2015 + 2016	XXX ± 0.0093
2017	XXX ± 0.0095
2018	XXX ± 0.0081
Average	**XXX ± 0.0051**

Table 5.1: Results of Δm_s statistical errors in different Run 2 data samples and their average.

Data sample	Tagger	$\bar{\eta}$	$p_0 \pm \sigma_{p_0}$	$p_1 \pm \sigma_{p_1}$	ϵ_{tag}
2015 + 2016	OS	0.4432	0.4775 ± 0.0053	0.9646 ± 0.0321	0.3817
	SS	0.4694	0.4725 ± 0.0046	0.7729 ± 0.0423	0.6896
2017	OS	0.3698	0.3878 ± 0.0069	0.9478 ± 0.0593	0.3715
	SS	0.4374	0.4487 ± 0.0043	0.8057 ± 0.0457	0.6393
2018	OS	0.3544	0.3822 ± 0.0054	0.9307 ± 0.0491	0.3973
	SS	0.4393	0.4537 ± 0.0044	0.8311 ± 0.0459	0.6942

Table 5.2: Set of calibration parameters for OS and SS taggers, for different Run 2 data samples. The average mistag $\bar{\eta}$ and the tagging efficiency ϵ_{tag} are fixed in the fit.
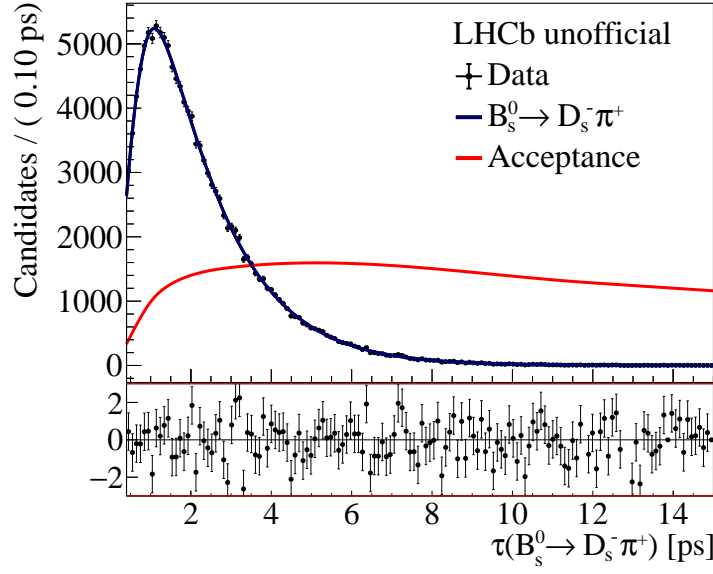
Figure 5.2: Decay-time distribution of $B_s^0 \to D_s^- \pi^+$ candidates in the 2015+2016 data sample. The solid blue curve is the result of the *sFit* procedure and the solid red curve shows the decay-time acceptance in arbitrary units.
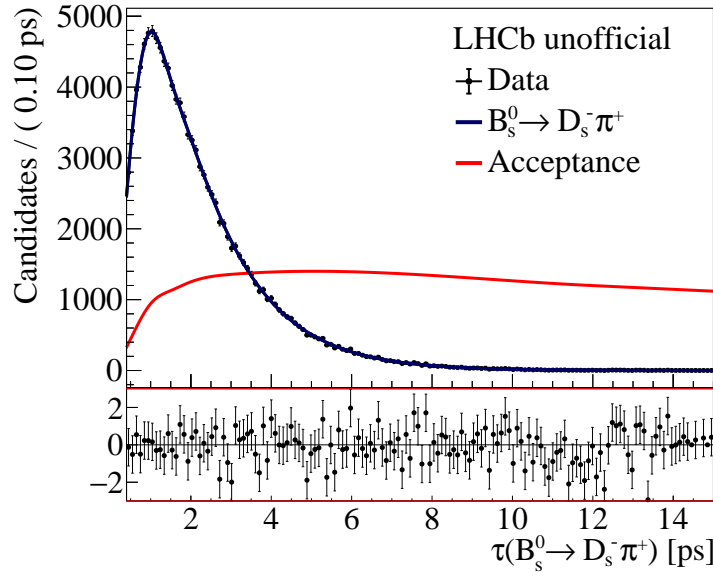
Figure 5.3: Decay-time distribution of $B_s^0 \to D_s^- \pi^+$ candidates in the 2017 data sample. The solid blue curve is the result of the *sFit* procedure and the solid red curve shows the decay-time acceptance in arbitrary units.
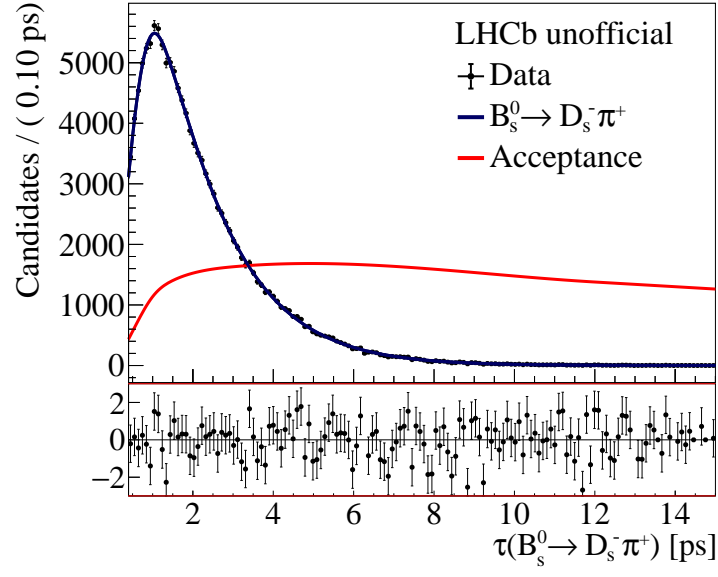
Figure 5.4: Decay-time distribution of $B_s^0 \rightarrow D_s^- \pi^+$ candidates in the 2018 data sample. The solid blue curve is the result of the *sFit* procedure and the solid red curve shows the decay-time acceptance in arbitrary units.

6 B_s^0 time-dependent CP asymmetry

In the $B_s^0 - \bar{B}_s^0$ system the flavor eigenstates are not the same as the mass eigenstates, as discussed in Chapter 2. The mass difference between the heavy and light mass eigenstates, namely Δm_s, determines the frequency of the oscillations between the flavour eigenstates. However, from the decay time distributions presented in Chapter 5 the oscillation phenomenon is not evident, since the information provided by the flavour taggers is not added to the fit. The mixing effect can be highlighted with the so called decay time asymmetries, which are the subject of this Chapter. The asymmetries are built distinctly for the two CP-conjugate final states considered also in Chapter 5, $D_s^-\pi^+$ and $D_s^+\pi^-$, folding the decay time distribution in one mixing period, $2\pi/\Delta m_s$:

$$\mathcal{A}_{mix}(D_s^-\pi^+) = \left[\frac{\tau(B_s^0 \to D_s^-\pi^+) - \tau(\bar{B}_s^0 \to D_s^-\pi^+)}{\tau(B_s^0 \to D_s^-\pi^+) + \tau(\bar{B}_s^0 \to D_s^-\pi^+)}\right] \text{modulo} \left(\frac{2\pi}{\Delta m_s}\right) \quad (6.0.1)$$

$$\mathcal{A}_{mix}(D_s^+\pi^-) = \left[\frac{\tau(B_s^0 \to D_s^+\pi^-) - \tau(\bar{B}_s^0 \to D_s^+\pi^-)}{\tau(B_s^0 \to D_s^+\pi^-) + \tau(\bar{B}_s^0 \to D_s^+\pi^-)}\right] \text{modulo} \left(\frac{2\pi}{\Delta m_s}\right) \quad (6.0.2)$$

Here the value of Δm_s is fixed to the HFLAV 2018 average value of $17.757\,\text{ps}^{-1}$ [159].

Before reconstructing the folded time asymmetries in Run 2 data, toy MC studies are implemented to understand the effects of the introduction of different parameters that contribute to modify these quantities: for example, the non-null mistag probability for the B_s^0 and $\bar{B}_s^0$ mesons must be taken into account, as well as the finite time resolution and vertex resolution of the LHCb detector.

In Section 6.1 the B_s^0 and $\bar{B}_s^0$ decay time distributions into $D_s^-\pi^+$ and $D_s^+\pi^-$ and the folded decay time asymmetries are studied in a MC simulation while in Section 6.2 the asymmetries obtained with the Run 2 dataset are presented.

6.1 Toy Montecarlo studies

6.1.1 The ideal case

In MC samples of $B_s^0(\bar{B}_s^0) \to D_s^\mp\pi^\pm$ with $D_s^\mp \to K^+K^-\pi^\mp$, all variables are available both at the true and at the reconstructed level; for the following studies the true variables are used, in particular the true lifetime and ID (either B_s^0 or $\bar{B}_s^0$

) and the ID of the particle that produces the K^+, *i.e.* D_s^+ or D_s^-. In fact, it is possible to separate events on the basis of the charm and beauty meson particle ID only, according to the combinations reported in Table 6.1.

Decay chain	B meson ID	D meson ID
$B_s^0 \to D_s^- \pi^+$	$+531$	-431
$\bar{B}_s^0 \to D_s^- \pi^+$	-531	-431
$B_s^0 \to D_s^+ \pi^-$	$+531$	$+431$
$\bar{B}_s^0 \to D_s^- \pi^+$	-531	$+431$

Table 6.1: Different combinations of the B meson ID and the D meson ID in $B_s^0(\bar{B}_s^0) \to D_s^\mp \pi^\pm$ decays.

In Figure 6.1 the true lifetime τ of the B_s^0, $\bar{B}_s^0$ are presented. These distributions corresponds to a total of $\approx 2.10\,\text{M}$ simulated events. The different decay channels are distinguished on the basis of the combinations reported in Table 6.1; in this way it is possible to observe the oscillation phenomenon. In Figure 6.2 the true decay time folded asymmetry is built according to Equations (6.0.1) and (6.0.2). The maximum (minimum) of these distributions is close to 1 (-1), as expected since the plots show MC simulation data at the true level. Furthermore, from these figures it is clear that the phase difference between the B_s^0 and the $\bar{B}_s^0$ decay amplitudes is equal to π: this shows in a different way that no CP violation is involved in this decay channel. Hence the values of the CP violating parameters D_f, C_f and S_f of Equation (2.1.24) for the $D_s\pi$ family of decays can be set to 1, 0 and 0 respectively, as we did in Section 5.3. This is clearly not the case for $B_s^0(\bar{B}_s^0) \to D^\mp K^\pm$, where the phase difference assumes a value different from π, as shown in Figure 6.3, meaning that CP violation occurs in this family of decays.

In Sections 6.1.2, 6.1.3 and 6.1.4 we are going to introduce some corrections in order to account for different effects: finite vertex resolution, finite time resolution and non-null mistag fraction. Finally, in Section 6.1.5 we will see the consequences of a combination of these three effects on MC data.
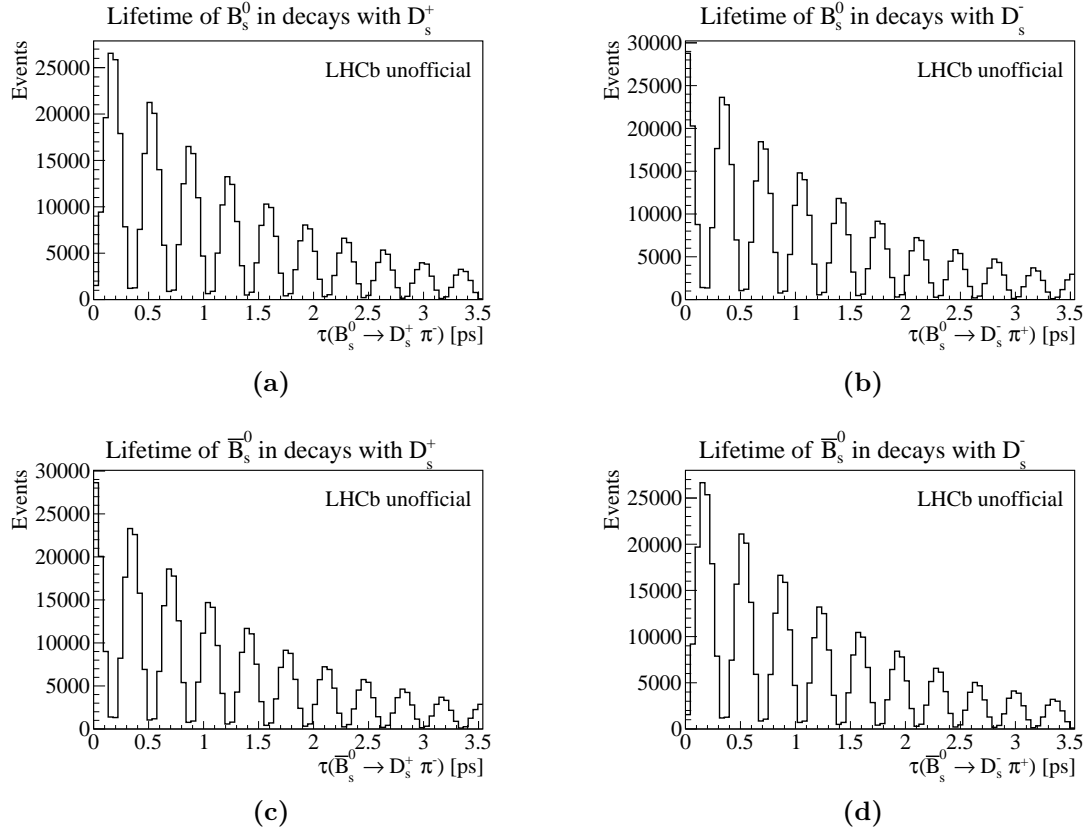
6.1.2 Effects of a finite vertex resolution
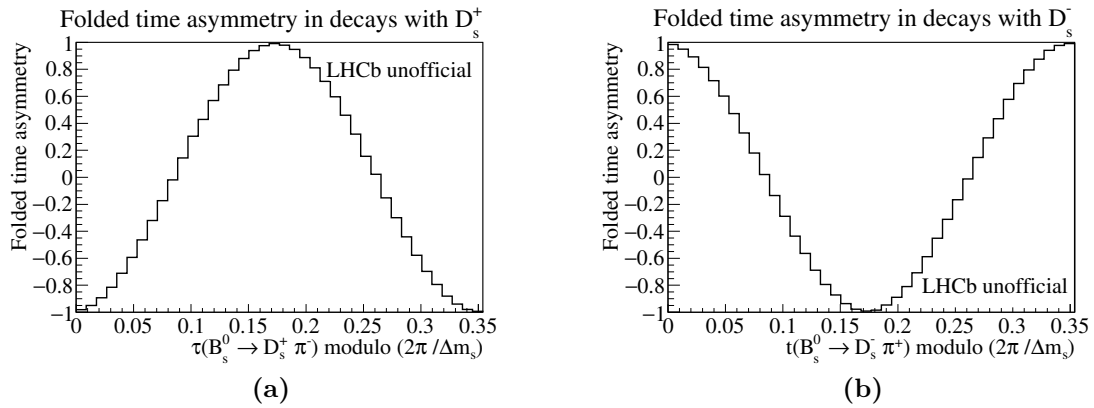
The lifetime of a particle is measured as

$$\tau = \frac{Lm}{p} \tag{6.1.1}$$

where L is the distance between the primary (production) vertex and the secondary (decay) vertex, m is the mass of the particle and p its momentum. In order to account
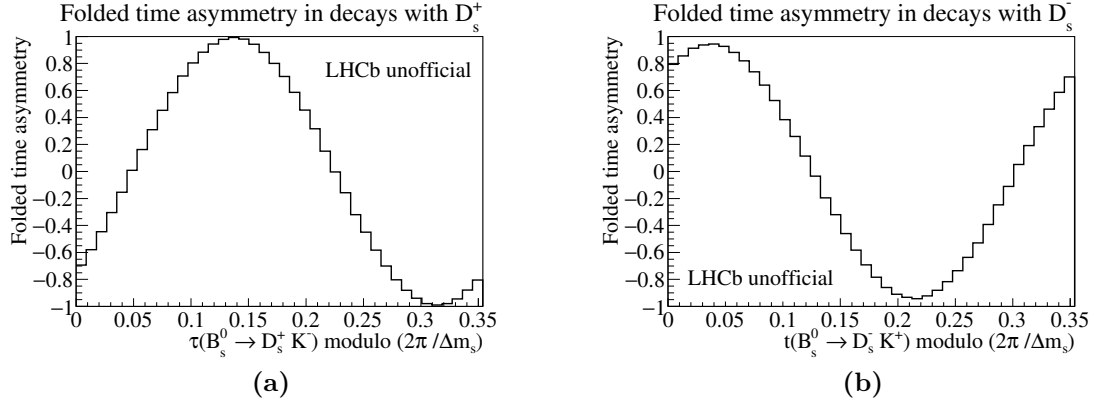
Figure 6.1: Decay time of B_s^0, $\bar{B}_s^0$ from MC simulations.

Figure 6.2: Folded time asymmetry of $B_s^0(\bar{B}_s^0) \to D_s^\mp \pi^\pm$ from MC simulations.

Figure 6.3: Folded time asymmetry of $B_s^0(\bar{B}_s^0) \to D_s^{\mp} K^{\pm}$ from MC simulations.

for the finite vertex resolution of the detector and avoid overlaps between primary and secondary vertices, the lifetime of the B meson is required to be $\tau > 0.4$ ps. In Figures 6.4 and 6.5 this lower threshold has been applied to the MC sample: in the lifetime distributions it simply introduces a cut in correspondence to $\tau = 0.4$ ps, but has no significant consequences on the folded time asymmetries, which oscillate between 1 and -1 as in the ideal case.

6.1.3 Effects of a finite time resolution

A finite decay time resolution, σ_t, must be considered too. In order to introduce this effect in the MC, the true τ undergo a smearing process according to

$$\tau = \tau_{true} + g, \qquad g \in G(0, \sigma_t) \qquad (6.1.2)$$

with g sampled from a Gaussian distribution, G, with mean set to 0 and $\sigma = \sigma_t$. The results of this process are shown in Figures 6.6 and 6.7 for different values of σ_t: 15, 30 and 45 fs. The effect of the introduction of a finite time resolution is the smearing of peaks and valleys in the decay time distributions, while the maximum (minimum) of the folded time asymmetry is lowered (raised). 45 fs is the typical LHCb time resolution.

### 6.1.4 Effects of a non-null mistag fraction

A crucial experimental aspect in the measurements of Δm_s or γ is the determination of the initial flavour of the B meson. For a tagging algorithm with discrete decisions (B_s^0, $\bar{B}_s^0$ or untagged) the fraction of mis-tagged events can be evaluated as in Equation (3.3.2). A non-null mistag probability ω is included in the MC sample by following this prescription:
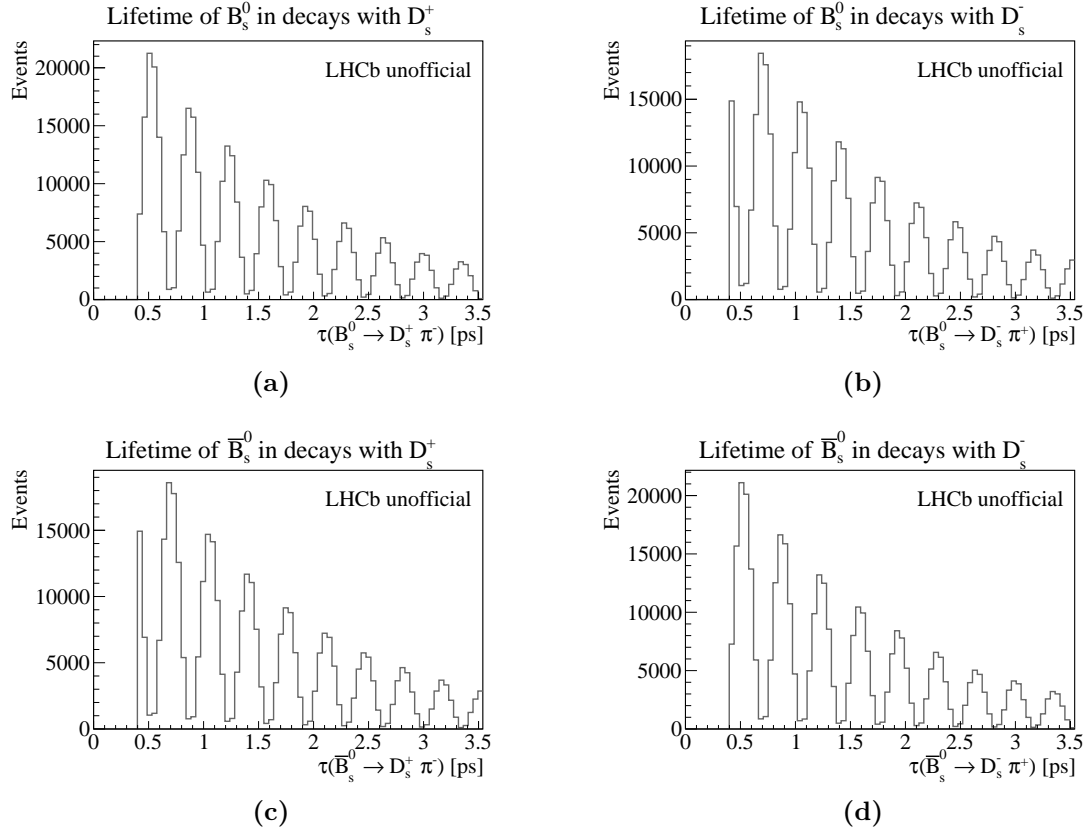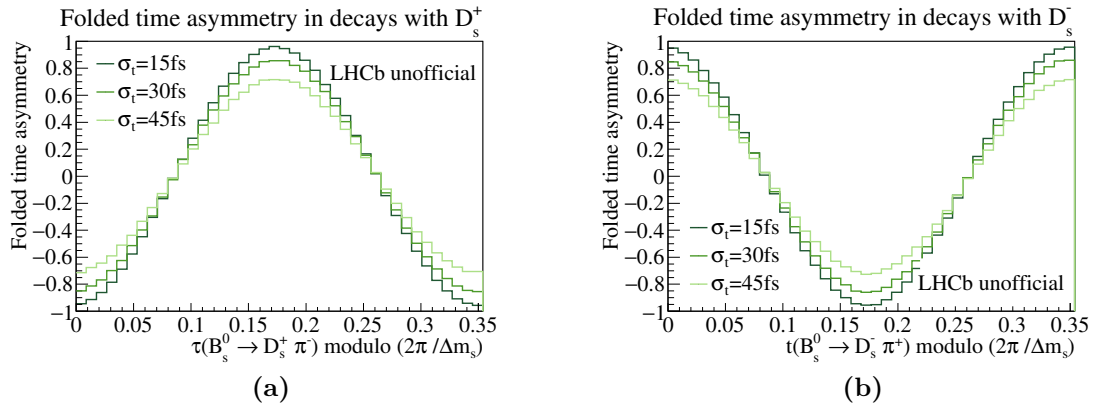
Figure 6.4: Decay time of B_s^0, $\bar{B}_s^0$ from MC simulations, after imposing a time threshold of $\tau = 0.4\,\mathrm{ps}$.
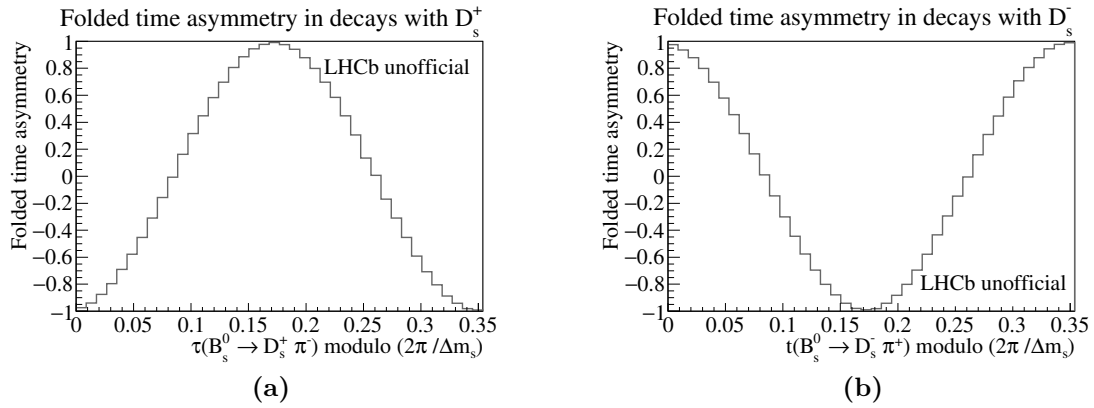
Figure 6.5: Folded time asymmetry of $B_s^0(\bar{B}_s^0) \to D_s^{\mp}\pi^{\pm}$ from MC simulations, after imposing a time threshold of $\tau = 0.4\,\mathrm{ps}$.
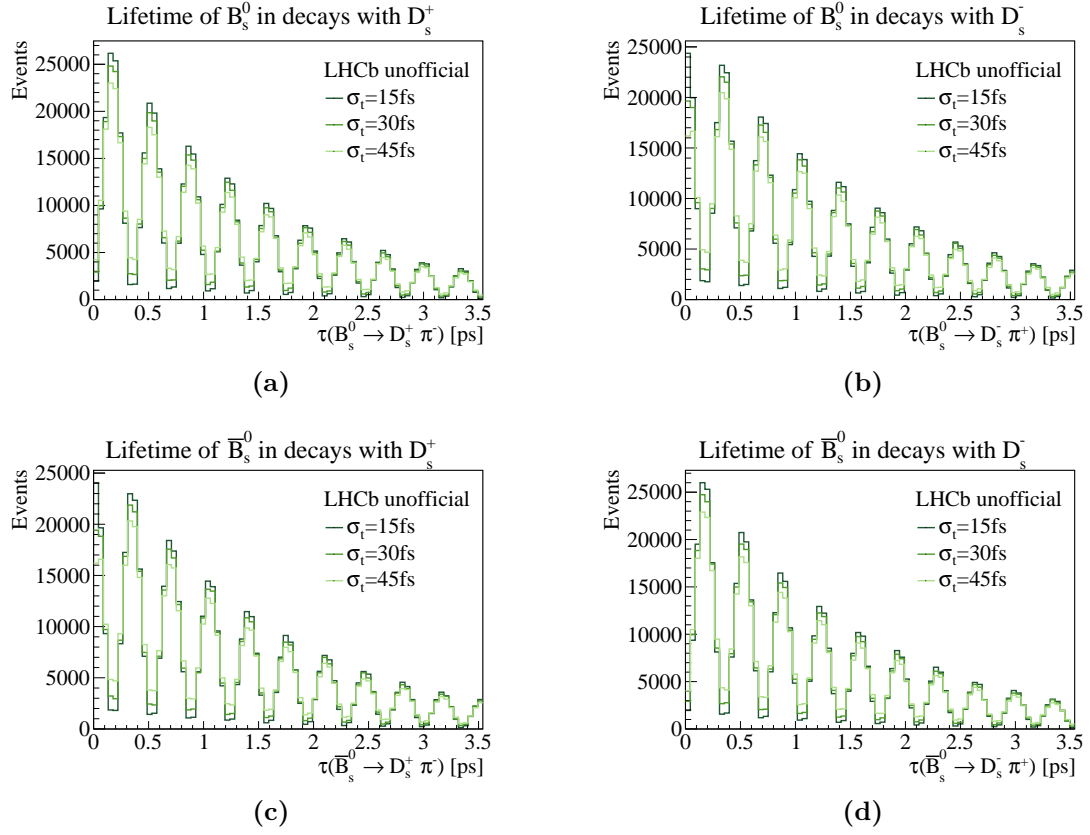
Figure 6.6: Decay time of B_s^0, $\bar{B}_s^0$ from MC simulations, for different values of the time resolution σ_t.
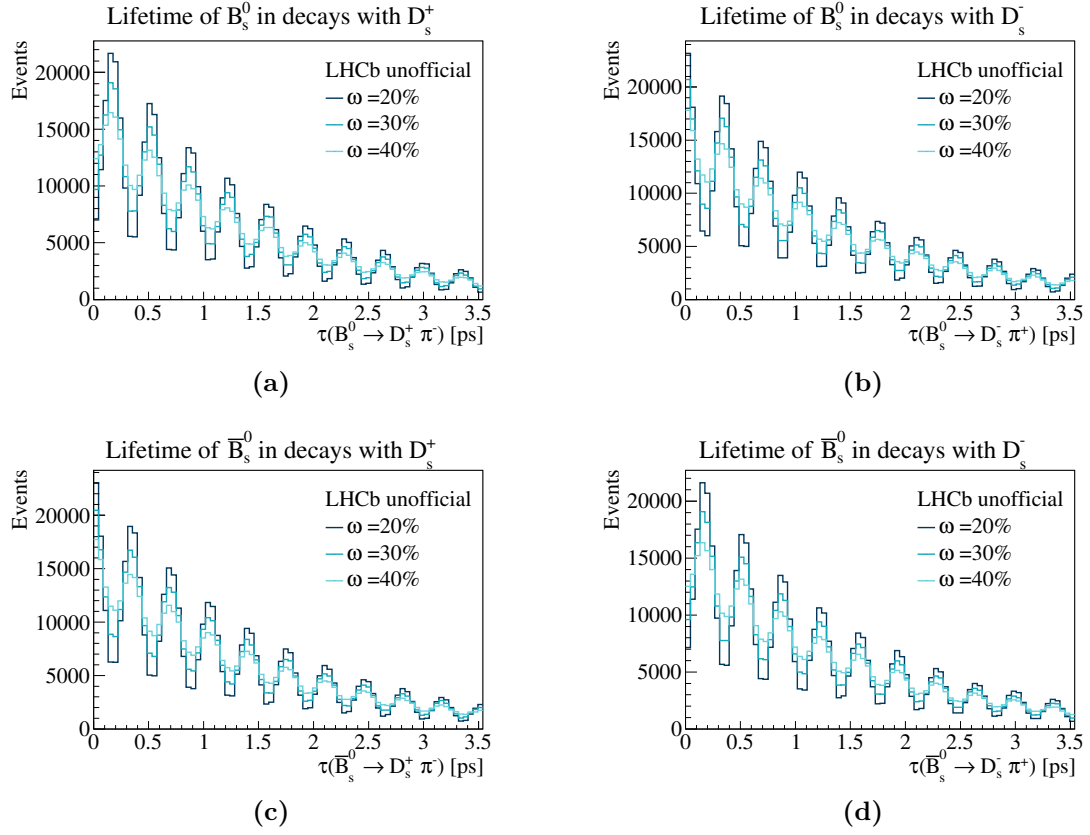

Figure 6.7: Folded time asymmetry of $B_s^0(\bar{B}_s^0) \rightarrow D_s^{\mp}\pi^{\pm}$ from MC simulations, for different values of the time resolution σ_t.

1. a number u is sampled from a uniform distribution $U(0, 1)$;

2. if $u < \omega$ then the ID of the B meson changes sign, otherwise it remains unchanged.

The effect of the introduction of a non-null mistag probability in MC is shown in Figures 6.8 and 6.9, for different values of ω: 20%, 30% and 40%. Similarly to the previous case, the higher the mistag probability is, the more peaks (valleys) of the decay time distributions are lowered (raised), as well as the maximum (minimum) of the folded time asymmetries. The typical mistag probability in LHCb is $\approx 40\%$ on average.

6.1.5   Combined effects

In order to study how the decay time distributions and the folded time asymmetries in MC get modified by the combination of finite vertex resolution, finite decay time resolution and mistag fraction, realistic values for these parameters were chosen, as similar as possible to the values from already published LHCb analyses. In particular, Figures 6.10 and 6.11 are realized with $\tau > 4\,\text{ps}$, $\sigma_t = 45\,\text{fs}$ and $\omega = 40\%$. The distributions are now significantly modified, with the folded time asymmetries oscillating between -0.2 and 0.2. By looking also at Figures 6.7 and 6.9, one can conclude that the parameter that has more impact on the shape of these distributions is the mistag probability. Thus it is crucial to develop performing flavour tagging algorithms to enhance the quality of the measurements.
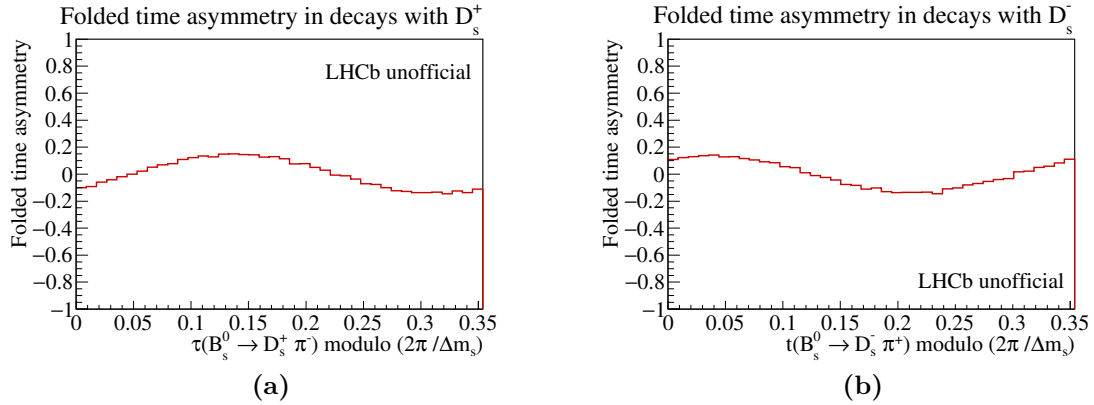
Figure 6.8: Decay time of B_s^0, $\bar{B}_s^0$ from MC simulations, for different values of the mistag probability ω.
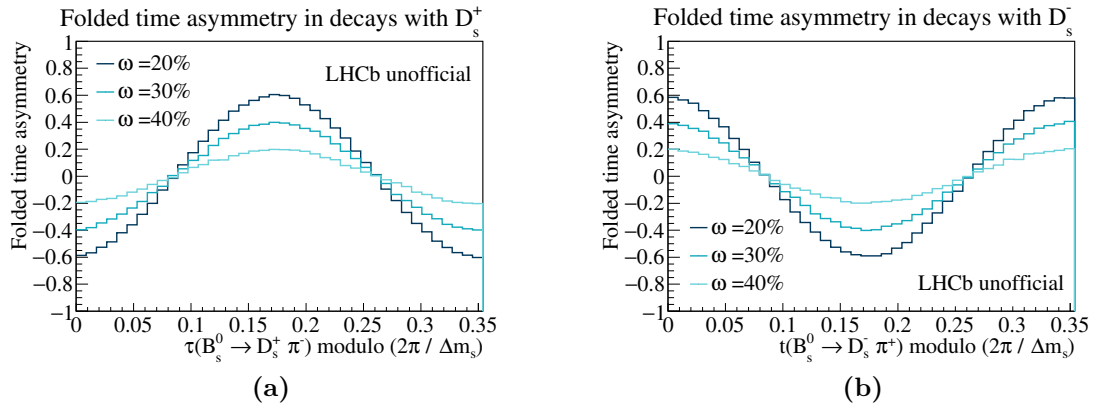
Figure 6.9: Folded time asymmetry of $B_s^0(\bar{B}_s^0) \rightarrow D_s^{\mp}\pi^{\pm}$ from MC simulations, for different values of the mistag probability ω.
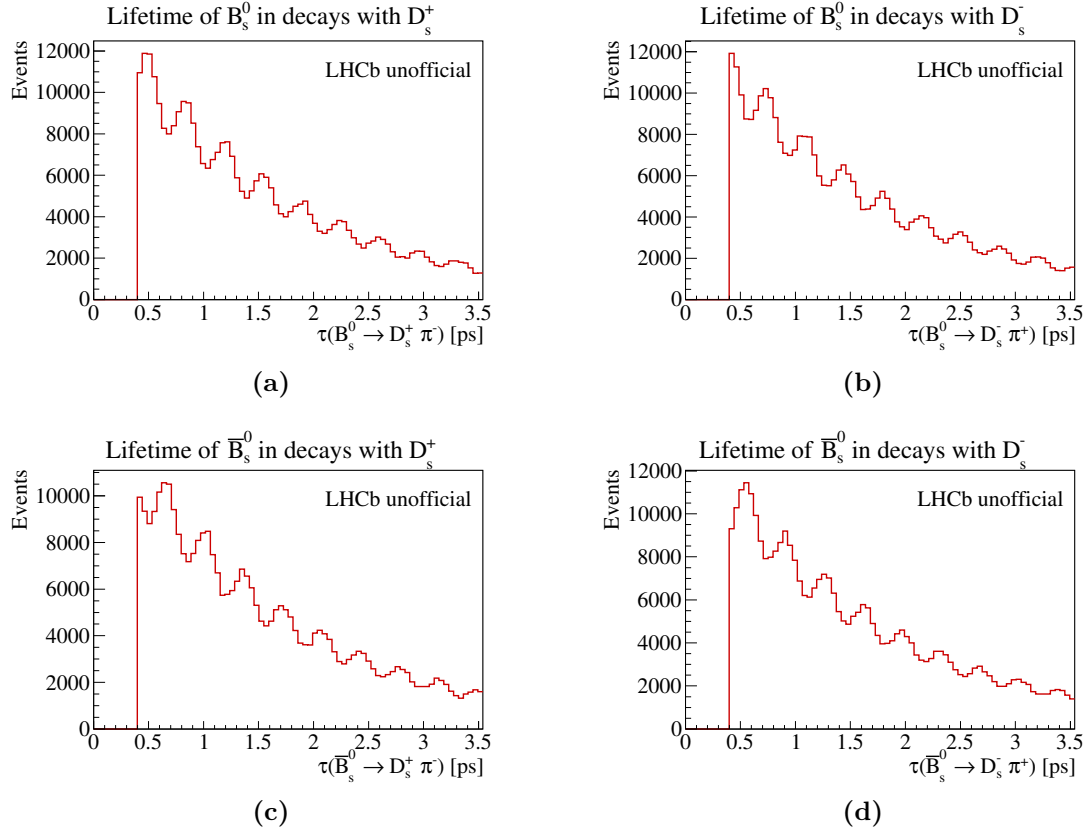
Figure 6.10: Decay time of B_s^0, $\bar{B}_s^0$ from MC simulations, with a time threshold of $\tau = 0.4\,\text{ps}$, a time resolution $\sigma_t = 45\,\text{fs}$ and a mistag probability $\omega = 40\%$.

Figure 6.11: Folded time asymmetry of $B_s^0(\bar{B}_s^0) \rightarrow D_s^\mp \pi^\pm$ from MC simulations, with a time threshold of $\tau = 0.4\,\text{ps}$, a time resolution $\sigma_t = 45\,\text{fs}$ and a mistag probability $\omega = 40\%$.

6.2 B_s^0 folded time asymmetries in Run 2 data

Folded time asymmetry plots were realised with $B_s^0 \to D_s^- \pi^+$ data from Run 2, according to Equations (6.0.1) and (6.0.1), under the assumption that all decay time efficiencies drop in the ratio. The samples are divided by year of data taking, in particular "2015+2016", "2017" and "2018". Data are background-subtracted using the *sWeight* method.

The B_s^0 and $\bar{B}_s^0$ decay chains are reconstructed on the basis of the B meson ID and the charge of the bachelor particle produced in the decay, *i.e.* the pion. The tagging of the initial flavour of the B meson is performed using both the information from OS taggers and SS taggers: each algorithm provides both a tagging decision d and an estimate of the mistag probability, η. The mistag probability is then calibrated according to Equation (3.3.4), where the parameters p_0 and p_1 are obtained from the $B_s^0 \to D_s^- \pi^-$ decay time fits for both the OS and SS taggers (see Chapter 5). Finally the decisions provided by the OS and SS taggers are combined into a final decision using the relations in Equation 3.3.8. The final decision can be $+1$ or -1: the first identify a B_s^0, the second a $\bar{B}_s^0$. All possible combinations of B meson ID and π charge are summarized in Table 6.2.

| Decay chain	B meson ID	π charge
$B_s^0 \to D_s^- \pi^+$,	$+1$	$+1$
$\bar{B}_s^0 \to D_s^- \pi^+$	-1	$+1$
$B_s^0 \to D_s^+ \pi^-$	$+1$	-1
$\bar{B}_s^0 \to D_s^- \pi^+$	-1	-1

Table 6.2: Different combinations of the B meson ID and the D meson ID in $B_s^0(\bar{B}_s^0) \to D_s^\mp \pi^\pm$ decays.

The measured folded time asymmetries are shown in Figure 6.12, 6.13 and 6.14. These distributions are phase blinded, *i.e.* each distribution is shifed by a different random phase. Note that differently from the folded time asymmetry distributions that appear in the previous Section, in these pictures the y axis range is set to $[-0.5, 0.5]$. The statistical error bars become then more visible. The distributions show a marked oscillating behaviour between a maximum of ≈ 0.2 and a minimum of ≈ -0.2.
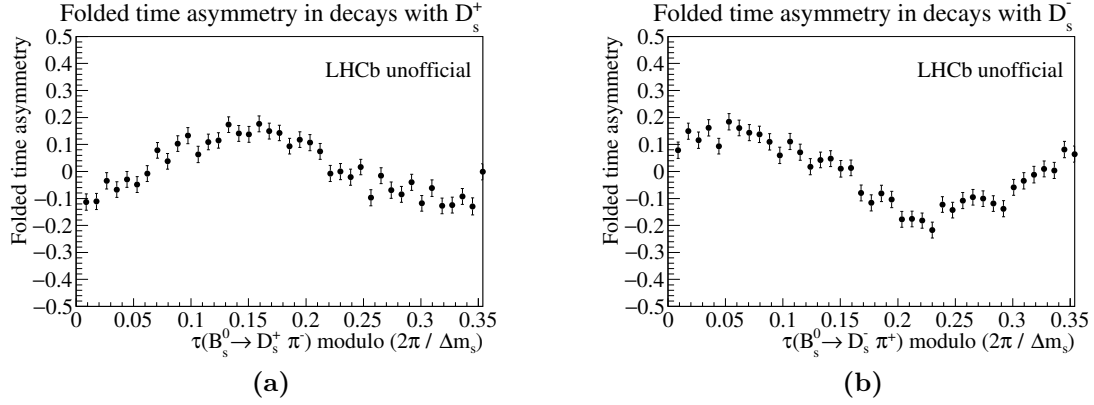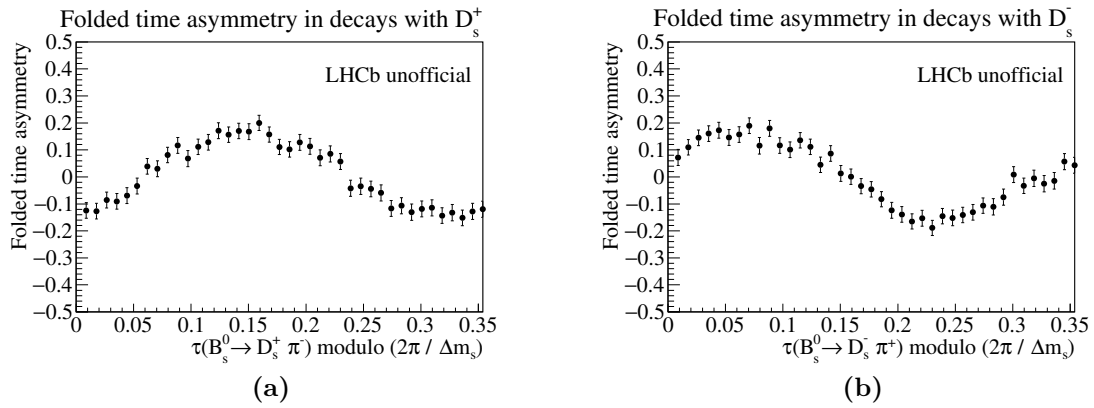
Figure 6.12: Folded time asymmetry of $B_s^0(\bar{B}_s^0) \to D_s^{\mp}\pi^{\pm}$ from 2015+2016 data.
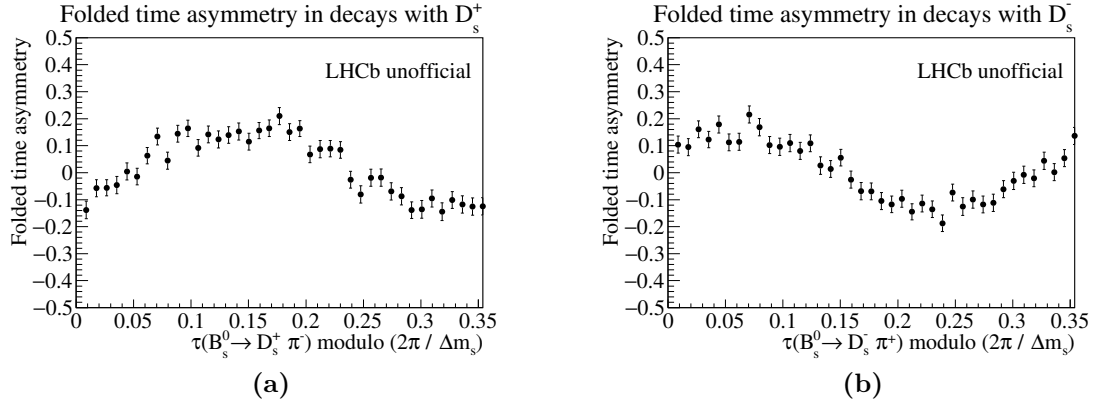
Figure 6.13: Folded time asymmetry of $B_s^0(\bar{B}_s^0) \to D_s^{\mp}\pi^{\pm}$ from 2017 data.

Figure 6.14: Folded time asymmetry of $B_s^0(\bar{B}_s^0) \to D_s^{\mp}\pi^{\pm}$ from 2018 data.

7   Conclusions

The main purpose of this thesis is the analysis of the flavour-specific decay channel $B_s^0 \to D_s^- \pi^+$ using the whole dataset collected by LHCb in Run 2. This data sample allows to perform a measurement of the $B_s^0 - \bar{B}_s^0$ oscillation frequency, Δm_s, and of the decay time efficiency. These are key quantities for the time-dependent analysis of the $B_s^0 \to D_s^\mp K^\pm$ decay channel, where a measurement of the angle γ of the CKM matrix can be obtained.

The strategy to achieve this result has been organized in different steps. Firstly, the $B_d^0 \to D^- \pi^+$ decays, that feature a very low background, are used as control channel to assess the correctness of the Montecarlo simulations: the LHCb standard fits to the invariant mass of the B_d^0 provided the *sWeights* necessary to statistically subtract background. The reconstruction of several kinematic variables has been checked by comparing data and MC simulations before and after a proper reweighting, using a standard LHCb reweighting approach.

Secondly, the standard LHCb fits to the decay time distributions of the $B_s^0 \to D_s^- \pi^+$ samples have been performed. These data have been background-subtracted through the *sWeights* provided by other analysts. From the decay time fits the parameters describing the decay time acceptance shape have been extracted. The measurement of Δm_s from these fits is still blinded: the statistical error associated to this measurement amounts to $0.0051 \, \mathrm{ps}^{-1}$, which enhance the precision with respect to the latest LHCb result [75]. Being the new statistical error comparable to the systematic error of the previous LHCb measurement, a special attention will be given to the evaluation of systematics before the result could be unblinded and published.

Finally, in order to highlight the mixing phenomenon in the $B_s^0 - \bar{B}_s^0$ system the folded time asymmetry distributions have been built. Moreover, by means of MC simulations, reconstruction effects contributing to modify the shape of these distributions have been studied.

Bibliography

[1] A. D. Sakharov. "Violation of CP invariance, C asymmetry, and baryon asymmetry of the universe". In: *Soviet Physics Uspekhi* 34.5 (May 1991), pp. 392–393. DOI: 10.1070/pu1991v034n05abeh002497. URL: https://doi.org/10.1070%2Fpu1991v034n05abeh002497.

[2] N. Cabibbo. "Unitary Symmetry and Leptonic Decays". In: *Phys. Rev. Lett.* 10 (12 June 1963), pp. 531–533. DOI: 10.1103/PhysRevLett.10.531. URL: https://link.aps.org/doi/10.1103/PhysRevLett.10.531.

[3] M. Kobayashi and T. Maskawa. "CP-Violation in the Renormalizable Theory of Weak Interaction". In: *Progress of Theoretical Physics* 49.2 (Feb. 1973), pp. 652–657. ISSN: 0033-068X. DOI: 10.1143/PTP.49.652. URL: https://doi.org/10.1143/PTP.49.652.

[4] M. B. Gavela et al. "Standard Model CP Violation and Baryon Asymmetry". In: *Modern Physics Letters A* 09.09 (1994), pp. 795–809. DOI: 10.1142/S0217732394000629. URL: https://doi.org/10.1142/S0217732394000629.

[5] L.-L. Chau and W.-Y. Keung. "Comments on the Parametrization of the Kobayashi-Maskawa Matrix". In: *Phys. Rev. Lett.* 53 (19 Nov. 1984), pp. 1802–1805. DOI: 10.1103/PhysRevLett.53.1802. URL: https://link.aps.org/doi/10.1103/PhysRevLett.53.1802.

[6] L. Wolfenstein. "Parametrization of the Kobayashi-Maskawa matrix". In: *Physical Review Letters* 51.21 (1983), p. 1945.

[7] A. J. Buras, M. E. Lautenbacher, and G. Ostermaier. "Waiting for the top quark mass, $K^+ \rightarrow \pi^+ \nu \bar{\nu}$, $B_s^0 - \bar{B}_s^0$ mixing, and CP asymmetries in B decays". In: *Physical Review D* 50.5 (1994), p. 3433.

[8] M. Gronau and D. Wyler. "On determining a weak phase from charged B decay asymmetries". In: *Physics Letters B* 265.1 (1991), pp. 172–176. ISSN: 0370-2693. DOI: https://doi.org/10.1016/0370-2693(91)90034-N. URL: http://www.sciencedirect.com/science/article/pii/037026939190034N.

[9] M. Gronau and D. London. "How to determine all the angles of the unitarity triangle from $B_d^0 \to DK_s$ and $B_s^0 \to D\phi$". In: *Physics Letters B* 253.3 (1991), pp. 483–488. ISSN: 0370-2693. DOI: https://doi.org/10.1016/0370-2693(91)91756-L. URL: http://www.sciencedirect.com/science/article/pii/037026939191756L.

[10] D. Atwood, I. Dunietz, and A. Soni. "Enhanced CP Violation with $B \to KD^0(\bar{D}^0)$ Modes and Extraction of the Cabibbo-Kobayashi-Maskawa Angle γ". In: *Phys. Rev. Lett.* 78 (17 Apr. 1997), pp. 3257–3260. DOI: 10.1103/PhysRevLett.78.3257. URL: https://link.aps.org/doi/10.1103/PhysRevLett.78.3257.

[11] D. Atwood, I. Dunietz, and A. Soni. "Improved methods for observing CP violation in $B^\pm \to KD$ and measuring the CKM phase γ". In: *Phys. Rev. D* 63 (3 Jan. 2001), p. 036005. DOI: 10.1103/PhysRevD.63.036005. URL: https://link.aps.org/doi/10.1103/PhysRevD.63.036005.

[12] C. Jarlskog. "Commutator of the Quark Mass Matrices in the Standard Electroweak Model and a Measure of Maximal CP Nonconservation". In: *Phys. Rev. Lett.* 55 (10 Sept. 1985), pp. 1039–1042. DOI: 10.1103/PhysRevLett.55.1039. URL: https://link.aps.org/doi/10.1103/PhysRevLett.55.1039.

[13] R. Huerta and R. Pérez-Marcial. "Comment on *Commutator of the Quark Mass Matrices in the Standard Electroweak Model and a Measure of Maximal CP Nonconservation*". In: *Phys. Rev. Lett.* 58 (16 Apr. 1987), pp. 1698–1698. DOI: 10.1103/PhysRevLett.58.1698. URL: https://link.aps.org/doi/10.1103/PhysRevLett.58.1698.

[14] C. Jarlskog. "Jarlskog Responds". In: *Phys. Rev. Lett.* 57 (22 Dec. 1986), pp. 2875–2875. DOI: 10.1103/PhysRevLett.57.2875. URL: https://link.aps.org/doi/10.1103/PhysRevLett.57.2875.

[15] T. D. Lee and C. S. Wu. "Weak Interactions: Decays of neutral K mesons". In: *Ann. Rev. Nucl. Part. Sci.* 16 (1966), pp. 511–590. DOI: 10.1146/annurev.ns.16.120166.002455.

[16] G. C. Branco, L. Lavoura, and J. P. Silva. "CP Violation". In: *Int. Ser. Monogr. Phys.* 103 (1999), pp. 1–536.

[17] I.I. Bigi et al. *CP Violation.* Cambridge Monographs on Particle Physics, Nuclear Physics and Cosmology. Cambridge University Press, 2000. ISBN: 9780521443494. URL: https://books.google.it/books?id=ZUANziLsV-MC.

[18]   P. Kooijman and N. Tuning. *Lectures on CP violation.* URL: https://www.nikhef.nl/~h71/Lectures/2015/ppII-cpviolation-29012015.pdf (visited on 10/14/2019). Jan. 2015.

[19]   S. L. Glashow. "Partial-symmetries of weak interactions". In: *Nuclear Physics* 22.4 (1961), pp. 579–588. ISSN: 0029-5582. DOI: https://doi.org/10.1016/0029-5582(61)90469-2. URL: http://www.sciencedirect.com/science/article/pii/0029558261904692.

[20]   S. Weinberg. "A Model of Leptons". In: *Phys. Rev. Lett.* 19 (21 Nov. 1967), pp. 1264–1266. DOI: 10.1103/PhysRevLett.19.1264. URL: https://link.aps.org/doi/10.1103/PhysRevLett.19.1264.

[21]   A. Salam. *Elementary Particle Physics: Relativistic Groups and Analyticity.* Ed. by N. Svartholm. Stockholm: Almquvist and Wiksell, 1968, p. 367.

[22]   S. L. Glashow, J. Iliopoulos, and L. Maiani. "Weak Interactions with Lepton-Hadron Symmetry". In: *Phys. Rev. D* 2 (7 Oct. 1970), pp. 1285–1292. DOI: 10.1103/PhysRevD.2.1285. URL: https://link.aps.org/doi/10.1103/PhysRevD.2.1285.

[23]   T. Inami and C. S. Lim. "Effects of Superheavy Quarks and Leptons in Low-Energy Weak Processes $K_L \to \mu\bar{\mu}$, $K^+ \to \pi^+\nu\bar{\nu}$ and $K^0 \leftrightarrow \bar{K}^0$". In: *Progress of Theoretical Physics* 65.1 (Jan. 1981), pp. 297–314. ISSN: 0033-068X. DOI: 10.1143/PTP.65.297. URL: https://doi.org/10.1143/PTP.65.297.

[24]   A. J. Buras and M. Lindner. *Heavy Flavours II.* Vol. 15. World Scientific, 1998.

[25]   A. J. Buras, M. Jamin, and P. H. Weisz. "Leading and next-to-leading QCD corrections to ϵ parameter and B^0 mixing in the presence of a heavy top quark". In: *Nuclear Physics B* 347.3 (1990), pp. 491–536.

[26]   C. Jarlskog. *CP violation.* Vol. 3. World Scientific, 1989.

[27]   M. Tanabashi et al. "Review of Particle Physics". In: *Phys. Rev. D* 98 (3 Aug. 2018), p. 030001. DOI: 10.1103/PhysRevD.98.030001. URL: https://link.aps.org/doi/10.1103/PhysRevD.98.030001.

[28]   A. B. Carter and A. I. Sanda. "CP Nonconservation in Cascade Decays of B Mesons". In: *Phys. Rev. Lett.* 45 (12 Sept. 1980), pp. 952–954. DOI: 10.1103/PhysRevLett.45.952. URL: https://link.aps.org/doi/10.1103/PhysRevLett.45.952.

[29]   A. B. Carter and A. I. Sanda. "CP violation in B-meson decays". In: *Phys. Rev. D* 23 (7 Apr. 1981), pp. 1567–1579. DOI: 10.1103/PhysRevD.23.1567. URL: https://link.aps.org/doi/10.1103/PhysRevD.23.1567.

[30] I. I. Bigi and A. I. Sanda. "CP violation in heavy flavor decays: Predictions and search strategies". In: *Nuclear Physics B* 281.1 (1987), pp. 41–71. ISSN: 0550-3213. DOI: https://doi.org/10.1016/0550-3213(87)90246-X. URL: http://www.sciencedirect.com/science/article/pii/055032138790246X.

[31] I. Dunietz and J. L. Rosner. "Time-dependent CP-violation effects in $B^0 - \bar{B}^0$ systems". In: *Phys. Rev. D* 34 (5 Sept. 1986), pp. 1404–1417. DOI: 10.1103/PhysRevD.34.1404. URL: https://link.aps.org/doi/10.1103/PhysRevD.34.1404.

[32] T. Jubb et al. "On the ultimate precision of meson mixing observables". In: *Nuclear Physics B* 915 (2017), pp. 431–453.

[33] M. Artuso, G. Borissov, and A. Lenz. "CP violation in the B_s^0 system". In: *Reviews of Modern Physics* 88.4 (2016), p. 045002.

[34] A. J. Bevan et al. "The Physics of the B Factories". In: *The European Physical Journal C* 74.11 (Nov. 2014), p. 3026. ISSN: 1434-6052. DOI: 10.1140/epjc/s10052-014-3026-9. URL: https://doi.org/10.1140/epjc/s10052-014-3026-9.

[35] *CKMFitter*. URL: http://ckmfitter.in2p3.fr/ (visited on 10/14/2019).

[36] The CKMFitter Group. *Updated results on the CKM matrix.* The 39th International Conference on High Energy Physics (ICHEP2018). Also available at URL: http://ckmfitter.in2p3.fr/www/results/plots_summer18/num/ckmEval_results_summer18.pdf (visited on 10/14/2019). Seoul, Aug. 2018.

[37] J. Charles et al. "CP violation and the CKM matrix: assessing the impact of the asymmetric B factories". In: *The European Physical Journal C* 41.1 (May 2005), pp. 1–131. ISSN: 1434-6052. DOI: 10.1140/epjc/s2005-02169-1. URL: http://dx.doi.org/10.1140/epjc/s2005-02169-1.

[38] J. Brod et al. "New physics effects in tree-level decays and the precision in the determination of the quark mixing angle γ". In: *Phys. Rev. D* 92 (3 Aug. 2015), p. 033002. DOI: 10.1103/PhysRevD.92.033002. URL: https://link.aps.org/doi/10.1103/PhysRevD.92.033002.

[39] J. Brod and J. Zupan. "The ultimate theoretical error on γ from $B \to DK$ decays". In: *Journal of High Energy Physics* 2014.1 (Jan. 2014), p. 51. ISSN: 1029-8479. DOI: 10.1007/JHEP01(2014)051. URL: https://doi.org/10.1007/JHEP01(2014)051.

[40] *Update of the LHCb combination of the CKM angle γ*. Tech. rep. LHCb-CONF-2018-002. CERN-LHCb-CONF-2018-002. Geneva: CERN, May 2018. URL: https://cds.cern.ch/record/2319289.

[41] R. Aaij et al. "Measurement of the CKM angle γ from a combination of LHCb results". In: *Journal of High Energy Physics* 2016.12 (Dec. 2016), p. 87. ISSN: 1029-8479. DOI: 10.1007/JHEP12(2016)087. URL: https://doi.org/10.1007/JHEP12(2016)087.

[42] R. Aaij et al. "Measurement of the CKM angle γ from a combination of $B^{\pm} \to Dh^{\pm}$ analyses". In: *Physics Letters B* 726.1 (2013), pp. 151–163. ISSN: 0370-2693. DOI: https://doi.org/10.1016/j.physletb.2013.08.020. URL: http://www.sciencedirect.com/science/article/pii/S0370269313006461.

[43] *Update of the LHCb combination of the CKM angle γ using $B \to DK$ decays.* Tech. rep. LHCb-CONF-2017-004. CERN-LHCb-CONF-2017-004. Geneva: CERN, July 2017. URL: https://cds.cern.ch/record/2275866.

[44] I. Bediaga et al. *Physics case for an LHCb Upgrade II - Opportunities in flavour physics, and beyond, in the HL-LHC era.* 2018. arXiv: 1808.08865 [hep-ex].

[45] I. Bediaga et al. *Framework TDR for the LHCb Upgrade: Technical Design Report.* Tech. rep. CERN-LHCC-2012-007. LHCb-TDR-12. Apr. 2012. URL: https://cds.cern.ch/record/1443882.

[46] R. Aaij et al. *Expression of Interest for a Phase-II LHCb Upgrade: Opportunities in flavour physics, and beyond, in the HL-LHC era.* Tech. rep. CERN-LHCC-2017-003. Geneva: CERN, Feb. 2017. URL: http://cds.cern.ch/record/2244311.

[47] R. Aaij et al. "Measurement of CP observables in $B^{\pm} \to D^{(*)}K^{\pm}$ and $B^{\pm} \to D^{(*)}\pi^{\pm}$ decays". In: *Physics Letters B* 777 (Feb. 2018), pp. 16–30. ISSN: 0370-2693. DOI: 10.1016/j.physletb.2017.11.070. URL: http://dx.doi.org/10.1016/j.physletb.2017.11.070.

[48] R. Aaij et al. "Measurement of CP observables in $B^{\pm} \to DK^{\pm}$ and $B^{\pm} \to D\pi^{\pm}$ with two- and four-body D decays". In: *Physics Letters B* 760 (2016), pp. 117–131. ISSN: 0370-2693. DOI: https://doi.org/10.1016/j.physletb.2016.06.022. URL: http://www.sciencedirect.com/science/article/pii/S0370269316302751.

[49] R. Aaij et al. "Study of CP violation in $B^{\mp} \to Dh^{\mp}$ ($h = K, \pi$) with the modes $D \to K^{\mp}\pi^{\pm}\pi^0$, $D \to \pi^+\pi^-\pi^0$ and $D \to K^+K^-\pi^0$". In: *Phys. Rev. D* 91 (11 June 2015), p. 112014. DOI: 10.1103/PhysRevD.91.112014. URL: https://link.aps.org/doi/10.1103/PhysRevD.91.112014.

[50]   R. Aaij et al. "Measurement of the CKM angle γ using $B^{\pm} \to DK^{\pm}$ with $D \to$ $K_S^0 \pi^+ \pi^-$, $K_S^0 K^+ K^-$ decays". In: *Journal of High Energy Physics* 2014.10 (Oct. 2014), p. 97. ISSN: 1029-8479. DOI: 10.1007/JHEP10(2014)097. URL: https://doi.org/10.1007/JHEP10(2014)097.

[51]   R. Aaij et al. "Measurement of the CKM angle γ using $B^{\pm} \to DK^{\pm}$ with $D \to K_S^0 \pi^+ \pi^-$, $K_S^0 K^+ K^-$ decays". In: *Journal of High Energy Physics* 2018.8 (Aug. 2018). ISSN: 1029-8479. DOI: 10.1007/jhep08(2018)176. URL: http://dx.doi.org/10.1007/JHEP08(2018)176.

[52]   R. Aaij et al. "A study of CP violation in $B^{\pm} \to DK^{\pm}$ and $B^{\pm} \to D\pi^{\pm}$ decays with $D \to K_s^0 K^{\pm} \pi^{\mp}$ final states". In: *Physics Letters B* 733 (2014), pp. 36–45. ISSN: 0370-2693. DOI: https://doi.org/10.1016/j.physletb.2014.03.051. URL: http://www.sciencedirect.com/science/article/pii/S037026931400207X.

[53]   R. Aaij et al. "Measurement of CP observables in $B^{\pm} \to DK^{*\pm}$ decays using two- and four-body D final states". In: *Journal of High Energy Physics* 2017.11 (Nov. 2017), p. 156. ISSN: 1029-8479. DOI: 10.1007/JHEP11(2017)156. URL: https://doi.org/10.1007/JHEP11(2017)156.

[54]   R. Aaij et al. "Study of $B^- \to DK^- \pi^+ \pi^-$ and $B^- \to D\pi^- \pi^+ \pi^-$ decays and determination of the CKM angle γ". In: *Phys. Rev. D* 92 (11 Dec. 2015), p. 112005. DOI: 10.1103/PhysRevD.92.112005. URL: https://link.aps.org/doi/10.1103/PhysRevD.92.112005.

[55]   R. Aaij et al. "Measurement of CP violation parameters in $B^0 \to DK^{*0}$ decays". In: *Phys. Rev. D* 90 (11 Dec. 2014), p. 112002. DOI: 10.1103/PhysRevD.90.112002. URL: https://link.aps.org/doi/10.1103/PhysRevD.90.112002.

[56]   R. Aaij et al. "Constraints on the unitarity triangle angle γ from Dalitz plot analysis of $B^0 \to DK^+ \pi^-$ decays". In: *Phys. Rev. D* 93 (11 June 2016), p. 112018. DOI: 10.1103/PhysRevD.93.112018. URL: https://link.aps.org/doi/10.1103/PhysRevD.93.112018.

[57]   R. Aaij et al. "Measurement of the CKM angle γ using $B^0 \to DK^{*0}$ with $D \to K_s^0 \pi^+ \pi^-$ decays". In: *Journal of High Energy Physics* 2016.8 (Aug. 2016), p. 137. ISSN: 1029-8479. DOI: 10.1007/JHEP08(2016)137. URL: https://doi.org/10.1007/JHEP08(2016)137.

[58]   R. Aaij et al. "Measurement of CP asymmetry in $B_s^0 \to D_s^{\mp} K^{\pm}$ decays". In: *Journal of High Energy Physics* 2018.3 (Mar. 2018), p. 59. ISSN: 1029-8479. DOI: 10.1007/JHEP03(2018)059. URL: https://doi.org/10.1007/JHEP03(2018)059.

[59]   R. Aaij et al. "Measurement of CP violation in $B^0 \to D^{\mp}\pi^{\pm}$ decays". In: *Journal of High Energy Physics* 2018.6 (June 2018), p. 84. ISSN: 1029-8479. DOI: 10.1007/JHEP06(2018)084. URL: https://doi.org/10.1007/JHEP06(2018)084.

[60]   A. Giri et al. "Determining γ using $B^{\pm} \to \mathrm{D}K^{\pm}$ with multibody D decays". In: *Phys. Rev. D* 68 (5 Sept. 2003), p. 054018. DOI: 10.1103/PhysRevD.68.054018. URL: https://link.aps.org/doi/10.1103/PhysRevD.68.054018.

[61]   Y. Grossman, Z. Ligeti, and A. Soffer. "Measuring γ in $B^{\pm} \to K^{\pm}(KK^*)_D$ decays". In: *Phys. Rev. D* 67 (7 Apr. 2003), p. 071301. DOI: 10.1103/PhysRevD.67.071301. URL: https://link.aps.org/doi/10.1103/PhysRevD.67.071301.

[62]   R. Aleksan, I. Dunietz, and B. Kayser. "Determining the CP-violating phase γ". In: *Zeitschrift für Physik C Particles and Fields* 54.4 (Dec. 1992), pp. 653–659. ISSN: 1431-5858. DOI: 10.1007/BF01559494. URL: https://doi.org/10.1007/BF01559494.

[63]   C. Albajar et al. "Search for $B^0 - \bar{B}^0$ oscillations at the CERN proton-antiproton collider". In: *Physics Letters B* 186.2 (1987), pp. 247–254. ISSN: 0370-2693. DOI: https://doi.org/10.1016/0370-2693(87)90288-7. URL: http://www.sciencedirect.com/science/article/pii/0370269387902887.

[64]   H. Albrecht et al. "Observation of B^0 - anti-B^0 Mixing". In: *Physics Letters B* 192.1 (1987), pp. 245–252. ISSN: 0370-2693. DOI: https://doi.org/10.1016/0370-2693(87)91177-4. URL: http://www.sciencedirect.com/science/article/pii/0370269387911774.

[65]   *Deutsches Elektronen-Synchrotron - A Research Centre of the Helmholtz Association*. URL: http://www.desy.de/index_eng.html (visited on 03/11/2019).

[66]   H. Albrecht et al. "Argus: A universal detector at DORIS II". In: *Nuclear Instruments and Methods in Physics Research Section A: Accelerators, Spectrometers, Detectors and Associated Equipment* 275.1 (1989), pp. 1–48. ISSN: 0168-9002. DOI: https://doi.org/10.1016/0168-9002(89)90334-3. URL: http://www.sciencedirect.com/science/article/pii/0168900289903343.

[67]   *LEP design report*. Tech. rep. CERN-LEP-84-01. Copies shelved as reports in LEP, PS and SPS libraries. Geneva: CERN, June 1984. URL: https://cds.cern.ch/record/102083.

[68]   *SLAC Linear Collider Conceptual Design Report*. Tech. rep. Stanford University, June 1980. URL: https://www-public.slac.stanford.edu/sciDoc/docMeta.aspx?slacPubNumber=slac-r-229.

[69]   *Design Report Tevatron 1 project*. Tech. rep. FERMILAB-DESIGN-1984-01. 1984. URL: https://cds.cern.ch/record/1478620.

[70] A. Abulencia et al. "Measurement of the $B_s^0 - \bar{B}_s^0$ Oscillation Frequency". In: *Physical Review Letters* 97.6 (Aug. 2006). ISSN: 1079-7114. DOI: 10.1103/physrevlett.97.062003. URL: http://dx.doi.org/10.1103/PhysRevLett.97.062003.

[71] C. Gay. "B Mixing". In: *Annual Review of Nuclear and Particle Science* 50.1 (Dec. 2000), pp. 577–641. ISSN: 1545-4134. DOI: 10.1146/annurev.nucl.50.1.577. URL: http://dx.doi.org/10.1146/annurev.nucl.50.1.577.

[72] A. Abulencia et al. "Observation of $B_s^0 - \overline{B}_s^0$ Oscillations". In: *Phys. Rev. Lett.* 97 (24 Dec. 2006), p. 242003. DOI: 10.1103/PhysRevLett.97.242003. URL: https://link.aps.org/doi/10.1103/PhysRevLett.97.242003.

[73] L. Evans and P. Bryant. "LHC machine". In: *Journal of instrumentation* 3.08 (2008), S08001.

[74] R. Aaij et al. "Measurement of CP violation and the B_s^0 meson decay width difference with $B_s^0 \to J\psi K^+ K^-$ and $B_s^0 \to J\psi \pi^+ \pi^-$ decays". In: *Physical Review D* 87.11 (June 2013). ISSN: 1550-2368. DOI: 10.1103/physrevd.87.112010. URL: http://dx.doi.org/10.1103/PhysRevD.87.112010.

[75] R. Aaij et al. "Precision measurement of the $B_s^0 - \bar{B}_s^0$ oscillation frequency with the decay $B_s^0 \to D_s^- \pi^+$". In: *New Journal of Physics* 15.5 (May 2013), p. 053021. DOI: 10.1088/1367-2630/15/5/053021. URL: https://doi.org/10.1088%2F1367-2630%2F15%2F5%2F053021.

[76] Y. Ohnishi et al. "Accelerator design at SuperKEKB". In: *Progress of Theoretical and Experimental Physics* 2013.3 (Mar. 2013). 03A011. ISSN: 2050-3911. DOI: 10.1093/ptep/pts083. URL: https://doi.org/10.1093/ptep/pts083.

[77] W. M. Yao et al. "Review of particle physics". English. In: *Journal of Physics G: Nuclear and Particle Physics* 33.1 (July 2006). ISSN: 0954-3899. DOI: 10.1088/0954-3899/33/1/001.

[78] A. Bharucha et al. "Implications of LHCb measurements and future prospects". In: *The European Physical Journal C* 73.4 (Apr. 2013), p. 2373. ISSN: 1434-6052. DOI: 10.1140/epjc/s10052-013-2373-2. URL: https://doi.org/10.1140/epjc/s10052-013-2373-2.

[79] R. Aaij et al. "Angular analysis and differential branching fraction of the decay $B_s^0 \to \phi\mu^+\mu^-$". In: *Journal of High Energy Physics* 2015.9 (Sept. 2015). ISSN: 1029-8479. DOI: 10.1007/jhep09(2015)179. URL: http://dx.doi.org/10.1007/JHEP09(2015)179.

[80] R. Aaij et al. "Angular analysis of the $B^0 \to K^{*0}\mu^+\mu^-$ decay using $3\,\mathrm{fb}^{-1}$ of integrated luminosity". In: *Journal of High Energy Physics* 2016.2 (Feb. 2016), p. 104. ISSN: 1029-8479. DOI: 10.1007/JHEP02(2016)104. URL: https://doi.org/10.1007/JHEP02(2016)104.

[81] R. Aaij et al. "Test of Lepton Universality Using $B^+ \to K^+\ell^+\ell^-$ Decays". In: *Physical Review Letters* 113.15 (Oct. 2014). ISSN: 1079-7114. DOI: 10.1103/physrevlett.113.151601. URL: http://dx.doi.org/10.1103/PhysRevLett.113.151601.

[82] R. Aaij et al. "Test of lepton universality with $B^0 \to K^{*0}\ell^+\ell^-$ decays". In: *Journal of High Energy Physics* 2017.8 (Aug. 2017). ISSN: 1029-8479. DOI: 10.1007/jhep08(2017)055. URL: http://dx.doi.org/10.1007/JHEP08(2017)055.

[83] T. Hurth, F. Mahmoudi, and S. Neshatpour. "On the anomalies in the latest LHCb data". In: *Nuclear Physics B* 909 (Aug. 2016), pp. 737–777. ISSN: 0550-3213. DOI: 10.1016/j.nuclphysb.2016.05.022. URL: http://dx.doi.org/10.1016/j.nuclphysb.2016.05.022.

[84] A. K. Alok et al. "New physics in $b \to s\mu^+\mu^-$ after the measurement of R_{K^*}". In: *Physical Review D* 96.9 (Nov. 2017). ISSN: 2470-0029. DOI: 10.1103/physrevd.96.095009. URL: http://dx.doi.org/10.1103/PhysRevD.96.095009.

[85] W. Altmannshofer, P. Stangl, and D. M. Straub. "Interpreting hints for lepton flavor universality violation". In: *Physical Review D* 96.5 (Sept. 2017). ISSN: 2470-0029. DOI: 10.1103/physrevd.96.055008. URL: http://dx.doi.org/10.1103/PhysRevD.96.055008.

[86] L. S. Geng et al. "Towards the discovery of new physics with lepton-universality ratios of $b \to s\ell\ell$ decays". In: *Physical Review D* 96.9 (Nov. 2017). ISSN: 2470-0029. DOI: 10.1103/physrevd.96.093006. URL: http://dx.doi.org/10.1103/PhysRevD.96.093006.

[87] R. Alonso et al. "Flavoured B - L local symmetry and anomalous rare B decays". In: *Physics Letters B* 774 (Nov. 2017), pp. 643–648. ISSN: 0370-2693. DOI: 10.1016/j.physletb.2017.10.027. URL: http://dx.doi.org/10.1016/j.physletb.2017.10.027.

[88] B. Capdevila et al. "Patterns of New Physics in $b \to s\ell^+\ell^-$ transitions in the light of recent data". In: *Journal of High Energy Physics* 2018.1 (Jan. 2018). ISSN: 1029-8479. DOI: 10.1007/jhep01(2018)093. URL: http://dx.doi.org/10.1007/JHEP01(2018)093.

[89] A. Carmona and F. Goertz. "Recent B physics anomalies: a first hint for compositeness?" In: *The European Physical Journal C* 78.11 (Nov. 2018). ISSN: 1434-6052. DOI: 10.1140/epjc/s10052-018-6437-1. URL: http://dx.doi.org/10.1140/epjc/s10052-018-6437-1.

[90] G. D'Amico et al. "Flavour anomalies after the R_{K^*} measurement". In: *Journal of High Energy Physics* 2017.9 (Sept. 2017). Last revised on Mar. 2019. ISSN: 1029-8479. DOI: 10.1007/jhep09(2017)010. arXiv: 1704.05438 [hep-ph]. URL: http://dx.doi.org/10.1007/JHEP09(2017)010.

[91] A. Lenz and U. Nierste. "Numerical updates of lifetimes and mixing parameters of B mesons". In: (2011). arXiv: 1102.4274 [hep-ph].

[92] M. Artuso, G. Borissov, and A. Lenz. "CP violation in the B_s^0 system". In: *Rev. Mod. Phys.* 88 (4 Oct. 2016), p. 045002. DOI: 10.1103/RevModPhys.88.045002. URL: https://link.aps.org/doi/10.1103/RevModPhys.88.045002.

[93] S. Aoki et al. "FLAG Review 2019". In: (2019). arXiv: 1902.08191 [hep-lat].

[94] A. Bazavov et al. "$B_{(s)}^0$-mixing matrix elements from lattice QCD for the Standard Model and beyond". In: *Physical Review D* 93.11 (June 2016). ISSN: 2470-0029. DOI: 10.1103/physrevd.93.113016. URL: http://dx.doi.org/10.1103/PhysRevD.93.113016.

[95] L. Di Luzio, M. Kirk, and A. Lenz. "Updated B_s-mixing constraints on new physics models for $b \to s\ell^+\ell^-$ anomalies". In: *Physical Review D* 97.9 (May 2018). ISSN: 2470-0029. DOI: 10.1103/physrevd.97.095035. URL: http://dx.doi.org/10.1103/PhysRevD.97.095035.

[96] Daniel King, Alexander Lenz, and Thomas Rauh. "B_s mixing observables and $|V_{td}/V_{ts}|$ from sum rules". In: *Journal of High Energy Physics* 2019.5 (May 2019). ISSN: 1029-8479. DOI: 10.1007/jhep05(2019)034. URL: http://dx.doi.org/10.1007/JHEP05(2019)034.

[97] R. Aaij et al. "Measurement of the $B_s^0 - \bar{B}_s^0$ oscillation frequency Δm_s in $B_s^0 \to D_s^-(3)\pi$ decays". In: *Physics Letters B* 709.3 (2012), pp. 177–184. ISSN: 0370-2693. DOI: https://doi.org/10.1016/j.physletb.2012.02.031. URL: http://www.sciencedirect.com/science/article/pii/S0370269312001621.

[98] *CERN - Accelerating Science*. URL: https://home.cern/ (visited on 03/11/2019).

[99] CMS Collaboration et al. *The CMS experiment at the CERN LHC*. 2008.

[100] G. Aad et al. "The ATLAS experiment at the CERN Large Hadron Collider". In: *Jinst* 3 (2008), S08003.

[101] K. Aamodt et al. "The ALICE experiment at the CERN LHC". In: *Journal of Instrumentation* 3.08 (2008), S08002.

[102] A. Alves Jr et al. "The LHCb detector at the LHC". In: *Journal of instrumentation* 3.08 (2008), S08005.

[103] *The CERN accelerator complex*. URL: https://cds.cern.ch/record/2197559 (visited on 02/10/2019).

[104] M. Aaboud et al. "Luminosity determination in pp collisions at $\sqrt{s} = 8$ TeV using the ATLAS detector at the LHC". In: *The European Physical Journal C* 76.12 (Nov. 2016), p. 653. ISSN: 1434-6052. DOI: 10.1140/epjc/s10052-016-4466-1. URL: https://doi.org/10.1140/epjc/s10052-016-4466-1.

[105] *Luminosity determination in pp collisions at $\sqrt{s} = 13$ TeV using the ATLAS detector at the LHC*. Tech. rep. ATLAS-CONF-2019-021. Geneva: CERN, June 2019. URL: https://cds.cern.ch/record/2677054.

[106] R Alemany-Fernandez, F Follin, and R Jacobsson. "The LHCB Online Luminosity Control and Monitoring". In: CERN-ACC-2013-0028 (May 2013), 3 p. URL: http://cds.cern.ch/record/1567250.

[107] *LHCb - Large Hadron Collider beauty experiment*. URL: http://lhcb-public.web.cern.ch/lhcb-public/ (visited on 10/02/2019).

[108] *Standard set of performance numbers*. URL: http://lhcb.web.cern.ch/lhcb/speakersbureau/html/PerformanceNumbers.html (visited on 10/04/2019).

[109] *LHCb VELO (VErtex LOcator): Technical Design Report*. Tech. rep. CERN-LHCC-2001-011. LHCb-TDR-5. Geneva: CERN, 2001. URL: https://cds.cern.ch/record/504321.

[110] *LHCb magnet: Technical Design Report*. Tech. rep. CERN-LHCC-2000-007. LHCb-TDR-1. Geneva: CERN, 2000. URL: https://cds.cern.ch/record/424338.

[111] *LHCb reoptimized detector design and performance: Technical Design Report*. Tech. rep. CERN-LHCC-2003-030. LHCb-TDR-9. See Chapter 5 for TT specs. Geneva: CERN, 2003. URL: https://cds.cern.ch/record/630827.

[112] *LHCb inner tracker: Technical Design Report*. Tech. rep. CERN-LHCC-2002-029. LHCb-TDR-8. Geneva: CERN, 2002. URL: https://cds.cern.ch/record/582793.

[113] *LHCb outer tracker: Technical Design Report*. Tech. rep. CERN-LHCC-2001-024. LHCb-TDR-6. Geneva: CERN, 2001. URL: https://cds.cern.ch/record/519146.

[114] *LHCb Silicon Tracker - Material for Publications.* URL: https://www.physik.uzh.ch/groups/lhcb/public/material/ (visited on 04/10/2019).

[115] *LHCb RICH: Technical Design Report.* Tech. rep. CERN-LHCC-2000-037. LHCb-TDR-3. Geneva: CERN, 2000. URL: https://cds.cern.ch/record/494263.

[116] *LHCb calorimeters: Technical Design Report.* Tech. rep. CERN-LHCC-2000-036. LHCb-TDR-2. Geneva: CERN, 2000. URL: https://cds.cern.ch/record/494264.

[117] J. R. Harrison. "Radiation damage studies in the LHCb VELO detector and searches for lepton flavour and baryon number violating tau decays". PhD thesis. University of Manchester, 2014.

[118] *LHCb muon system: Technical Design Report.* Tech. rep. CERN-LHCC-2001-010. LHCb-TDR-4. Geneva: CERN, 2001. URL: https://cds.cern.ch/record/504326.

[119] R. Aaij et al. "Design and performance of the LHCb trigger and full real-time reconstruction in Run 2 of the LHC". In: *Journal of Instrumentation* 14.04 (Apr. 2019), P04013–P04013. ISSN: 1748-0221. DOI: 10.1088/1748-0221/14/04/p04013. URL: http://dx.doi.org/10.1088/1748-0221/14/04/P04013.

[120] *Trigger Schemes.* URL: http://lhcb.web.cern.ch/lhcb/speakersbureau/html/TriggerScheme.html.

[121] "Optimization and calibration of the same-side kaon tagging algorithm using hadronic B_s^0 decays in 2011 data". In: LHCb-CONF-2012-033 (Oct. 2012). Linked to LHCb-ANA-2011-103. URL: http://cds.cern.ch/record/1484021.

[122] "Performance of flavour tagging algorithms optimised for the analysis of $B_s^0 \to J/\psi\phi$". In: LHCb-CONF-2012-026 (July 2012). URL: http://cds.cern.ch/record/1458489.

[123] R. Aaij et al. "Opposite-side flavour tagging of B mesons at the LHCb experiment". In: *The European Physical Journal C* 72.6 (June 2012). ISSN: 1434-6052. DOI: 10.1140/epjc/s10052-012-2022-1. URL: http://dx.doi.org/10.1140/epjc/s10052-012-2022-1.

[124] R. Aaij et al. "B flavour tagging using charm decays at the LHCb experiment". In: *Journal of Instrumentation* 10.10 (Oct. 2015), P10005–P10005. ISSN: 1748-0221. DOI: 10.1088/1748-0221/10/10/p10005. URL: http://dx.doi.org/10.1088/1748-0221/10/10/P10005.

[125] L. Breiman et al. *Classification and regression trees.* Taylor & Francis Ltd, 1984.

[126] Y. Freund and R. E. Schapire. "A Decision-Theoretic Generalization of On-Line Learning and an Application to Boosting". In: *Journal of Computer and System Sciences* 55.1 (1997), pp. 119–139. ISSN: 0022-0000. DOI: https://doi.org/10.1006/jcss.1997.1504. URL: http://www.sciencedirect.com/science/article/pii/S002200009791504X.

[127] M. Calvi, O. Leroy, and M. Musy. *Flavour Tagging Algorithms and Performances in LHCb*. Tech. rep. LHCb-2007-058. CERN-LHCb-2007-058. Geneva: CERN, May 2007. URL: http://cds.cern.ch/record/1035129.

[128] M. Gronau, A. Nippe, and Jonathan L. Rosner. "Method for flavor tagging in neutral *B* meson decays". In: *Physical Review D* 47.5 (Mar. 1993), pp. 1988–1993. ISSN: 0556-2821. DOI: 10.1103/physrevd.47.1988. URL: http://dx.doi.org/10.1103/PhysRevD.47.1988.

[129] R. Aaij et al. "New algorithms for identifying the flavour of B^0 mesons using pions and protons". In: *The European Physical Journal C* 77.4 (Apr. 2017). ISSN: 1434-6052. DOI: 10.1140/epjc/s10052-017-4731-y. URL: http://dx.doi.org/10.1140/epjc/s10052-017-4731-y.

[130] R. Aaij et al. "A new algorithm for identifying the flavour of B_s^0 mesons at LHCb". In: *Journal of Instrumentation* 11.05 (May 2016), P05010–P05010. ISSN: 1748-0221. DOI: 10.1088/1748-0221/11/05/p05010. URL: http://dx.doi.org/10.1088/1748-0221/11/05/P05010.

[131] P. Nason et al. *Bottom Production*. 2000. arXiv: hep-ph/0003142 [hep-ph].

[132] T. Sjöstrand, S. Mrenna, and P. Skands. "A brief introduction to PYTHIA 8.1". In: *Computer Physics Communications* 178.11 (June 2008), pp. 852–867. ISSN: 0010-4655. DOI: 10.1016/j.cpc.2008.01.036. URL: http://dx.doi.org/10.1016/j.cpc.2008.01.036.

[133] J. Pumplin et al. "New generation of parton distributions with uncertainties from global QCD analysis". In: *JHEP* 07 (2002), p. 012. DOI: 10.1088/1126-6708/2002/07/012. arXiv: hep-ph/0201195 [hep-ph].

[134] Christian Elsasser. *$\bar{b}b$ production angle plots*. URL: https://lhcb.web.cern.ch/lhcb/speakersbureau/html/bb_ProductionAngles.html.

[135] E. Norrbin and T. Sjöstrand. "Production and hadronization of heavy quarks". In: *The European Physical Journal C* 17.1 (Oct. 2000), pp. 137–161. ISSN: 1434-6052. DOI: 10.1007/s100520000460. URL: http://dx.doi.org/10.1007/s100520000460.

[136] R. Aaij et al. "Measurement of B meson production cross-sections in proton-proton collisions at $\sqrt{s} = 7$ TeV". In: *JHEP* 08 (2013), p. 117. DOI: 10.1007/JHEP08(2013)117. arXiv: 1306.3663 [hep-ex].

[137] M. Cacciari, M. Greco, and P. Nason. "The p_T spectrum in heavy-flavour hadroproduction". In: *Journal of High Energy Physics* 1998.05 (May 1998), pp. 007–007. ISSN: 1029-8479. DOI: 10.1088/1126-6708/1998/05/007. URL: http://dx.doi.org/10.1088/1126-6708/1998/05/007.

[138] M. Cacciari, S. Frixione, and P. Nason. "The p_T spectrum in heavy-flavour photoproduction". In: *Journal of High Energy Physics* 2001.03 (Mar. 2001), pp. 006–006. ISSN: 1029-8479. DOI: 10.1088/1126-6708/2001/03/006. URL: http://dx.doi.org/10.1088/1126-6708/2001/03/006.

[139] M. Cacciari et al. "Theoretical predictions for charm and bottom production at the LHC". In: *Journal of High Energy Physics* 2012.10 (Oct. 2012). ISSN: 1029-8479. DOI: 10.1007/jhep10(2012)137. URL: http://dx.doi.org/10.1007/JHEP10(2012)137.

[140] L. Gladilin. "Fragmentation fractions of $$c$$cand $$b$$bquarks into charmed hadrons at LEP". In: *The European Physical Journal C* 75.1 (Jan. 2015), p. 19. ISSN: 1434-6052. DOI: 10.1140/epjc/s10052-014-3250-3. URL: https://doi.org/10.1140/epjc/s10052-014-3250-3.

[141] R. Aaij et al. "Measurement of the *b*-Quark Production Cross Section in 7 and 13 TeV *pp* Collisions". In: *Physical Review Letters* 118.5 (Feb. 2017). ISSN: 1079-7114. DOI: 10.1103/physrevlett.118.052002. URL: http://dx.doi.org/10.1103/PhysRevLett.118.052002.

[142] R. Aaij et al. "Measurement of *b* hadron fractions in 13 TeV *pp* collisions". In: *Physical Review D* 100.3 (Aug. 2019). ISSN: 2470-0029. DOI: 10.1103/physrevd.100.031102. URL: http://dx.doi.org/10.1103/PhysRevD.100.031102.

[143] J. Butter et al. "Branching fraction measurement of $B^0 \rightarrow D_s^+\pi^-$". In: (May 2019). URL: https://cds.cern.ch/record/2675816.

[144] D. Martínez Santos and F. Dupertuis. "Mass distributions marginalized over per-event errors". In: *Nuclear Instruments and Methods in Physics Research Section A: Accelerators, Spectrometers, Detectors and Associated Equipment* 764 (Nov. 2014), pp. 150–155. ISSN: 0168-9002. DOI: 10.1016/j.nima.2014.06.081. URL: http://dx.doi.org/10.1016/j.nima.2014.06.081.

[145] N. L. Johnson. "Systems of frequency curves generated by methods of translation". In: *Biometrika* 36 (1949), pp. 149–176. DOI: 10.1093/biomet/36.1-2.149.

[146] M. Clemencic et al. "The LHCb Simulation Application, Gauss: Design, Evolution and Experience". In: *Journal of Physics: Conference Series* 331.3 (Dec. 2011), p. 032023. DOI: 10.1088/1742-6596/331/3/032023. URL: https://doi.org/10.1088%2F1742-6596%2F331%2F3%2F032023.

[147] D. J. Lange. "The EvtGen particle decay simulation package". In: *Nuclear Instruments and Methods in Physics Research Section A: Accelerators, Spectrometers, Detectors and Associated Equipment* 462.1 (2001). BEAUTY2000, Proceedings of the 7th Int. Conf. on B-Physics at Hadron Machines, pp. 152–155. ISSN: 0168-9002. DOI: https://doi.org/10.1016/S0168-9002(01)00089-4. URL: http://www.sciencedirect.com/science/article/pii/S0168900201000894.

[148] P. Golonka and Z. Was. "PHOTOS Monte Carlo: a precision tool for QED correctionsin Z and W decays". In: *The European Physical Journal C* 45.1 (Jan. 2006), pp. 97–107. ISSN: 1434-6052. DOI: 10.1140/epjc/s2005-02396-4. URL: http://dx.doi.org/10.1140/epjc/s2005-02396-4.

[149] S. Agostinelli et al. "Geant4 - a simulation toolkit". In: *Nuclear Instruments and Methods in Physics Research Section A: Accelerators, Spectrometers, Detectors and Associated Equipment* 506.3 (2003), pp. 250–303. ISSN: 0168-9002. DOI: https://doi.org/10.1016/S0168-9002(03)01368-8. URL: http://www.sciencedirect.com/science/article/pii/S0168900203013688.

[150] J. Allison et al. "Geant4 Developments and Applications". In: *IEEE Transactions on Nuclear Science* 53 (Feb. 2006), pp. 270–278. DOI: 10.1109/TNS.2006.869826.

[151] K. Cranmer. "Kernel estimation in high-energy physics". In: *Computer Physics Communications* 136.3 (May 2001), pp. 198–207. ISSN: 0010-4655. DOI: 10.1016/s0010-4655(00)00243-5. URL: http://dx.doi.org/10.1016/S0010-4655(00)00243-5.

[152] R. Brun et al. *RooKeysPdf Class Reference.* URL: https://root.cern.ch/doc/master/classRooKeysPdf.html (visited on 11/11/2019).

[153] J. H. Friedman. "Greedy Function Approximation: A Gradient Boosting Machine". In: *The Annals of Statistics* 29.5 (2001), pp. 1189–1232. ISSN: 00905364. URL: http://www.jstor.org/stable/2699986.

[154] M. Pivk and F.R. Le Diberder. "sPlot: A statistical tool to unfold data distributions". In: *Nuclear Instruments and Methods in Physics Research Section A: Accelerators, Spectrometers, Detectors and Associated Equipment* 555.1-2 (Dec. 2005), pp. 356–369. ISSN: 0168-9002. DOI: 10.1016/j.nima.2005.08.106. URL: http://dx.doi.org/10.1016/j.nima.2005.08.106.

[155] J. Borel et al. *The $B_s \to D_s\pi$ and $B_s \to D_s K$ selections.* Tech. rep. LHCb-2007-017. CERN-LHCb-2007-017. LPHE Note 2007-03. Geneva: CERN, Apr. 2007. URL: http://cds.cern.ch/record/1027381.

[156] T. Skwarnicki. "A study of the radiative CASCADE transitions between the Upsilon-Prime and Upsilon resonances". PhD thesis. Cracow, INP, 1986. URL: http://www-library.desy.de/cgi-bin/showprep.pl?DESY-F31-86-02.

[157] T. M. Karbach, G. Raven, and M. Schiller. *Decay time integrals in neutral meson mixing and their efficient evaluation.* 2014. arXiv: 1407.0748 [physics.data-an].

[158] Y. Xie. *sFit: a method for background subtraction in maximum likelihood fit.* 2009. arXiv: 0905.0724 [physics.data-an].

[159] Heavy Flavour Averaging Group. *HFLAV: B Lifetime and Oscillation Parameters.* URL: https://www.slac.stanford.edu/xorg/hflav/osc/index.html (visited on 01/11/2019).